DEVELOPMENT OF ROBOTIC TARGETING SYSTEMS FOR MRI-GUIDED INTERVENTIONS AND RESEARCH

by

ALEXANDER DAVID SQUIRES

(Under the Direction of Zion Tsz Ho Tse)

ABSTRACT

Magnetic Resonance Imaging (MRI) is widely used in medical procedures and supporting research due to its ability to view interior anatomical structures inside living systems, providing high-quality soft tissue imaging while not exposing patients or subjects to ionizing radiation or contrast agents. Advances in MRI technology have led to the development of numerous MR-guided therapies which exploit the excellent soft tissue contrast and high spatial resolution of MRI. This development of hardware and software in the realm of MRI-guided interventions has provided a framework on which the creation of new systems for MRI-guided targeting systems can be built.

Working inside the MR environment imposes several limitations on materials and procedures used. Given the tremendous magnetic field present, safety concerns dictate that only certain materials may be used, restricting choices for structural, actuation, and encoding materials. Beyond safety concerns, other materials and electronic signals become undesirable by causing interference with MR image acquisition. The limited space of the bore limits access to subjects and imposes limitations on the size of systems

designed for intrabore use. Successful mitigation of all these factors is necessary when developing successful designs for MR-guided therapies.

The core of this dissertation is built around three projects: 1) a sample positioning platform for high-field, small-bore MRI; 2) a needle and catheter guidance robot for prostate cancer treatment; and 3) a needle guidance system for stem cell injections into the spines of minipigs. The prostate robot, developed for the NIH Center for Cancer Research, is designed as a guide for needle insertions to a target tumor, after which a laser catheter is inserted to ablate the diseased tissue. The robotic needle guide provides continuous coverage of the prostate and aims to allow surgeons perform MR-guided ablations more quickly. Development of the spinal targeting system for minimally invasive stem cell injection into the spinal cord is part of a larger study to explore ALS therapies, for which a fixed-motor two-axis rotation stage was developed. These projects, while differing in application and final design, are linked through their use of pneumatic motors and overall design criteria.

INDEX WORDS: Surgical Robotics, Magnetic Resonance Imaging, MR

DEVELOPMENT OF ROBOTIC TARGETING SYSTEMS FOR MRI-GUIDED INTERVENTIONS AND RESEARCH

by

ALEXANDER D SQUIRES

BSBE, University of Georgia, 2012

BA, University of Georgia, 2012

A Dissertation Submitted to the Graduate Faculty of The University of Georgia in Partial Fulfillment of the Requirements for the Degree

DOCTOR OF PHILOSOPHY

ATHENS, GEORGIA

2016

DEVELOPMENT OF ROBOTIC TARGETING SYSTEMS FOR MRI-GUIDED INTERVENTIONS AND RESEARCH

by

ALEXANDER DAVID SQUIRES

Major Professor: Zion Tsz Ho Tse
Committee: Mark Haidekker
Charlie Changying Li

Electronic Version Approved:

Suzanne Barbour
Dean of the Graduate School
The University of Georgia
December 2016

ACKNOWLEDGEMENTS

The work presented in this dissertation has been supported by MRI suite time provided by Emory University Hostpital and the National Institutes of Health, without which a discussion of MRI-compatible devices would be quite anemic.

This achievement would not be possible without the support and love of friends and family, to whom I can only begin to express my thanks for keeping me happy and healthy throughout my studies.

To my advisor Dr. Zion Tse, thank you for providing the Medical Robotics Laboratory as a location to grow as a student and a researcher. Under your guidance I have learned much in the development of systems for MR-guided therapies and research. I look forward to carrying those lessons forward and using them to assist in the design of systems for the betterment of humanity.

To my lab-mates past and present: thank you for keeping the lab alive and fun. Research can be a dry occupation, but the lab was always lively with all of you around - even Kevin. A particular thank you is needed for Stan for blazing the path for doctoral candidates in our lab.

To Dicy and Carissa, best friends for over a decade now and for many more decades to come – thank you for always being there. No matter how long goes between us meeting up, we can always jump right back to making fun of each other and supporting each other's aspirations.

To Inaam, my best friend, roommate, and boo, I can't begin to express how much you've helped me out over the years, over academic and personal trials. You've told me to shape up when I needed it and cut loose when I was wound tight. Here's to many more years of good times and snarky messages.

To my family: you have supported my academic aspirations since before I can remember, encouraging me to explore and refine my love of design from paper teepees to tubs of Legos to helping me figure out that it is probably a grounding issue. None of this would be possible without support and encouragement from all of you.

Lastly but furthest from least, I would like to give my utmost love and thanks to my wife Kate for loving and supporting me throughout graduate school. To begin to repay even half of the support you have given me over the past several years, or even just the past few months, is a task I will be trying to accomplish for a long time yet.

TABLE OF CONTENTS

Page

LIST OF TABLES

Page

LIST OF FIGURES

Page

CHAPTER 1

INTRODUCTION

Need for MR-Guided Interventions

There are approximately three main categories of invasiveness of surgical procedures: invasive procedures also known as open surgery, minimally invasive procedures, and noninvasive procedures. Minimally invasive surgery provides great benefits to the patient over conventional open surgery by minimizing the peripheral trauma which is often inevitably linked with performing a medical procedure. Besides enhanced patient outcomes, these differences lead to a shorter recovery time for the patient and reduced risk of complications [1]. However, it is also well documented that minimally invasive surgery brings a number of complications to the operating table. These difficulties are due to the highly limited workspace, specialized tools requiring further staff training and adaption for use, and greatly reduced visual and touch information. Despite the aforementioned drawbacks, minimally invasive surgery has continued to gain popularity and to be widely used [2]. A prime factor in this continued adoption is the corresponding development of medical tools and devices intended for use in minimally invasive surgery.

Medical robotics has been applied in MIS due to favorable traits of robotic systems including high accuracy, repeatability, and the possibility of designing specialized mechanisms that can be applied to specific procedures and organs. Furthermore, medical robots can incorporate sensors to return touch and force

information and can also be combined with medical imaging technology to allow autonomous, semiautonomous, or teleoperated control, which can improve surgical performance and the scope of MIS. In addition, by incorporating emerging imaging techniques and non-invasive modalities, more precise, cost-effective, and portable treatment tools can be made possible. Medical robotics has been in use for approximately thirty years; the first generation of medical robots were used as tool holders and positioners, before the development of active medical robots in the early 1990's [3].

Despite the fact that this technology has been around for three decades, medical robots have not been widely adopted due to limitations of control and the high risk of their applications. The associated regulations and standards, and in particular for active systems, which are intended to be powered during a procedure, are necessarily demanding and as such, the standard development time is very long in this field. There has also been the issue of acceptance from the medical community and surgeons, who still view with distrust any technology that would create a separation of the surgeon from the surgery. A few systems have seen commercial success; these are operated remotely or semiautonomously, where control of the robot remains strictly with the clinician at all times except, in some cases, during a highly restricted function, which can be monitored. A current trend for medical robotics and devices being developed for use with minimally invasive surgery and non-invasive surgery is to further increase the scope of applications with the design of highly function-specific devices that can be combined with medical imaging technology.

Difficulties in Design of MRI-Compatible Devices

MRI possesses several advantages over other noninvasive imaging methods. One of the most apparent ones is the lack of ionizing agents and radiation that is present in MRI. Other systems (Xray, CT, etc) may be direct sources of radiation and/or use ionizing contrast agents to assist in image acquisition. MRI lacks radioactive elements, instead using large magnetic fields and radio frequencies to generate images. This can cause tissue heating in prolonged imaging, but this is easily managed by limiting scanning within a certain time frame, accomplished by most scanners. This lack of radiation is particularly attractive in pediatrics. The resolution of MRI is also highly attractive. Resolution can widely vary depending on scan time, image type, and anatomy location, but in general MRI returns excellent image quality. Ultrasound, as another common nonionizing imaging method, can work faster and has been improving recently with better imaging methods, but still falls short of MR resolution. Additionally, it has difficulty penetrating some tissues which MR does not have an issue with.

Development of MR systems for intrabore use present engineering challenges which require the use of nonstandard actuation and materials to overcome complications when developing peripheral devices for use in MR environments for basic and translational MRI research [4-6]. The primary magnetic field can take hold of ferromagnetic materials, accelerating them rapidly into the bore, which presents a major safety hazard. The RF pulses and magnetic gradients present a pair of problems, one with introduced systems and one with the scanner itself. In an introduced systems, the RF and magnetic gradients can induce electrical currents and noise in metallic components and circuitry, causing heating, false readings, and other undesirable effects. Even disregarding

safety concerns with standard electric motors, the magnetic field present in the MRI would lock them in place, rendering them useless. With regards to the scanner, introduction of foreign materials can cause field inhomogeneities which create image artifacts and decay image quality.

Satisfying safety concerns for devices in the MR environments is relatively simple, requiring a designer to ensure their components are made of MR-safe materials [7]; however, this restrictions cause complications when applied to functional components. Plastic is a preferred material as it is both MR safe and causes no image degrading artifacts. Certain metals such as brass and titanium are safe to use in the MR environment, but should be kept to a minimum as they alter the magnetic field and cause metallic interference artifacts [4, 8, 9]. Development of sources of actuation which are safe to use in the MRI has resulted in methodologies which are expensive to source.

Actuation and encoding causes a significant problem with MR robotics, as standard encoders and actuators are unsafe and/or inoperable in the magnetic field. For this reason, robotic solutions tend to utilize pneumatic or piezoelectric systems for their actuation needs. Piezoelectric motors offer incredible accuracy but require shielding, while pneumatic motors tend to be less precise but can be fabricated totally from plastic, effectively making them invisible to the scanner and able to be operated even while the scanner is in use.

Outline of Dissertation

This dissertation aims to present the design and testing of several systems developed for MR-guided research and therapies. These systems build in complexity throughout the following chapters, beginning with a single degree-of-freedom sample positioning platform and culminating in a 4 degree-of-freedom surgical guide. Common design constraints are explored in each, in addition to unique requirements which drive the development of each system.

References

[1] R. Christopher, S. Nicholas, and D. Robert, "The role of force feedback in surgery: analysis of blunt dissection," in *10th Symposium on Haptic Interface for Virtual Environment and Teleoperator Systems*, 2002, pp. 18-125.

[2] M. J. Mack, "Minimally invasive and robotic surgery," *Jama,* vol. 285, pp. 568-572, 2001.

[3] B. Davies, "A review of robotics in surgery," *Proceedings of the Institution of Mechanical Engineers, Part H: Journal of Engineering in Medicine,* vol. 214, pp. 129-140, 2000.

[4] H. Elhawary, A. Zivanovic, B. Davies, and M. Lamperth, "A review of magnetic resonance imaging compatible manipulators in surgery," *Proceedings of the Institution of Mechanical Engineers Part H-Journal of Engineering in Medicine,* vol. 220, pp. 413-424, Apr 2006.

[5] R. Gassert, A. Yamamoto, D. Chapuis, L. Dovat, H. Bleuler, and E. Burdet, "Actuation methods for applications in MR environments," *Concepts in Magnetic*

Resonance Part B-Magnetic Resonance Engineering, vol. 29B, pp. 191-209, Oct 2006.

[6] N. V. Tsekos, A. Khanicheh, E. Christoforou, and C. Mavroidis, "Magnetic resonance - Compatible robotic and mechatronics systems for image-guided interventions and rehabilitation: A review study," *Annual Review of Biomedical Engineering*, vol. 9, pp. 351-387, 2007.

[7] ASTM, in *"Standard Practice for Marking Medical Devices and Other Items for Safety in the Magnetic Resonance Environment."* vol. F2503, ed.

[8] J. F. Schenck, "The role of magnetic susceptibility in magnetic resonance imaging: MRI magnetic compatibility of the first and second kinds," *Medical Physics*, vol. 23, pp. 815-850, Jun 1996.

[9] F. G. Shellock, "Magnetic resonance safety update 2002: Implants and devices," *Journal of Magnetic Resonance Imaging*, vol. 16, pp. 485-496, Nov 2002.

CHAPTER 2

MAGIC ANGLE POSITIONING SYSTEM

Magic Angle Imaging in High Fields

The signal intensity obtained during MRI scans depends on a combination of natural factors (e.g. T1/T2 times, proton density, field inhomogeneity) and scan parameters (e.g. repetition time/echo time (TR/TE), flip angle) [1]. In highly ordered tissues, water molecules are somewhat restricted in their movement, causing increased spin-spin interactions. These interactions reduce transverse relaxation times (T2), reducing signal intensity at a rate proportional to $3 \cdot \cos^2(\theta)-1$, where θ is the angle between the primary magnetic field (B_o) and the direction in which the spins are coupled [1, 2]. By choosing a signal reduction of 0% (i.e. the maximum signal intensity) the equation returns $\theta=54.74°$, frequently simplified to 55°. This angle is referred to as the "magic angle" and the increase in Signal-to-Noise Ratio (SNR) is known as the magic angle effect [2, 3].

Utilizing this effect, it is possible to obtain high-quality images of fibrous microstructures [3, 4]. With a small-bore scanner, high-resolution images comparable to histology are obtainable without damaging tissue, allowing analysis of living tissues and comparison between in vivo and ex vivo samples [5, 6]. Use of a small-bore, high-field scanner provides an improved signal-to-noise ratio over clinical scanners, delivering a boost in image quality useful when performing functional MRI, microscopic MRI, or other procedures requiring a high resolution in a small field of view [5, 7, 8].

Enhancement of the magic angle effect is possible through the use of ultrashort TE sequences to maximize SNR [9, 10].

Taking advantage of the magic angle effect requires precise positioning and orientation of the sample, as demonstrated in the results; a 5° difference in orientation decreased intensity by almost two-thirds [2-4]. The goal of the presented MAPS is to streamline the iterative process required for imaging fiber tissue structure using the magic angle effect, where precise adjustments are needed repeatedly for magic angle effect to be taken place at different segments of the tissue of the interest. Precise rotation of the sample by a motorized stage could allow the sample to be within the image field of view for comparison without repositioning of the tissue sample and the imaging coil. Thus, a MR-conditional mechatronic system for positioning and orienting samples inside a 9.4T small bore MRI scanner was developed. The presentation of the device in this chapter is meant to highlight the basic design requirements of MR-conditional devices, demonstrate its use, and present data obtained by utilization of the system.

System Design

Any device designed to operate in the MRI environment must be safe in the high-strength magnetic field, which can be accomplished by using non-magnetic materials in the device's design. While non-magnetic metals may be safely used inside the scanner, those materials with high magnetic susceptibility can produce magnetic field inhomogeneity and image artifacts that may negatively affect image quality and provide image voids [11, 12]. To satisfy both safety and image quality considerations, our MRI sample positioning platform was designed and fabricated entirely from acrylonitrile butadiene styrene (ABS, a type of thermoplastic) components. Spatial restrictions were

also important. The positioner would be used in a small-bore horizontal MRI scanner with inserts which limited the effective bore diameter up to 11cm. Tissue samples were placed on a 6cm diameter turntable and contained inside test tubes. To meet the positioning needs of the current projects, the accuracy goal for the device's turntable orientation was positioning error at or below 0.5°.

The specification of positioning resolution was established by consulting the collaborating radiologist and MRI physicist on the project team. The magic angle effect has been adopted clinically to enhance the contrast and SNR of tendinous tissue in MR images [13-15], and from the literature, the clinical protocols for positioning the tissue of interest use a positioning accuracy of 1˚ to 5˚. Therefore, a goal of 0.5˚ positioning resolution is enables the practical use of the device for fast and repeatable positioning in magic angle related studies. Use of a motorized sample positioning platform allows adjustment of sample position to be performed while maintaining the position of the sample stage and MR coils and eliminating the need for repeated movement of the gantry in and out of the bore, streamlining procedures in which multiple adjustments need to be made. Additionally, misalignments when initially loading samples can be compensated for once initial scans have been taken.

The Magic Angle Positioning System (MAPS) is composed of three primary components: the computer interface, the control box, and the sample positioning platform (Figure 2.1). The computer interface provides selection of control modes and angular information. The control box, placed 2 meters from the scanner gantry, houses the valves, fiber optic circuitry, and other electronics necessary to operate the MAPS. The sample positioning platform utilizes pneumatic power to rotate samples inside the bore of the

scanner. Additionally, a connecting cable between the control box and the sample positioning platform was assembled.

(a) MAPS setup schematic in MRI suite

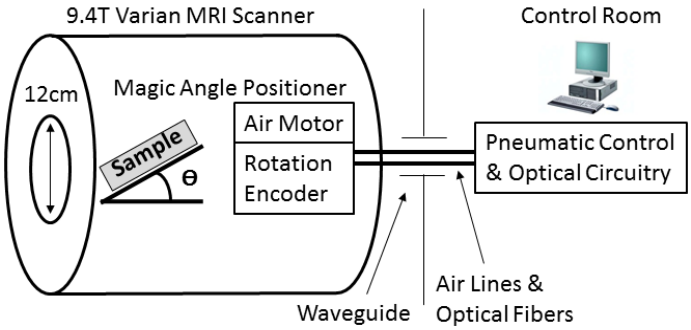

(b) Block diagram of MAPS and control box

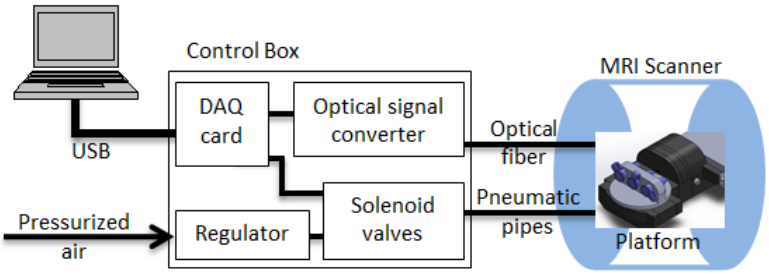

(c) Magic Angle Positioner

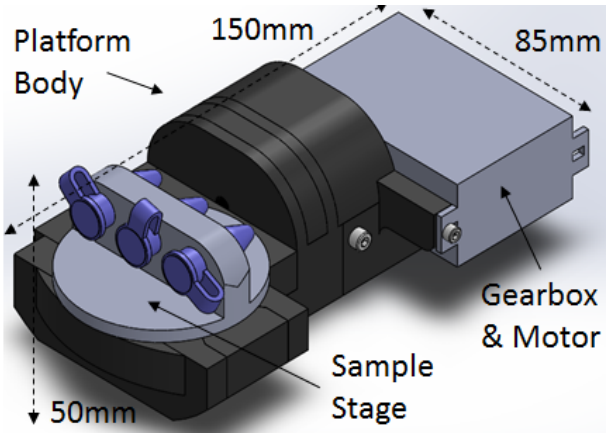

Figure 2.1 – Overview of the Magic Angle Positioning System: (a) Positioner setup in 9.4T small bore, horizontal scanner. (b) Diagram of control circuitry. Similar systems are used in other projects presented in this dissertation. (c) The assembled sample positioning platform.

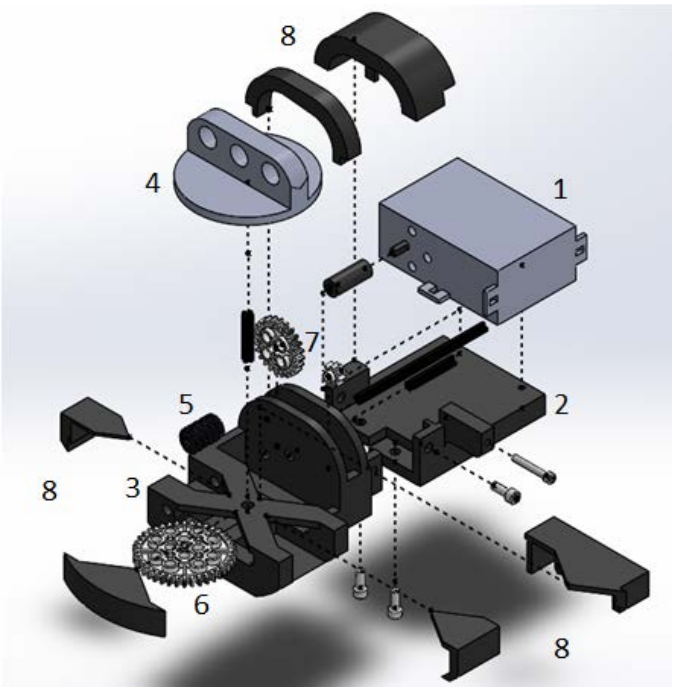

Figure 2.2 –Exploded view of the sample positioning platform. Components are labeled in Table 2.1.

Table 2.1	**Sample Positioning Platform Components**	
Part #	*Component*	*Dimensions, etc.*
1	Motor & Tamiya Gearbox	68x45x27 mm
2	Gearbox Support Body	72x80x30 mm
3	Sample Stage Support Body	85x80x45 mm
4	Sample Stage	Ø55x24 mm
5	Sample Stage Gear	Ø42 mm (40 teeth)
6	Worm Gear	16 mm (3 teeth engaged)
7	Spur Gear Pair	3:1 (24:8 teeth)
8	Assorted Covers	6 different covers

The computer interface, programmed in LabView®, provides a Graphical User Interface (GUI) for operating the MAPS. Operators may choose between either manual or automatic positioning modes, depending on preferences and application. Manual control provides the operator with the choice to rotate the sample platform either clockwise or counter-clockwise. Automatic positioning allows the computer to position the sample platform using a proportional control [16].

The control box is an aluminum enclosure to ensure it is MRI-conditional. The computer interface connects to a National Instruments USB-6009 digital acquisition card, which controls a motor driver and collects signals from a fiber optic kit. The dual H-bridge motor driver (Sparkfun, ROB-09670) provides the power necessary to operate a pair of solenoid valves (ALCON, 01AA031B1-4PCA) which control the airflow that powers the pneumatic motor. The fiber optic kit (Carl's Electronics, CK1500) relayed the rotation of the sample platform. The connection between the control box and the positioning platform consisted of four 1mm fiber optic cables and a pair of 2.8mm ID plastic pneumatic pipes, both of which were outfitted with quick-connect fittings to facilitate ease in transportation and assembly.

The positioning platform (Figure 2.1c) was comprised of 3-Dimensional (3D) printed ABS plastic parts and commercial plastic components, and consisted of two separate sections. The first was a motor housing to hold the pneumatic motor (Figure 2.2), the fiber optic supports, and the initial Tamiya gearbox (TAMIYA Inc., 72005). The second section shifted the axle down and laterally through a 3:1 spur gear combination, then into a 40:1 worm gear. A pair of sample holders was also 3D printed: the first was a flat platform with a ring of holes to act as attachment points for adaptability, while the

second could secure samples contained in micro-centrifuge tubes. Due to being constructed entirely from plastic components, pneumatic actuation, and encoding rotation via optical fibers, a complete lack of electrical components in the platform was achieved, eliminating image fidelity concerns and safety issues due to electrical interference.

The MRI environment imposes huge challenges for electromagnetic (EM) actuators. The static magnetic field, as well as the Radio-Frequency (RF) pulses and switched-magnetic-field gradients applied during imaging, interfere with the normal operation of electronics. Additionally, an EM actuator used in the MRI scanner room can degrade image quality due to EM noise emission [17-19]. For these reasons, a major part of the project was developing the capability to accurately control a nonmetallic pneumatic actuator which can match or approximate the form factor of hobby DC motors used with the commercial gearboxes used. The motor used was derived from a design used in previous work by my advisor [20], with the addition of a reflective optical disc to encode rotation. One channel was used for encoding, with direction derived from the most recent applied direction. Compressed air drove the motor turbine, after which a 60,708:1 gear reduction was accomplished via a 505.9:1 reducing gearbox, a 3:1 spur gear pairing, and a 40:1 worm gear. Plastic ball bearings with polyacetal races, glass balls, and nylon cages were added to the air turbine shaft to reduce friction. Control of the airmotor was accomplished with solenoid air valves, which limited the dynamic response of the control system; this drawback was overcome by controlling the motor with proportionally smaller pulses of air as the motor neared its goal position, timed such that the motor completely stopped before the application of the next pulse. A deadband halted the application of pressure once within an acceptable error range. The development of

this motor is an improvement over previous MR-compatible pneumatic motors, which lacked an integrated quadrature system, instead relying on MR registration or external encoders for position information [15].

The completed system was first tested outside the scanner to ensure accuracy and determine the motor's load capabilities for further testing. Platform accuracy was quantified with a quadrature encoder generating 1024 pulses/revolution, giving a resolution of 0.088° (YUMO Corporation, E6B2-CWZ3E). Unloaded trials at different pressures were used to quantify system accuracy by rotating the output shaft by a specific amount. Loaded trials demonstrated the platform's performance, measured by loading the output shaft of the of the platform in 50g increments from 0g to 500g until the current pressure was incapable of generating the force required to actuate the platform. Trials varied the pressure from 20 to 40 PSI.

Experimental Validation

The MAPS facilitated a series of imaging tests of fibrous tissues using loaded and unloaded ovine Achilles' tendons embedded in agarose gel. System calibration was conducted during the tissue localization scan. Once the initial scan was conducted, the offset angle between B_0 and the principal axis of the tissue sample is used to initialize tissue position and updated when the platform is rotated. Measuring the impact the positioning platform exerted on MR images was performed in a 9.4T Varian/Agilent horizontal MRI scanner, used due to its ability to produce high-resolution images when studying the magic angle effect in a small tissue sample. Two-dimensional high-resolution multi-slice spin echo pulse sequences were used with repetition time = 1000ms, echo time = 13.2ms, and in-plane resolution 60x60 μm^2.

Specifications for defining and measuring artifacts were taken from ASTM standard F2119 [21], based on the parallels between unpowered MR-conditional implants and the unpowered sample platform. Image quality and SNR were evaluated in three conditions: MAPS absent, powered up and down (Fig. 2.4). A cylindrical phosphate buffered saline phantom was imaged with a standard multi-slice spin echo sequence. The SNR of the image with only the phantom was computed using the formula

$$SNR = \mu/\sigma$$

where μ is the mean signal in the 9mm x 9mm region of interest (ROI) in the image center of the phantom (ROI-1) and σ is the standard deviation of the signal in the 9mmX9mm ROI at the right top corner of the image (ROI-2).

Tendons were initially scanned with their primary orientation parallel to the main magnetic field B_o. Defining this as relative 0° to B_0, the samples' rotations were incremented up to the magic angle (~55° relative to B_0), and continued to 90° relative to B_0. Using the standard deviation of surrounding agarose gel as the reference measurement for noise, the signal intensity resulting from the magic angle is measured as the SNR of target structures relative to the surrounding gel.

The magic angle platform was operated in the pressure range of 20 to 40 PSI. Figure 2.3a shows the positioning error in for different target angles and pressure levels. The magic angle platform demonstrated a maximum error of 0.27° as shown in Figure 2.3a, a mean error of 0.020˚, and a standard deviation of 0.073˚ for rotation from all the error measurements (n=180).

Figure 2.3b shows the magic platform under varying load conditions. Load conditions were tested by operating the platform from the initial position of 0˚ (parallel to

the B_0) to the magic angle of 55˚, during which average speed, measured position, and actual position were recorded. While maximum positioning error over all conditions (pressure, target, and load) was 0.27°, all but one condition resulted in error within 0.18˚ of the target. The termination of each pressure condition represented the final load which the system was able to actuate before being unable to generate the requisite torque. Fig. 2.3b demonstrates a linear performance of the motor speed versus the delivery torque under air pressure from 20 PSI to 40PSI, where the motor speed increased with the air pressure level.

(a) MAPS Accuracy in Degrees

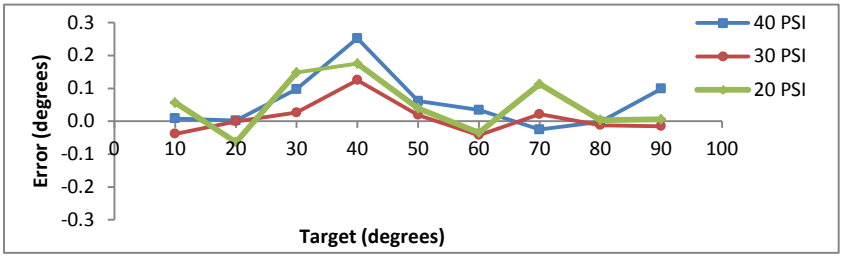

(b) Angular Velocity under different load conditions

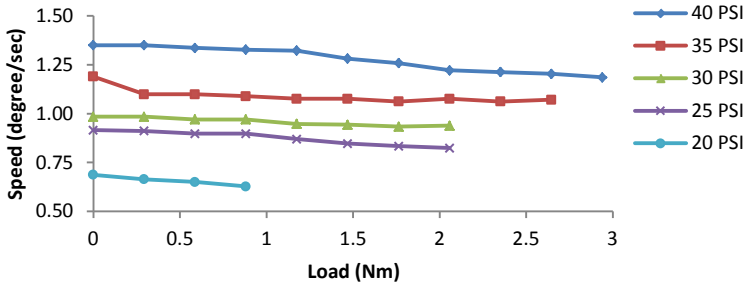

Figure 2.3 – (a) MAPS positioning error. (b) Stage velocity under varying loads.

MRI Compatibility

The images used for MRI compatability calculation are displayed in Fig. 2.4; there was less than 0.5% SNR difference between the conditions, demonstrating minimal

effect from the system to the MRI images [22, 23]; no observable image artifacts existed when MAPS was present. SNR was calculated according to:

$$SNR = \mu_1/\sigma_2$$

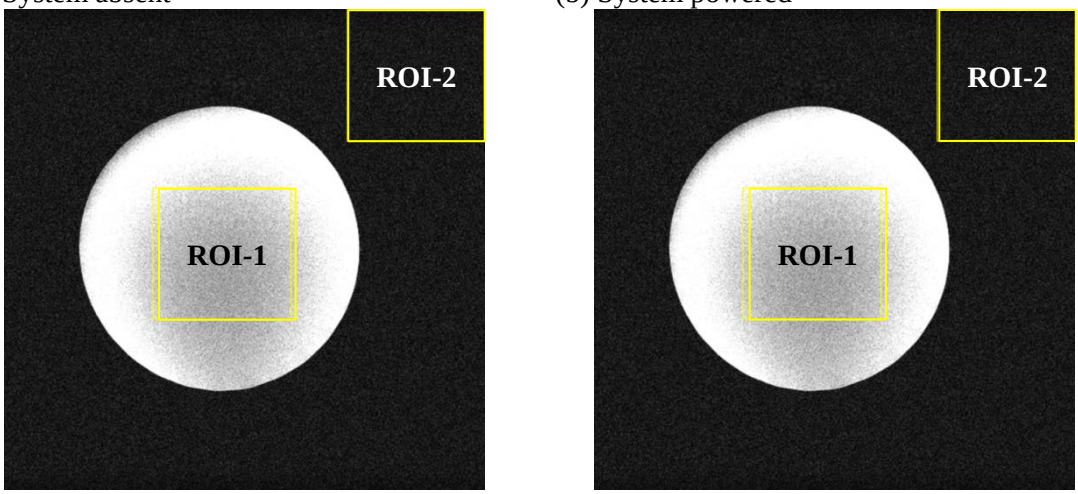

Figure 2.4 Saline phantom when the sample platform is unpowered (a) and powered up (b). The yellow square indicates the 9mmX9mm regions of interest (ROI) for SNR measurement.

Imaging Collagen Fibers in Tendons

Use of MAPS was employed by testing at the University of Pittsburgh in analysis of collagen fibers in tendons. The results in Fig. 2.5 show an increase in relative signal intensity as both loaded and unloaded tendons draw near to the magic angle. An unloaded tendon had an increase in signal intensity at the magic angle of about 200% relative to that at 0° to B_0, whereas a loaded tendon had a greater signal intensity increase, up to approximately 600% relative to that at 0° to B_0. Normalized data is shown quantitatively in Fig. 2.5b. SNR for signal intensity measurements was calculated with the same method as the MRI compatibility tests.

The undulating pattern of the collagen fibers in the unloaded tendon samples, known as “crimping” [24, 25], shows up strongly near the magic angle as light and dark

bands perpendicular to the main orientation of the tendon. Similarly, the striated patterns of the loaded tendon were most pronounced near the magic angle (Figure 2.5a, 55˚), consistent with the stretch of the collagen fibers and disappearance of the crimp observed in MR images and in histology (Figure 2.5a, 2.6a) [6].

The MR signals were higher in loaded than unloaded tendons near the magic angle by a factor of 2 to 3. This is, in part, because in loaded tendons, the collagen fibers are more aligned with one another, longitudinally to the tendon [26]. This explains the increased signal at the magic angle, but not the slight increase in signal in loaded tendons at other angles. This could be because in highly ordered, collagen rich fibrous tissues, bound protons are subject to spin-spin interactions within a static magnetic field. An

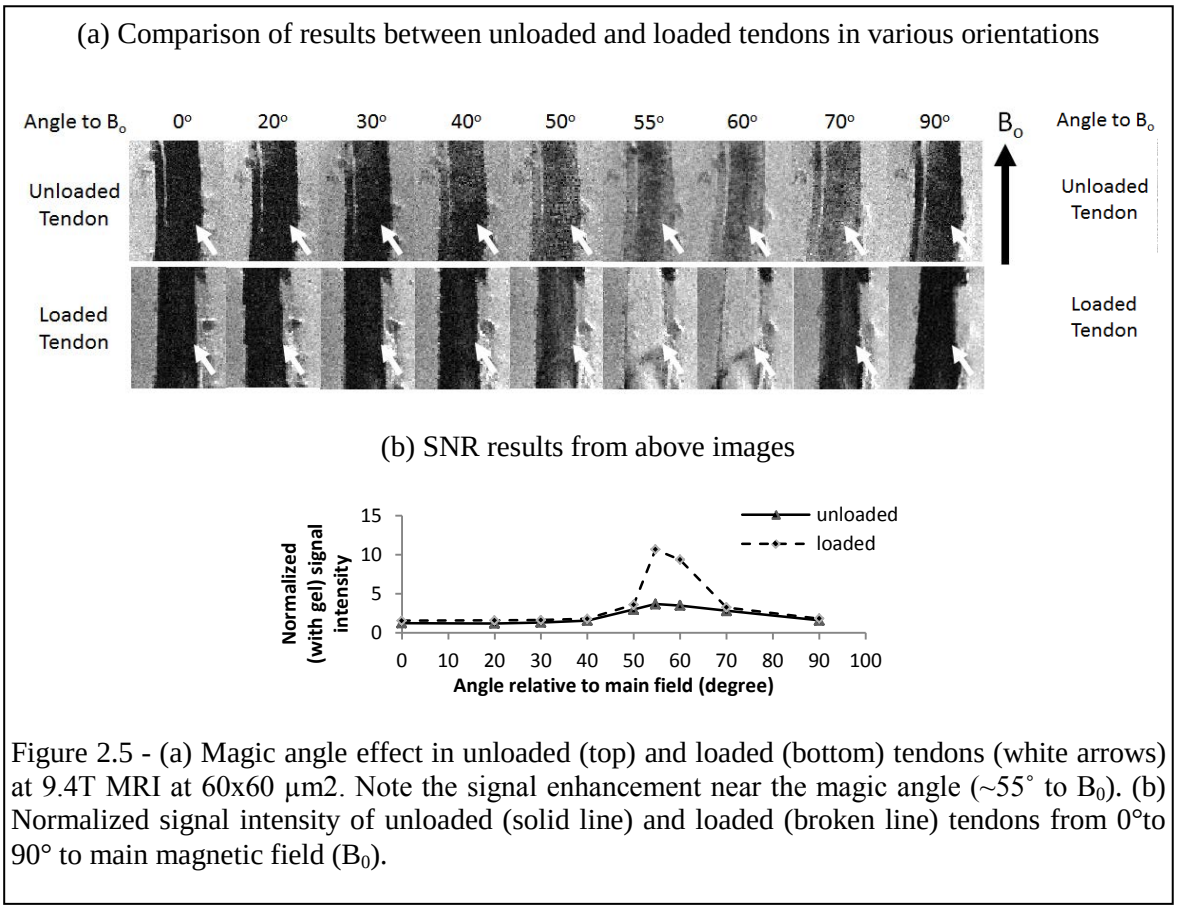

Figure 2.5 - (a) Magic angle effect in unloaded (top) and loaded (bottom) tendons (white arrows) at 9.4T MRI at 60x60 μm2. Note the signal enhancement near the magic angle (~55˚ to B_0). (b) Normalized signal intensity of unloaded (solid line) and loaded (broken line) tendons from 0°to 90° to main magnetic field (B_0).

increase in the distance between protons in tendons, caused by stretching during loading, may reduce the spin-spin interactions and increase signal strength [6]. Another possible explanation lies in the release of water, which was bound within the tendon prior to loading, altering the T2 relaxation time constant [27].

(a) Histology, unloaded tendon (b) Histology, loaded tendon

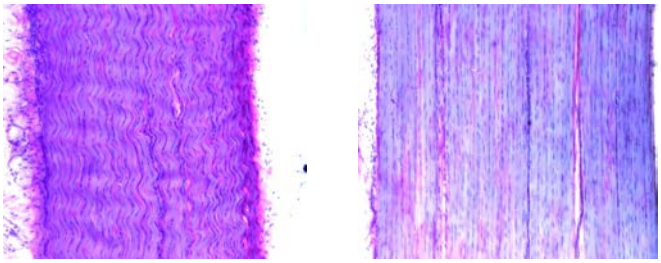

Crimping Striation

Figure 2.6 - Histological images of the tendons illustrating the orientation of the collagen fibers in unloaded (a) and loaded (b). The magic angle effect is more significant in the loaded tendon due to a high degree of alignment, whereas in the unloaded tissue the signal is partially canceled out due to the unaligned nature of crimped fibers. (a) corresponds with the Unloaded Tendon rows in Fig. 2.5a, while (b) is a tendon under load, as the bottom row in Fig. 2.5a.

Discussion

A high-field, small-bore MRI-conditional positioning system was developed using a miniature pneumatic motor, intended to facilitate Magic Angle-related experiments evaluating microstructures in fibrous tissues for basic and translational MRI research. The hardware and software were designed to provide a simple and accurate solution (max error <0.5˚) for studying magic angle effect in fibrous tissues within a high-field and small bore MRI scanner. The hardware for the intra-scanner component contained a unique motion-encoder unit in conjunction with a reduction gearbox to accomplish highly accurate positioning of a sample platform for studies. The positioning platform demonstrated high levels of accuracy, positioning diminutive fibrous tissue

samples in a small-bore scanner without the need for manual adjustment. Furthermore, the total lack of metallic components or electrical signals permitted high-resolution imaging free of image artifacts and radiofrequency electromagnetic interference. The use of custom 3D printed pneumatic actuators and encoder components drove the cost of the system down.

Validation of the system as a research tool was performed in unloaded and loaded tendon samples in which images demonstrated 200%-600% increase in SNR using the system. With the positive results generated, this system has demonstrated its practical usability in magic angle studies and other experiments that requires precise positioning within high-field small bore MRI scanners.

References

[1] S. J. Erickson, R. W. Prost, and M. E. Timins, "The Magic-Angle Effect - Background Physics and Clinical Relevance," *Radiology,* vol. 188, pp. 23-25, Jul 1993.

[2] Y. Xia, "Magic-angle effect in magnetic resonance imaging of articular cartilage - A review," *Investigative Radiology,* vol. 35, pp. 602-621, Oct 2000.

[3] G. D. Fullerton, I. L. Cameron, and V. A. Ord, "Orientation of Tendons in the Magnetic-Field and Its Effect on T2 Relaxation-Times," *Radiology,* vol. 155, pp. 433-435, 1985.

[4] L. C. Ho, I. A. Sigal, N.-J. Jan, A. Squires, Z. Tse, E. X. Wu, *et al.*, "Magic angle-enhanced MRI of fibrous microstructures in sclera and cornea with and without intraocular pressure loading," *Investigative ophthalmology & visual science,* vol. 55, pp. 5662-5672, 2014.

[5] E. Y. Chang, J. Du, W. C. Bae, S. Statum, and C. B. Chung, "Effects of achilles tendon immersion in saline and perfluorochemicals on T2 and T2*," *Journal Of Magnetic Resonance Imaging: JMRI*, vol. 40, pp. 496-500, 2014.

[6] K. M. Mountain, T. A. Bjarnason, J. F. Dunn, and J. R. Matyas, "The functional microstructure of tendon collagen revealed by high-field MRI," *Magnetic Resonance In Medicine: Official Journal Of The Society Of Magnetic Resonance In Medicine / Society Of Magnetic Resonance In Medicine*, vol. 66, pp. 520-527, 2011.

[7] N. Wang, D. Kahn, F. Badar, and Y. Xia, "Molecular origin of a loading-induced black layer in the deep region of articular cartilage at the magic angle," *Journal Of Magnetic Resonance Imaging: JMRI*, 2014.

[8] F. Schick, "Whole-body MRI at high field: technical limits and clinical potential," *European Radiology*, vol. 15, pp. 946-959, 2005.

[9] J. Du, S. Statum, R. Znamirowski, G. M. Bydder, and C. B. Chung, "Ultrashort TE T1ρ magic angle imaging," *Magnetic resonance in medicine*, vol. 69, pp. 682-687, 2013.

[10] M. Bydder, J. H. Brittain, A. Shimakawa, A. Takahashi, J. W. Johnson, M. D. Robson, *et al.*, "MAGIC ANGLE EFFECTS AND ULTRASHORT TE (UTE) IMAGING," presented at the International Society for Magnetic Resonance in Medicine, Miami, 2005.

[11] A. Rudisch, C. Kremser, S. Peer, A. Kathrein, W. Judmaier, and H. Daniaux, "Metallic artifacts in magnetic resonance imaging of patients with spinal fusion.

A comparison of implant materials and imaging sequences," *Spine,* vol. 23, pp. 692-699, 1998.

[12] J. F. Schenck, "The role of magnetic susceptibility in magnetic resonance imaging: MRI magnetic compatibility of the first and second kinds," *Medical Physics,* vol. 23, pp. 815-850, Jun 1996.

[13] H. Elhawary, A. Zivanovic, M. Rea, Z. Tse, D. McRobbie, I. Young, *et al.*, "A MR Compatible Mechatronic System to Facilitate Magic Angle Experiments in Vivo," in *Medical Image Computing and Computer-Assisted Intervention – MICCAI 2007*. vol. 4792, N. Ayache, S. Ourselin, and A. Maeder, Eds., ed: Springer Berlin Heidelberg, 2007, pp. 604-611.

[14] H. Elhawary, A. Zivanovic, Z. T. H. Tse, M. Rea, B. L. Davies, I. Young, *et al.*, "A magnetic-resonance-compatible limb-positioning device to facilitate magic angle experiments in vivo," *Proceedings of the Institution of Mechanical Engineers, Part H: Journal of Engineering in Medicine,* vol. 222, pp. 751-760, May 1, 2008 2008.

[15] T. Zion Tsz Ho, H. Elhawary, A. Zivanovic, M. Rea, M. Paley, G. Bydder, *et al.*, "A 3-DOF MR-Compatible Device for Magic Angle Related <emphasis emphasistype="italic">In Vivo</emphasis> Experiments," *Mechatronics, IEEE/ASME Transactions on,* vol. 13, pp. 316-324, 2008.

[16] K. J. Åström and T. Hägglund, "PID controllers: theory, design, and tuning," *Instrument Society of America, Research Triangle Park, NC,* 1995.

[17] ASTM-F2182, "Standard Test Method for Measurement of Radio Frequency Induced Heating On or Near Passive Implants During Magnetic Resonance Imaging," 2011.

[18] F. G. Shellock, "Metallic surgical instruments for interventional MRI procedures: evaluation of MR safety," *Journal of Magnetic Resonance Imaging*, vol. 13, pp. 152-7, 2001.

[19] H. Elhawary, Z. T. H. Tse, A. Hamed, M. Rea, B. L. Davies, and M. U. Lamperth, "The case for MR-compatible robotics: a review of the state of the art," *The International Journal of Medical Robotics and Computer Assisted Surgery*, vol. 4, pp. 105-113, 2008.

[20] Z. Tse, H. Elhawary, A. Zivanovic, and M. Lamperth, "A one degree of freedom MR compatible haptic system for tissue palpation," in *Proceedings of the 13th Annual Meeting of the British Chapter of the International Society for Magnetic Resonance in Medicine*, 2007.

[21] ASTM, "Standard Test Method for Evaluation of MR Image Artifacts from Passive Implants," vol. F2119, ed. West Conshohocken, PA: ASTM International, September 2007.

[22] K. Chinzei, R. Kikinis, and F. Jolesz, "MR Compatibility of Mechatronic Devices: Design Criteria," in *Medical Image Computing and Computer-Assisted Intervention – MICCAI'99*. vol. 1679, C. Taylor and A. Colchester, Eds., ed: Springer Berlin Heidelberg, 1999, pp. 1020-1030.

[23] K. Chinzei, N. Hata, F. Jolesz, and R. Kikinis, "MR Compatible Surgical Assist Robot: System Integration and Preliminary Feasibility Study," in *Medical Image*

Computing and Computer-Assisted Intervention – MICCAI 2000. vol. 1935, S. Delp, A. DiGoia, and B. Jaramaz, Eds., ed: Springer Berlin Heidelberg, 2000, pp. 921-930.

[24] B. J. Rigby, N. Hirai, J. D. Spikes, and H. Eyring, "The Mechanical Properties of Rat Tail Tendon," *The Journal of General Physiology*, vol. 43, p. 265, 11/01/Number 2/November 1959 1959.

[25] A. Viidik and R. Ekholm, "Light and electron microscopic studies of collagen fibers under strain," *Zeitschrift für Anatomie und Entwicklungsgeschichte,* vol. 127, p. 154, 12/03/ 1968.

[26] S. P. Lake, K. S. Miller, D. M. Elliott, and L. J. Soslowsky, "Effect of fiber distribution and realignment on the nonlinear and inhomogeneous mechanical properties of human supraspinatus tendon under longitudinal tensile loading," *Journal of Orthopaedic Research,* vol. 27, pp. 1596-1602, 2009.

[27] J. A. Hannafin and S. P. Arnoczky, "Effect of cyclic and static tensile loading on water content and solute diffusion in canine flexor tendons: an in vitro study," *Journal Of Orthopaedic Research: Official Publication Of The Orthopaedic Research Society,* vol. 12, pp. 350-356, 1994.

CHAPTER 3

PLANAR GUIDE FOR PROSTATE INTERVENTIONS

Advantages of MR-Guided Prostate Interventions

Prostate cancer is the most common male cancer in the United States with an estimated 220,000 new cases and 28,000 deaths in 2015 [1]. Most cases of the disease are low-risk, non-metastasizing disease for which targeted, focal therapy has emerged as a treatment alternative that spares patients from undesired side effects such as impotence and incontinence [2]. Currently, the most frequently utilized treatment for localized prostate cancer is radical prostatectomy which entails partial or total removal of the prostate. Following the prostatectomy, morbidities may develop, including incontinence and sexual dysfunction [3]. Given the drastic nature of this treatment, alternative solutions to radical prostatectomy are desirable. Patients can pursue active surveillance or localized treatment, but usually prefer the latter to avoid the anxiety associated to leaving the disease untreated [4]. Localized treatments for prostate cancer include cryoablation, high-intensity focused ultrasound (HIFU), and Focal Laser Ablation (FLA). FLA has the advantage of effectively treating the tumor volume while minimizing over-treatment in the surrounding tissues [5].

Utilizing high-energy laser technology, FLA induces cell death through rapid, targeted heating of tissue. FLA generates a well-controlled ablation zone to target a prostate tumor, leaving the majority of the gland intact including the delicate neurovascular bundles and the urethral sphincters [6]. While FLA for localized prostate

cancer is receiving increased attention due to its potential for providing an optimal level of cancer control in select patients with a minimal amount of treatment-related side effects, the procedure has several technical limitations. These limitations are mostly related to the difficulty of effectively localizing the prostate tumor for treatment planning, safely placing the laser catheter to ablate the entire tumor and achieve adequate margins, and accurately monitoring the ablated area. Further complicating these difficulties, larger tumors require multiple overlapping catheter placements, which can be difficult to achieve in an accurate and repeatable manner using current free-hand/template-based techniques. Thermal ablation is effective for treating small tumors; however, the success rate for eliminating large tumors is low in part because physicians have difficulty discerning if ablations have fully covered the tumor. Although treatment planning which utilizes pre-procedural images to plan multiple ablations is an option, it is highly probable that the tumor moves during the ablation procedure [7, 8]. Even if a perfect surgical plan could be calculated, a physician will likely have difficulty delivering the ablation device at the exact locations of the plan, resulting in under-treatment of the tumor or potential damage to adjacent normal tissue, if not both. In response to these problems, iterative laser treatment planning is desired as an enhanced therapy, using preoperative parametric MRI (structural and pathological) information together with intraoperative MR thermometry imaging to update the plan iteratively after each ablation [9].

Performed under multi-parametric MRI guidance, FLA benefits from pre-operative planning and tumor identification, as well as intra-operative guidance and ablation monitoring. MRI offers a superior imaging modality for prostate FLA, providing excellent image contrast between the cancerous and healthy surrounding tissues. MRI

thermometry offers real-time monitoring of the ablated zone. Additionally, MRI-guidance allows real-time visualization of both the therapeutic device and the tumor in the same image [10-17]. Widespread adoption of MRI-guided therapy has been hindered by the scarcity and cost of MRI facilities, as well as limited physician access to patients positioned within the MRI bore. The constraints of working within the bore of an MRI scanner have led to the development of strategies to perform procedures outside of the scanner using MRI data, utilizing techniques such as frameless stereotaxy [13, 18]. These techniques are susceptible to misregistration caused by motion and shifting of position as patients are removed from and replaced in the MRI bore. The efficiency of the procedure is compromised because the procedure requires moving the patient in and out of the bore multiple times and frequent hardware readjustment, with resulting procedure times averaging 4-6 hours per patient. To reduce procedure time so MRI-guided prostate therapy can be applied in routine clinical practice, a procedure performed entirely inside the magnetic bore without multiple starts and stops for human operator manipulations is desirable. A carefully designed robotic system can simplify MRI-guided prostate therapy by optimizing the workspace and access to the tissue of interest, improving the positioning accuracy and repeatability of interventional tools, and reducing patient setup time.

FLA could be performed using a grid template (similar to those used in brachytherapy) to guide the laser ablation catheter into the targeted location under MRI-guidance [19]. The template design provided by Visualase Inc. for FLA could be considered suboptimal for the following reasons: 1) the distance among the holes is 5 mm, limiting the potential accuracy. 2) FLA does not provide needle angulation, which is

sometimes required to avoid pubic arch interference or nerve bundles. 3) The user interface included with the commercial product does not provide the capability and workflow required for effective treatment planning and subsequent procedures in FLA.

Numerous MRI-conditional robotic systems for prostate procedures have been reported in literature, but they are primarily for biopsy. Seifabadi in [20] reviews those robotic systems and categorized them into three groups based on the method of needle placement: transrectal, transperineal, and transglutteal. While those systems have shown potential, they suffer from negatively influencing MR image signal to noise ratio (SNR), procedure workflow, bulkiness, and patient safety by making the needle placement fully automatic [21]. Cepek et.al reported a positioning system for MRI-guided FLA of prostate with patient trials [22]. However, the device was manually operated, making the presented hardware and software the first robotic system reported for MRI-guided focal laser ablation of prostate to the best of the authors' knowledge. An MRI-guided ablation robotic system has been reported, although it was intended for liver laser ablation [23]. The presented robotic system removes the burden of needle guidance from the physician, thus making the procedure more efficient and straightforward, only requiring a physician to insert the needle to the prescribed depth.

Developing Multiple Degrees of Freedom

Hardware Design

The robotic assistance system consisted of three major components: the robotic needle positioner, a control box, and the host PC. The MRI-conditional robot was positioned near the patient's perineum while they are in a supine position in the MRI bore (Fig. 3.1, 3.2). Connected to the robot via pneumatic and optical lines through the

waveguide, the control box contained the hardware necessary for manipulating the robot. The host PC ran control software for the robot in addition to custom FLA surgical planning software. The robotic positioning system was developed with the goal of performing transperineal prostate ablations with accuracy beyond that of freehand or template approaches by keeping targeting errors under 2mm while simultaneously lessening procedure times and avoiding damage to nearby anatomy. Further design specifications included:

- An MR-conditional robot capable of operating with little or no artifact generation
- A workspace that spanned the entirety of the prostate in most patients
- A motorized needle guidance channel
- The ability to angle the robot, intended to bypass critical anatomical structures was desired.
- Needle insertions being performed by surgeons, who wanted tactile feedback and human supervision during the procedure. Furthermore, human insertion would simplify regulatory concerns should the design be commercialized.

A slim robot design built around a Core-XY belt system was chosen as a solution to the design requirements [1]. The Core-XY belt system is a modification of a standard 2-axis positioning frame frequently found in CNC-controlled machinery, such as mills and 3D printers, with independent control of each axis by its own motor. However, the secondary axis (e.g. the horizontal axis in Fig. 3.1a) has the motor mounted on the moving arm, adding to the size and inertia of the end effector. In our robot, the Core-XY system allows both motors to be mounted on the robots frame, reducing the number of moving parts and allowing a more slender robot while maintaining the same workspace.

(a) Robot Setup in MR

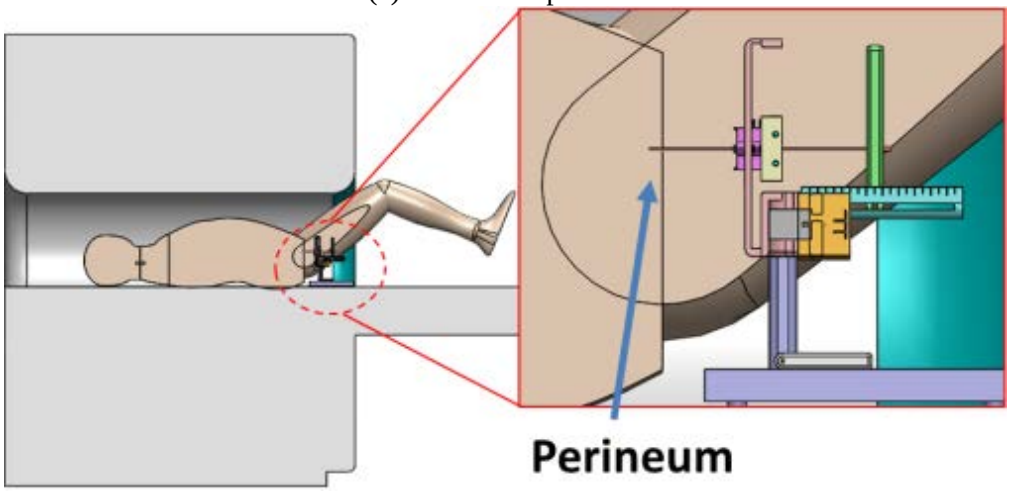

(b) Robot Front & Side Views

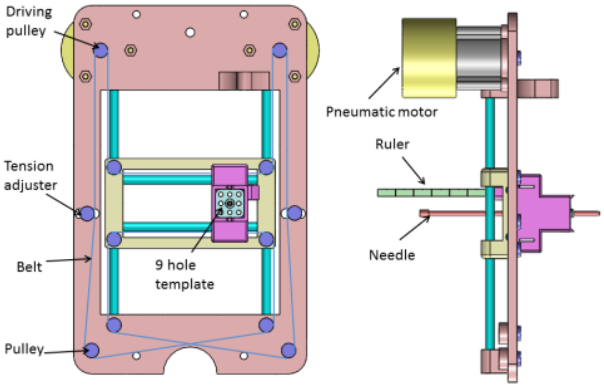

(c) Robot base and angulation platform

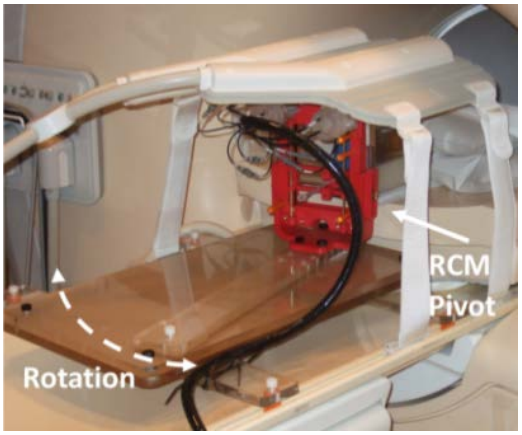

(d) Bottom view of robot base and angulation platform - RCM

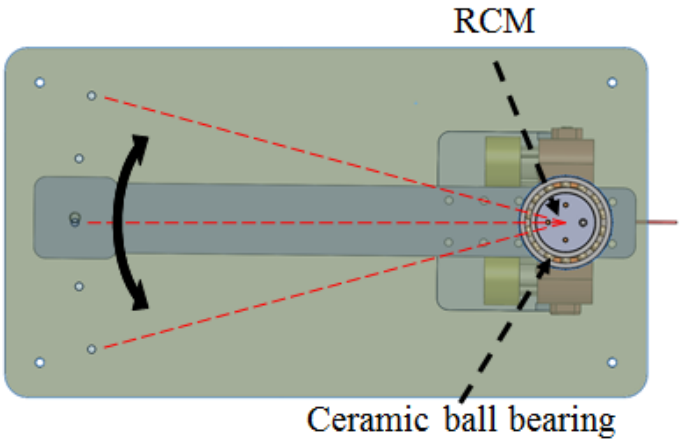

Figure 3.1 - Design of an MRI-guided transperineal robotic positioner. (a) Overview of the full robotic system (b) Front and side view showing the robot design. (c) Positioner setup inside the scanner. (d) Bottom view of the robot board.

(a) Robotic Needle Guide

(b) Robotic Needle Guide

(c) Robotic Needle Guide

(d) Robot Setup in MRI

(e) Robot Setup out of MRI bore

(f) Robot setup in MRI bore

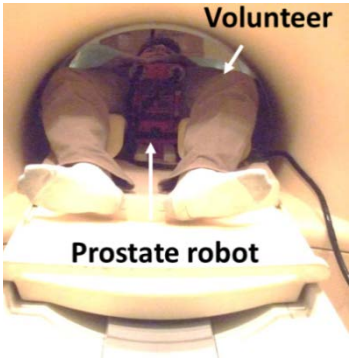

Figure 3.2 - Robot and human setup in the MRI scanner. (a) and (c) show surgeon and patient views of the robot, with (b) showing a side view. (d) Robot setup and laser fiber/cooling catheter. A surface coil is placed on top of the robot. (e) and (f) show the robot and patient setups.

The Core-XY system utilizes a single belt, requiring the motors to work in sync to position the end effector of the robot. The two motors A and B can independently be turned CW or CCW, resulting in 4 possible combinations of motor rotation, which corresponds to the end effector moving up, down, left, or right. This relation is mathematically defined as:

$$\Delta X = \frac{1}{2}(\Delta A + \Delta B)$$

$$\Delta Y = \frac{1}{2}(\Delta A - \Delta B)$$

The robot's base plate (Fig. 3.1d) was designed to slide underneath the patient until the pivot point of the targeting assembly was located under the patient's prostate, defining the prostate as the remote center of motion (RCM) as shown in Fig. 3.1d. The RCM allowed the robot and needle guide to be located at a different location from the pivot point while still rotating about the prostate, providing optimal coverage of the desired volume, i.e. the prostate. The width of the robot permitted the robot to face against the patient's perineum while the end effector is less than 25mm away from the perineum. The robot is designed to provide coverage of the prostate comparable or exceeding that of existing systems, with continuous coverage in the transverse plane and along the scanner axis via adjustable insertion depth. The robot contains two motorized, continuous degrees of freedom (DOF) for horizontal and vertical motion and one manual, discrete degree of freedom for rotation. In the transverse plane, the robot offers 51mm of horizontal (left-right) movement and 83mm of vertical (ventral-dorsal) movement. The discrete DOF pivots the robot about the RCM, providing 0˚, ±7.5˚ and ±15˚ relative to 0˚ parallel to the axis of the bore, permitting targeting of tumors located laterally to the urethra and neurovascular bundles without damaging these critical structures. The

guidance channel can be removed from the robot for sterilization as well as use of alternate sized channels for differing needle gauges.

Actuation of the horizontal and vertical DOFs (Fig. 2a-b) utilizes a pair of motors to adjust the position of the needle guide. The motors were both mounted on the robot frame, simplifying the design of the moving parts in the robot and avoiding obstructing the workspace. The motors are an enhanced version of motors previously used by the researchers with optical quadrature encoding embedded within the motor unit for precise positioning [24].

The robot was controlled through a graphical user interface designed in LabVIEW 2014 (National Instruments, Austin, TX). A graphical display demonstrated the workspace, end effector position, and target position. Operators could choose to drive the end effector to the target position either manually or automatically. The control scheme was derived from proportional control with a deadband accuracy of 0.3mm. The solenoid valves were opened based on a PWM signal with a low time sufficient to allow the motor to come to a complete stop at the maximum operating pressure. The high time of the signal was calculated based on the distance to the target position, with a sufficiently large value overwriting the PWM signal with a continuously high signal. Based on the target point, the program gave a tool length to which the needle, catheter, or other tools should be inserted.

The commercially available Visualase Laser Ablation System (Medtronics, Minneapolis, MN) was used in this study. The ablation system consisted of a laser generator, an optical fiber that delivers laser from control room into scanner room, a water cooling system, a cooling catheter that the laser fiber passes through, a computer

workstation, and a mechanical grid template (65 mm × 65 mm – holes are 5 mm apart) with embedded fiducials for registration. In this study, only the laser generator, optical fiber, and cooling catheter were used, and the presented robotic positioning hardware and OncoNav software were adopted for surgical planning, catheter positioning and navigation, as well as thermometry monitoring. OncoNav was developed by the NIH Clinical Center over the past five years and provides the ability to segment images and do treatment planning [25].

The design of the pneumatic motors used for actuation was an expansion on the design utilized in previous studies. Prior motor designs used a single reflection-based fiber optic line to provide encoding, and the motor housing was held together by the same threaded rod used to attach the motor to the planetary gearbox as well as the robot.

On the exterior of the new design of the motor housing (cap and body), extensions were added to allow the motor housing to be assembled independently of affixation to the gearbox and robot, assuring the robustness of the motor as an independent unit. The encoding ability of the motor was improved by instead integrating a pair of interruption-based fiber optic lines, which permitted quadrature encoding and a higher degree of reliability for the encoding. The cap was extended to allow a pair of stacked fiber optic cables to be inserted, while an extension on the rotor supported the asymmetric interrupters which blocked transmission of the optical signal.

The robot was registered to the MR coordinate system using a series of 5 PinPoint fiducials (Beekley, USA) mounted in wells in the frame of the robot. These fiducial markers were originally located near the same plane as the 4mm brass rods used as rails for the moving components, which caused a large enough artifact in their vicinity to hide

the fiducial markers. A 50mm standoff was designed to fit into the original fiducial wells and increase the fiducials distance from the brass rods, allowing them to be seen for registration. The robot's coronal midline was selected as the zero point for the robot's insertion axis.

(a) Motor Assembly

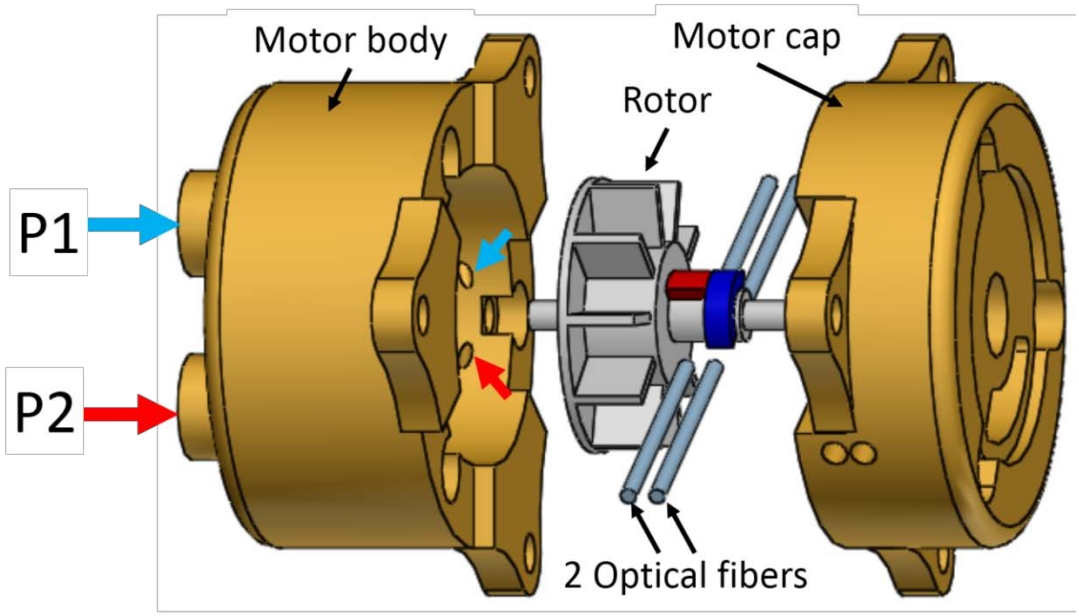

(b) Quadrature signal

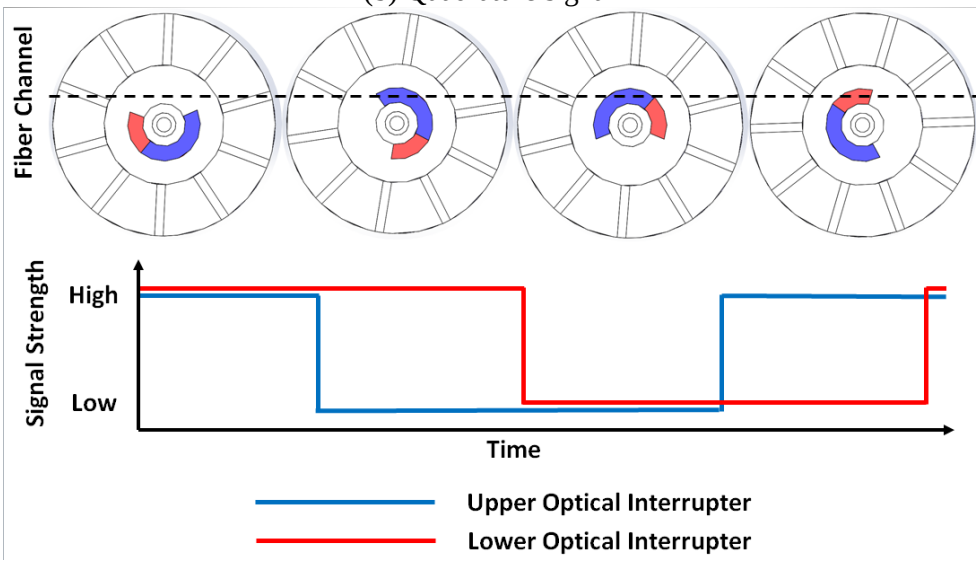

Figure 3.3 – Updated design of the airmotor for the prostate robot. (a) Motor components. The cap is extended and holds the fiber optic lines. (b) Rotation of turbine causes the creation of a quadrature signal once per revolution.

The control box for the robot was built around a National Instruments USB-6001 DAQ card. Four pairs of fiber optic transmitters and receivers, two pairs per motor, provided the capability of encoding motor rotation. The default output for the optical receivers was a digital TTL signal, which proved somewhat unreliable for transmission through multiple fiber junctions and a 10mm air gap, necessitating readings to be taken directly from the phototransistor which provided a clear signal despite being shy of activating the Shmidt trigger in the digital output circuit. Four solenoid valves, two per motor, controlled air flow to the motors.

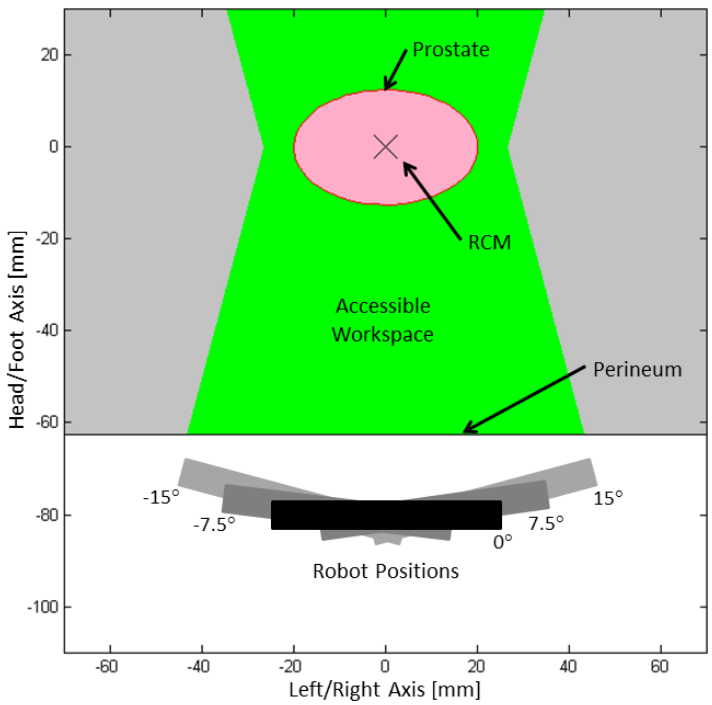

Figure 3.4 - Coronal view of the robot workspace: prostate (red oval), RCM (black x), the level of the perineum (black line), and the width of robot workspaces in each position (parallel blue lines). Distance from the inferior edge of the prostate to the perineum is 50mm, on the high side of the typical adult male range of 30-50mm.

System Validation

MRI Compatibility

Validation of the robot as a low-interference device for MR images was accomplished by calculating signal-to-noise ratios (SNR) of a homogenous phantom under four conditions (Table 1). The SNR variation was <7.5% in all cases, thus falling within an acceptable range for devices used inside MRI [26]. The SNR was calculated using the standard formula

$$SNR = \mu_1/\sigma_2$$

where $\mu_1$is the mean value of the target region and σ_2 is the standard deviation of the region in empty space (Figure 3.5a).

Table 3.1	**MR Compatibility test condition**
Evaluation steps	*Description*
Control image	Phantom placed in the isocenter of scanner
Motor presented	Robot introduced to scanner with power disconnected
Powered, at rest	Robot powered but not actuated
Powered, actuated	Robot powered and actuated

(a) Phantom Image

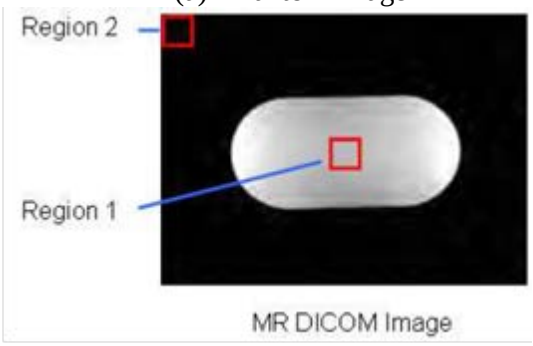

(b) Normalized SNR results

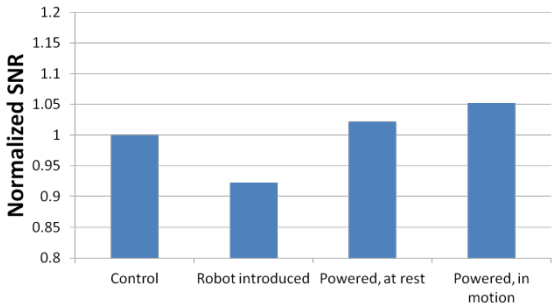

Figure 3.5- (a) MR Image of the phantom, with regions used for SNR calculations (b) SNR results from the 4 test conditions

Open-air Accuracy Testing: Method

Validation of the robot's accuracy was confirmed first on a benchtop, using physical measurements, and secondly inside the gantry, to confirm the resulting position after each move. The positions of the actual needle tips were compared to the positions set by the users (n=32 for benchtop initially, later n=12 in scanner). The needle tip positions during benchtop tests were qualified using an Aurora Electromagnetic tracker (NDI Medical, Waterloo, Ontario), and the mean and standard deviation of the positional error were calculated. The difference between the encoded position and target position was recorded as the targeting error, and the distance between the encoded position and physical position was measured as the positioning error.

Open-air Accuracy Testing: Results

The system parameters used in experiments and validation at NIH had a physical error mean of 0.46mm and a standard deviation of 0.25mm (Fig. 3.6a-b). Automatic control error, the difference between the target point and the reported final position in the control software after automatic control, had an in-plane (transverse) targeting control error mean of 0.29mm and a standard deviation of 0.12mm (Fig. 3.6c-d). A significant component of the error is contributed by the necessity of implementing a deadband in the pneumatic motor control scheme, as the 12-meter long pneumatic lines create significant delay between the motors and the control box.

Prostate Phantom Accuracy Testing: Method

Between benchtop testing and laser catheter trials, tests of the robot occurred in a prostate phantom with a simulated seed placement procedure. This permitted initial testing of the robot and OncoNav planning software before performing ablation. Insertion

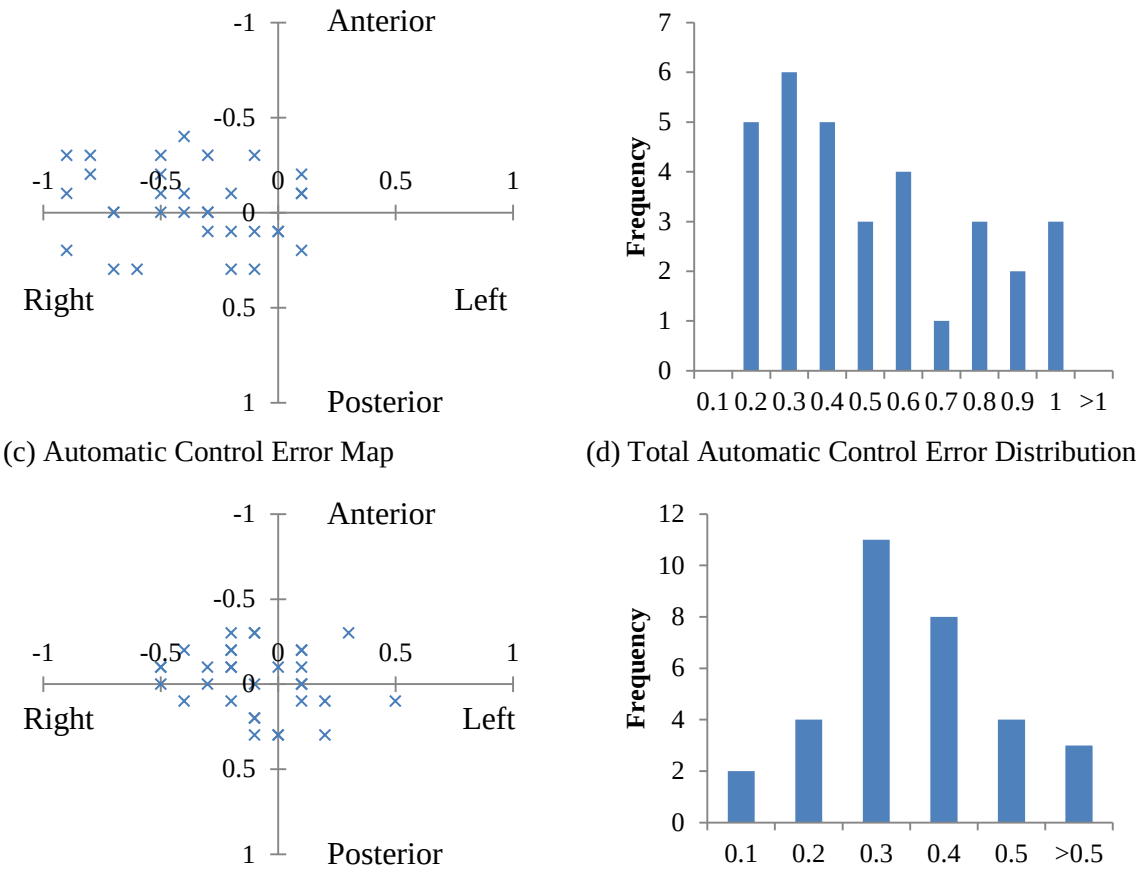

Figure 3.6 - Transverse plane error maps and distributions of total transverse plane error for physical error (a,b) and automatic control error (c,d).

accuracy tests were carried out at NIH utilizing a prostate phantom to simulate brachytherapy seed deposition (Fig. 3.7). Target regions were selected in OncoNav treatment planning software, and the robot adjusted the needle guide accordingly. A needle and sheath were inserted to the target depth and the needle subsequently was removed. Plastic seeds (2mm diameter × 10mm length) were inserted through the sheath by the needle and lodged inside the phantom. Once the seed was implanted, an inverted pyramid pattern optimized the number of seed placements given the relative position of the phantom and robot and a spacing of ~10mm between seeds.

(a) Seed placements (white circle) in prostate phantom

(b) Transverse view & sagittal zoom-in

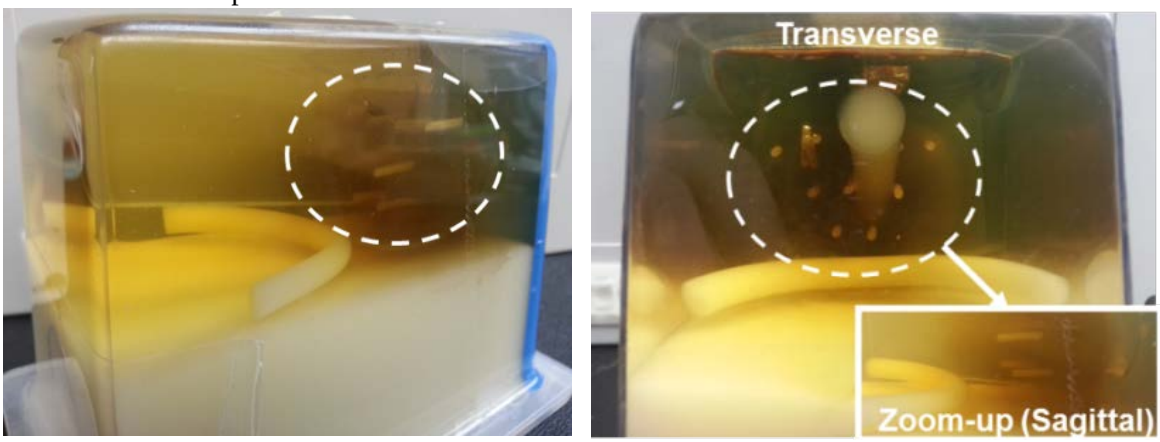

(c) Placement plans overlaid (red boxes)

(d) Placement plans overlaid (red circles)

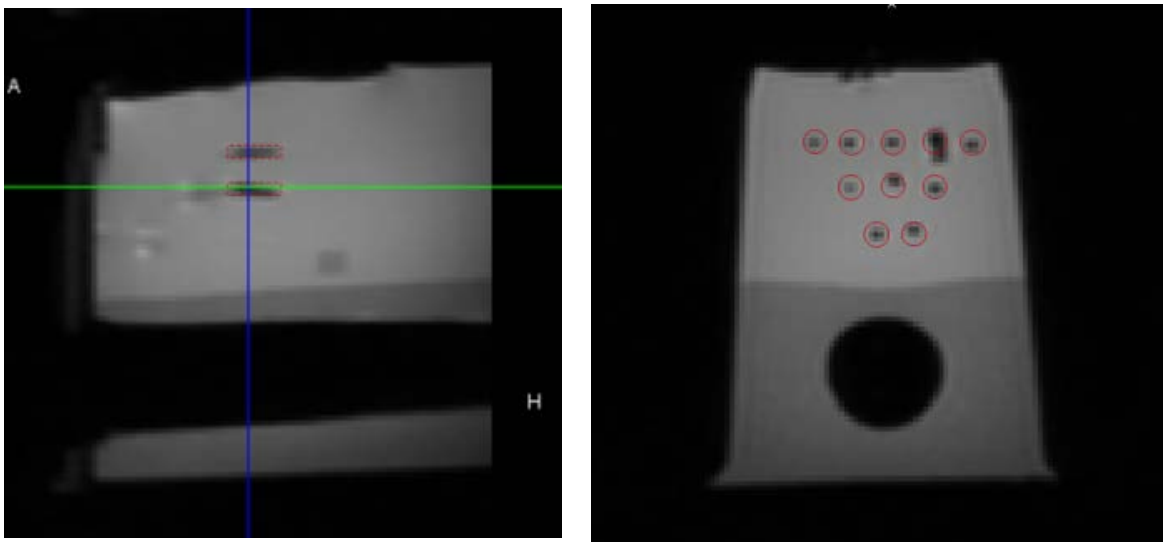

(b) Map of targets and seeds

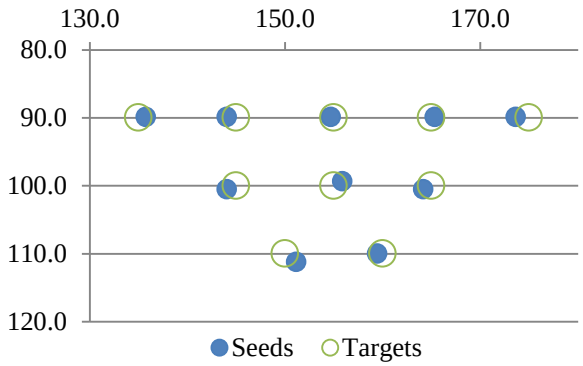

Figure 3.7 - (a) Prostate phantom with inserted seeds visible inside dashed oval. (b) Distribution of targets and seeds for "brachytherapy" insertions.. (c,d) MR images of the embedded seeds. Visible in d is a seed that turned sideways when inserted. (e) distribution of seeds and targets.

Prostate Phantom Accuracy Testing: Results

Derived from MR images, the positioning errors of the seed placements (n=10) had a mean of 0.9mm and a standard deviation of 0.4mm perpendicular to the insertion axis, and a mean of 1.9mm and a standard deviation of 2.7mm along the insertion axis. These errors were calculated from MR images with a voxel area of 1.18x1.18mm for perpendicular error, and a 3.6mm voxel depth for the error along the needle guide. The relatively large slice thickness contributed to some uncertainty with regards to insertion error, and measurements erred on the side of greater error to avoid over reporting accuracy. The inverted pyramid pattern of the seed placement, with a spacing of ~10mm between seeds, is shown in Fig. 3.7d.

Temperature-sensitive Phantom Ablation: Method

A temperature-sensitive phantom was utilized to measure the targeting ability of the laser ablation catheter with robotic guidance at the clinical Philips Achieva 3.0T TX MRI system. Phantoms were made of a low temperature sensitive liposome (LTSL) co-loaded with an MRI contrast agent (ProHance Gd-HP-DO3A) and doxorubicin were used to evaluate the feasibility of the protocol in a phantom study for validation of ablation efficacy [27, 28]. A LTSL formulation containing lyso-lecithin ThermoDox®, (Celsion Corp., USA) with a concentration of 1.8 mg doxorubicin/mL was utilized as the material for the phantom. Doxorubicin hydrochloride (Doxorubicin), zinc sulfate monohydrate (ZnSO4), phosphate buffer saline (PBS), potassium phosphate monobasic (KH2PO4), nitroblue tetrazolium (NBT), magnesium chloride (MgCl2), nicotinamide adenine dinucleotide phosphate (NADPH), and Trifluoroacetic acid were used from Sigma–Aldrich (Saint Louis, MO, USA). The LTSL phantoms change from beige to pink in

areas undergoing laser ablation (light to dark in MR images), allowing real-time and spatial monitoring and evaluation of the ablation efficacy.

MR images of the robot and phantom provided the coordinates of the robot and target points. After inserting the catheter and performing the planned ablation(s), T2W MR images and gross sectioning showed the results of the procedure. System accuracy and efficacy was quantified using virtual tumors designated by the scanner operator inside the phantoms. Overlays of the virtual tumors with MRI thermometry images obtained during the laser ablation provided measurements, giving the targeting accuracy. Comparisons between the thermometry images and gross sections of the phantoms provide visual confirmation of the system's performance.

Temperature-sensitive Phantom Ablation: Results

Measurements of catheter insertion accuracy for the trials in anatomical prostate phantoms with physical tumors (n=5, Fig. 3.8a) and temperature-sensitive phantoms with virtual tumors (n=8, Fig. 3.8b). Insertion accuracy of the catheter relative to the designated target point was under 2mm (μ=1.7mm, σ=0.2mm). Analysis of the ablated regions demonstrated that 100% of the tumor volume was treated in each case, with an extra 10% of the ablated regions lying outside of the calculated ablation ellipsoids.

(a) Anatomical phantom, physical tumor

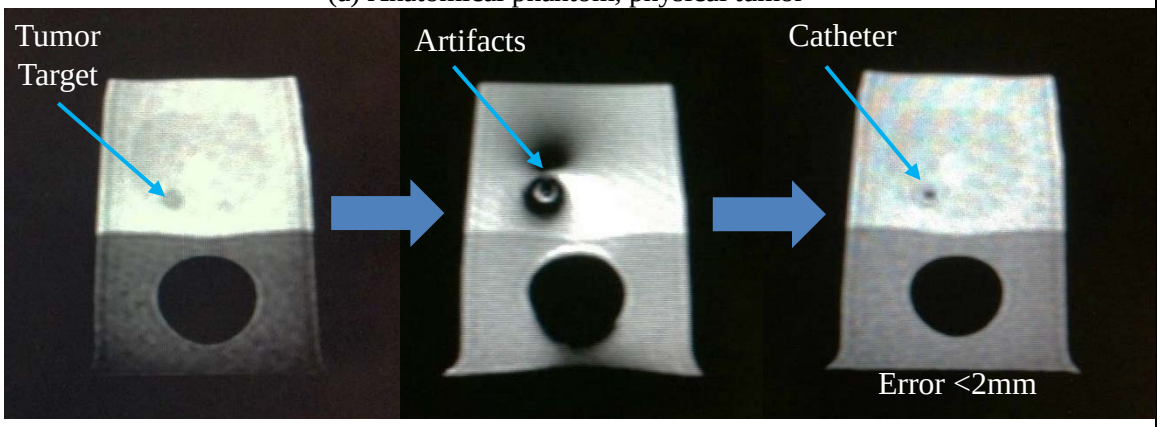

(b) Temperature-sensitive phantom, virtual tumor, pre-ablation

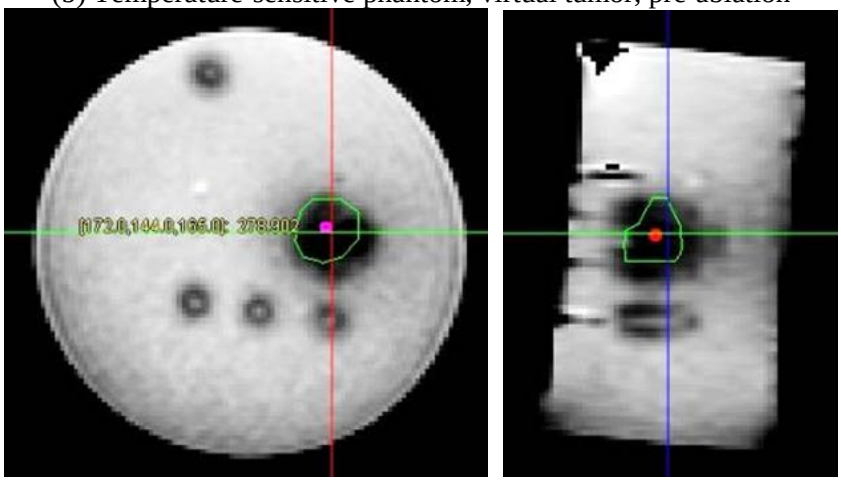

(b) Temperature-sensitive phantom, virtual tumor, post-ablation

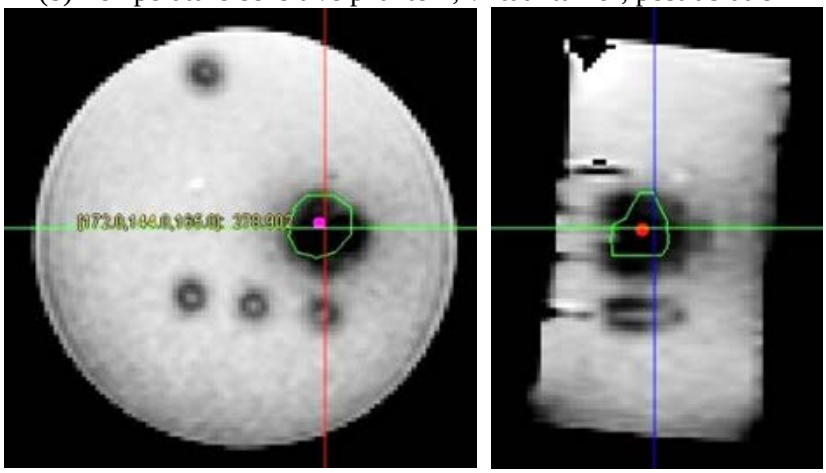

Figure 3.8- (a) An anatomical prostate phantom with tumor visible as darker shade. From left to right: initial phantom image, phantom with titanium trocar and plastic sheath inserted, phantom with catheter and sheath inserted. (b) Tempertature sensitive phantom with created green virtual tumor and white ablation ellipsoids and (c) the burn pattern post-ablation. Previous ablations are visible as well.

Cadaver Trials

Surgical Workflow

Subjects (n=3) were placed in a lateral recumbent position on the MRI gantry (Fig. 3.9). A cooling catheter was prepared and the MRI-compatible robotic platform placed at the anus, just below the tail. Axial MRI scans (3T Philips MR) containing both the prostate anatomy and the perineal guide template were acquired and the OncoNav treatment planning software registered the robotic platform to the canine anatomy. The FLA ablation protocol in prostate patients is summarized in Tables 3.2 and 3.3.

Targets were selected using OncoNav treatment planning software, which provides the appropriate robotic adjustments and calculates the insertion depth of the FLA catheter. The physician starts with the first ablation path using the NIH OncoNav software. The robot is aligned to the desired path, and used to insert an ablation catheter. Since the robot position is known from its mechanical sensors, the MRI plane containing the catheter is displayed in real time to guide the catheter to the planned depth. Ablation takes place under MRI thermometry monitoring and iterative ablation planning is used to adjust the plan based on information from MR T2W and thermometry images.

Results

Despite initial difficulties in traversing the anus and rectum to reach the canine prostate, in all trials the ablation catheter successfully targeted the prostate and ablated the defined targets. Quantification of ablated volume was complicated due to incompletely thawed cadavers, but conservative calculations put ablated volume at 85%, with high-end calculations of coverage meeting 100% and excess of 25% above the target volume.

(a) Subject and robot placement

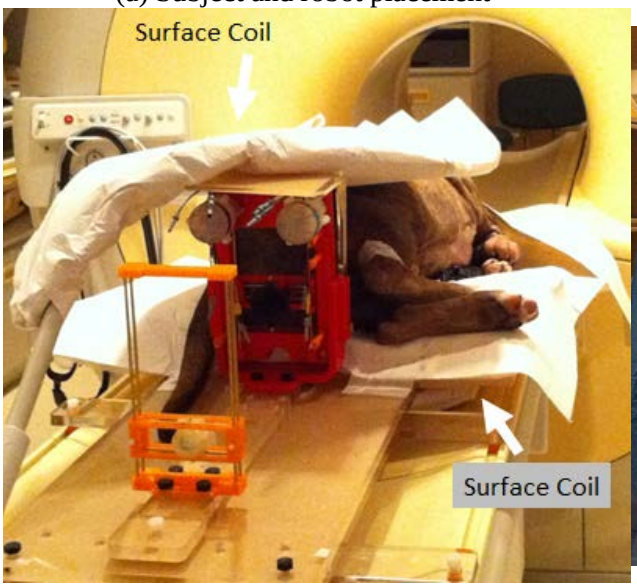

(b) Remote insertion in use

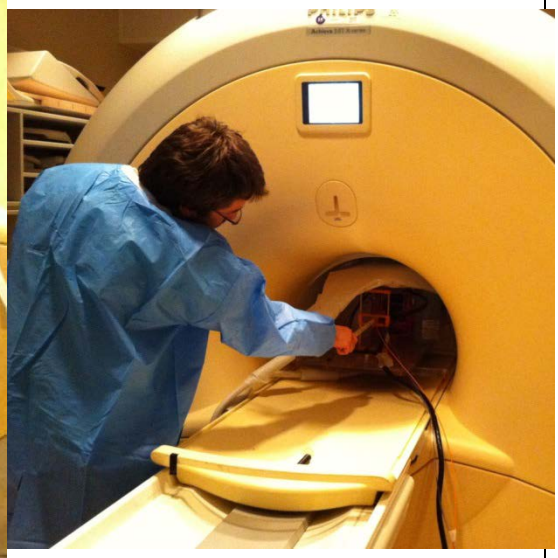

(c) Remote insertion stage in scanner

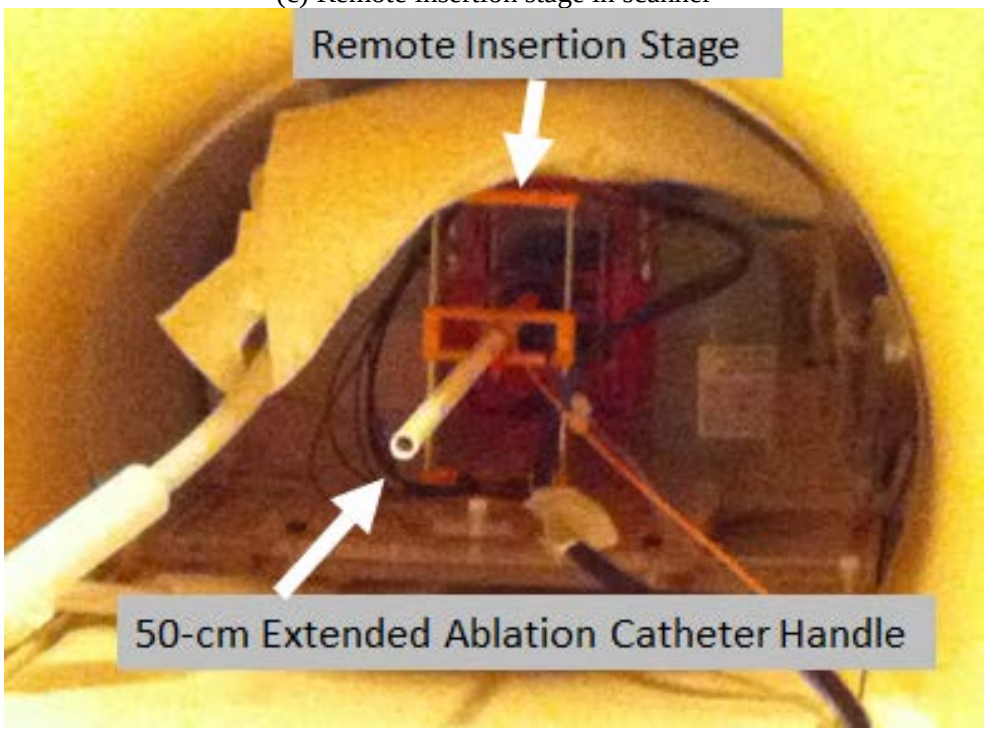

Figure 3.9 – (a) Canine cadaver trial setup. Additional material was wrapped around the body to prevent contamination of the scanner. (b) After finishing insertion of the catheter extension, an operator stands at the bore with their hand flush with the face of the scanner. (c) Robot and cadaver in the MR bore, with the extension arm for catheter insertion visible.

Table 3.2	**Ablation procedure protocol for canine preliminary study**
Step	*Description*
1	The subject was positioned within the MRI unit for the duration of therapy in a lateral recumbent position.
2	An imaging volume containing the needle guidance robot and prostate was chosen, and a T1 planning image acquired.
3	After loading the planning image into the OncoNav treatment planning software, temperature sensitive fast RF-spoiled gradient recalled echo (FSPGRE) images were acquired repeatedly on the MRI and transferred in real time to OncoNav software for the reconstruction of the prostate temperature map.
4	Based on the treatment plan in OncoNav, an ablation position was estimated for optimal coverage of the tumor, after which the robot was moved to the next location for catheter insertion.
5	Ablation takes place under MRI thermometry monitoring with a single lesion requiring between 30 and 240 seconds of laser-radiation at a power level of 6-15 watts.
6	The thermal maps were acquired in real time and sent to OncoNav to validate treatment volume via comparison to the treatment plan and registered tumor volumes.
7	If additional treatments were required (for large, irregular, or multiple tumors), the robotic needle guide was repositioned to the next treatment location and the catheter re-inserted into the new tumor target, repeating **Steps 4-6.**
8	At the end of all laser treatments, post treatment MR images (including dynamic contrast-enhanced T1 as well as T2 weighted images) were acquired for determination of the effective treatment region.

Table 3.3	**Procedure Time**	
Step	*Description*	*Time*
1. System Setup	Physical setup of robot and system in MR suite	20 min.
2. Subject Positioning	Aligning position of subject and robot	10 min.
3. Localizing Scan	Initial scan to determine subject/robot location	5 min.
4. Registration & Anatomy Scan	High-resolution scans of target anatomy and robot fiducials	20 min.
5. OncoNav Targeting	Identification and sectioning of target anatomy	15 min.
6. Robot Adjustment	Aligning robot guide with target point	2 min.
7. Trocar Insertion	Inserting trocar and sheath into patient	2 min.
8. Catheter Insertion	Removal of trocar, insertion of catheter	2 min.
9. Confirmation Scan	Confirming catheter location	5 min.
10. MR Thermometry	Tracking of tissue heating during ablation	5 min.
11. Repeat 6 through 10	For new target or repositioning on current target	15 min.
Total		101 min

Discussion

The developed robotic needle guide met the safety requirements for working in the MR environment and provided full prostate coverage, meeting the needs of the NIH group. Additional utility was added over traditional template-based approaches by adding a continuous workspace and angulation capability for a higher level of targeting flexibility. Testing of the robotic needle guide showed positioning accuracy in the submillimeter range in benchtop and phantom brachytherapy tests. Robot-assisted FLA is therefore possible, and can perform more effective ablations under MRI thermometry monitoring, with fewer unnecessary ablation catheter insertions, lessened chances of untreated zones, reduced MRI-time and reduced complications.

Assesment of the accuraccy of the system requires consideration of the goal of the procedure for which it is being utilized. The high degree of accuracy attained in positioning trials demonstrates utility for performing biopsies, brachtherapy, or other voxel-targeting procedures. Assesment of utility as an aide for ablation is not as stricly dependent on pinpoint accuracy, although it certainly assists in workflow. The complete treatment of the virtual tumors created in OncoNav is the proper standard for successful use. Coupled with minimal overtreatment of the tumors, this result indicates positive results and pormise for use in clinical trials.

The major success of this project was proof that a pneumatic-powered MR-guided robotic system could be designed and fabricated in the lab. Despite the overall success of the system, multiple design decisions led to difficulties during trials and need to be accounted for in future designs. While providing a stronger and more rigid frame, the use of brass rods and components in the design created difficulites when performing

registration and would sometimes cause artifacts when imaging tissue near the robot. Avoiding metal altogether in future robotic designs will eliminate this issue. Motor control proved to be an issue as well, as controlling the positioning of a pneumatic motor at the distal end of a 10 meter pipe via a solenoid valve did not create a favorable environment for fine control. Implementation of a more nuanced control scheme in term of both hardware and software would provide better control, especially when implementing designs which, like a Core-XY platform, require multiple actuators to act in sync to achieve desired motion. The balance between ease of tuning and debugging and the advantages of fixed motors must be weighed when determining which method to use for positioning platforms.

An MRI-compatible robotic needle guide and remote insertion system were tested with the goal of improving available technology for prostate focal laser ablation. This study reports the state of hardware and software development, and presents ablation testing results. The needle guidance robot and remote insertion system were tested as potential assistive technologies for MR imaging-guided and thermometry monitored laser ablations. Custom software, OncoNav, was used for robot-assisted prostate laser ablation with composite treatment planning. Composite treatment planning was performed in canine cadavers to quantify the coverage and efficacy of the ablated volume in an ex-vivo system.

Robot-assisted MRI-guided FLA demonstrates promise by providing accuracy in needle placement and angulation while supplying the ability to perform manually-driven remote insertions for procedure time saving. Ablation of the target volumes was successful with minimal damage to healthy surrounding tissue. The system reduced the

number of subject removals from the scanner, enabling visual and haptic feedback during insertion and reducing the procedure time, which extrapolates to reduced costs in clinical practice. Once reviewed by the Interventional Oncology team at NIH, potential patients will be sought for in vivo trials of the needle guidance robot in conjunction with the remote insertion system.

References

[1] R. Siegel, J. Ma, Z. Zou, and A. Jemal, "Cancer statistics, 2014," *CA: A Cancer Journal for Clinicians*, vol. 64, pp. 9-29, 2014.

[2] O. Raz, M. A. Haider, S. R. Davidson, U. Lindner, E. Hlasny, R. Weersink, *et al.*, "Real-time magnetic resonance imaging–guided focal laser therapy in patients with low-risk prostate cancer," *European urology*, vol. 58, pp. 173-177, 2010.

[3] A. W. Levinson, H. J. Lavery, N. T. Ward, L.-M. Su, and C. P. Pavlovich, "Is a return to baseline sexual function possible? An analysis of sexual function outcomes following laparoscopic radical prostatectomy," *World Journal of Urology*, vol. 29, pp. 29-34, 2011.

[4] F. Fang, N. L. Keating, L. A. Mucci, H.-O. Adami, M. J. Stampfer, U. Valdimarsdóttir, *et al.*, "Immediate risk of suicide and cardiovascular death after a prostate cancer diagnosis: cohort study in the United States," *Journal of the National Cancer Institute*, vol. 102, pp. 307-314, 2010.

[5] U. Lindner, N. Lawrentschuk, R. A. Weersink, S. R. Davidson, O. Raz, E. Hlasny, *et al.*, "Focal laser ablation for prostate cancer followed by radical prostatectomy: validation of focal therapy and imaging accuracy," *European Urology*, vol. 57, pp. 1111-1114, 2010.

[6] "Visualase Image-guided Thermal Laser Ablation Technology in Urology. ," *Available at: http://www.visualaseinc.com/prostate-focal-ablation/,* Accessed March 17, 2014.

[7] M. Stoll, T. Boettger, C. Schulze, and M. Hastenteufel, "Transfer of methods from radiotherapy planning to ablation planning with focus on uncertainties and robustness," 2012.

[8] K. S. Lehmann, B. B. Frericks, C. Holmer, A. Schenk, A. Weihusen, V. Knappe, *et al.*, "In vivo validation of a therapy planning system for laser-induced thermotherapy (LITT) of liver malignancies," *International journal of colorectal disease,* vol. 26, pp. 799-808, 2011.

[9] S. Xu, J. Kruecker, H. Amalou, J. T. Kwak, and B. J. Wood, "Real-time treatment iterative planning for composite ablations," presented at the Computer Assisted Radiology and Surgery 28th International congress and Exhibition, Fukuoka, Japan, 2014.

[10] Z. T. H. Tse, H. Elhawary, A. Zivanovic, M. Rea, M. Paley, B. Graham, *et al.*, "A 3 Degree Of Freedom MR Compatible Device for Magic Angle Related in Vivo Experiments," *ASME/IEEE Transactions on Mechatronics,* vol. 13, pp. 316-324, 2008.

[11] N. M. deSouza, "Magnetic resonance imaging guided breast biopsy using a frameless stereotactic technique," *Clinical radiology,* vol. 51, pp. 425-428, 1996.

[12] K. Hynynen, O. Pomeroy, D. N. Smith, P. E. Huber, N. J. McDannold, J. Kettenbach, *et al.*, "MR Imaging-guided Focused Ultrasound Surgery of

Fibroadenomas in the Breast: A Feasibility Study1," *Radiology,* vol. 219, pp. 176-185, April 1, 2001 2001.

[13] B. T. Larson, A. G. Erdman, N. V. Tsekos, E. Yacoub, P. V. Tsekos, and I. G. Koutlas, "Design of an MRI-Compatible Robotic Stereotactic Device for Minimally Invasive Interventions in the Breast," *Journal of Biomechanical Engineering - Transactions of the ASME,* vol. 126, pp. 458-465, 2004/08/00/ 2004.

[14] G. R. Sutherland, P. B. McBeth, and D. F. Louw, "NeuroArm: An MR Compatible Robot for Microsurgery," *Computer Assisted Radiology and Surgery* vol. 1256, pp. 504-508, 2003.

[15] W. A. Hall, A. J. Martin, H. Liu, E. S. Nussbaum, R. E. Maxwell, and C. L. Truwit, "Brain biopsy using high-field strength interventional magnetic resonance imaging," *Neurosurgery online,* vol. 44, pp. 807-813, 1999.

[16] N. Hata, R. Hashimoto, J. Tokuda, and S. A. Morikawa, "Needle guiding robot for MR-guided microwave thermotherapy of liver tumor using motorized remote-center-of-motion constraint," in *Robotics and Automation, 2005. ICRA 2005. Proceedings of the 2005 IEEE International Conference on*, 2005, pp. 1652-1656.

[17] D. Kim, E. Kobayashi, T. Dohi, and I. Sakuma, "A new, compact MR-compatible Surgical Manipulator for minimally invasive liver surgery," in *The Proceedings of the 5th International Conference on Medical Image Computing and Computer-Assisted Intervention*, Tokyo, Japan, 2002, pp. 164 - 169.

[18] S. H. Heywang, "MR Imaging of the Breast with Gd-DTPA: Use and Limitations'," *Radiology,* vol. 171, pp. 95-103, 1989.

[19] Medtronic. (July 2). *Visualase: MRI-Guided Laser Ablation*. Available: http://www.medtronic.com/for-healthcare-professionals/products-therapies/neurological/laser-ablation/visualase/

[20] R. Seifabadi, "Teleoperated MRI-Guided Prostate Needle Placement," 2013.

[21] J. Cepek, B. A. Chronik, U. Lindner, J. Trachtenberg, S. R. Davidson, J. Bax, *et al.*, "A system for MRI-guided transperineal delivery of needles to the prostate for focal therapy," *Medical Physics*, vol. 40, p. 012304, 2013.

[22] J. Cepek, U. Lindner, S. Ghai, A. S. Louis, S. R. Davidson, M. Gertner, *et al.*, "Mechatronic system for in-bore MRI-guided insertion of needles to the prostate: An in vivo needle guidance accuracy study," *Journal of Magnetic Resonance Imaging*, 2014.

[23] E. Franco and M. Ristic, "Design and control of needle positioner for MRI-guided laser ablation of the liver," in *Mechatronic and Embedded Systems and Applications (MESA), 2014 IEEE/ASME 10th International Conference on*, 2014, pp. 1-6.

[24] Z. T. H. Tse, H. Elhawary, A. Zivanovic, M. Rea, M. Paley, G. Bydder, *et al.*, "A 3-DOF MR-compatible device for magic angle related in vivo experiments," *Mechatronics, IEEE/ASME Transactions on*, vol. 13, pp. 316-324, 2008.

[25] Y. Koethe, S. Xu, G. Velusamy, B. J. Wood, and A. M. Venkatesan, "Accuracy and efficacy of percutaneous biopsy and ablation using robotic assistance under computed tomography guidance: a phantom study," *European radiology*, vol. 24, pp. 723-730, 2014.

[26] K. Chinzei, R. Kikinis, and F. A. Jolesz, "MR compatibility of mechatronic devices: design criteria," in *Medical Image Computing and Computer-Assisted Intervention–MICCAI'99*, 1999, pp. 1020-1030.

[27] A. Ranjan, G. C. Jacobs, D. L. Woods, A. H. Negussie, A. Partanen, P. S. Yarmolenko, *et al.*, "Image-guided drug delivery with magnetic resonance guided high intensity focused ultrasound and temperature sensitive liposomes in a rabbit Vx2 tumor model," *Journal of Controlled Release,* vol. 158, pp. 487-494, 2012.

[28] A. H. Negussie, P. S. Yarmolenko, A. Partanen, A. Ranjan, G. Jacobs, D. Woods, *et al.*, "Formulation and characterisation of magnetic resonance imageable thermally sensitive liposomes for use with magnetic resonance-guided high intensity focused ultrasound," *International Journal of Hyperthermia,* vol. 27, pp. 140-155, 2011.

CHAPTER 4

MANUAL TEMPLATE FOR SPINAL CORD TARGETING

Amyotrophic Lateral Sclerosis

The symptoms of Amyotrophic Lateral Sclerosis (ALS) are due to the progressive degeneration of motor neurons. ALS research in small animal models has shown evidence of axonal regeneration, neural protection, and re-myelination when cells are injected in the ventral horn of the spinal cord near the cervical enlargement [1-5]. These results have encouraged recent human and large animal studies where stem cells are directly injected into the spinal cord. Direct injection cell delivery to the spinal cord parenchyma allows visual confirmation of success, and does not rely on cells migrating to the therapy area [6-9]. Currently, direct injection methods require a multi-level laminectomy and dissection of the dura mater to expose the cord for cell infusion. This approach is acceptable for small trials with patients in the final stages of the disease, but an open surgical approach to direct injection is ultimately undesirable for the field to progress.

The development of imaging-based interventional needle targeting and positioning systems for commercial applications and research settings has been undertaken by numerous sources. Perfint Robio/Maxio, Brainlab Varioguide/iPlan, Stryker Nav3, Innomotion, Accubot, NeuroArm and Steady Hand are a representative sample of such systems [10-13]. The majority of these systems are used in conjunction with CT (computed tomography) or US (ultrasound), which enable high accessibility to

the patient, good needle visualization [14], as well as minimal restrictions on materials. For this study's ultimate goal of delivering cellular therapeutics to the spinal cord, MRI was mandated as the imaging modality for treatment guidance because the specific anatomical locations can only be visualized with MRI. The ventral gray matter horn within the spinal cord is the target for ALS studies performed by the research group, and MRI is required to visualize the contrast between gray and white matter. Similar targeting requirements are necessary to visualize injury or inflammation sites present in patients with ALS. Thus, the plethora of systems which have been developed for CT and US do not meet the requirements of the research group. There are few systems which have been adapted for use within the MRI scanner. The Steady Hand system from John's Hopkins has been used for prostate interventions but has not been adapted to neurologic applications [15, 16]. Studies have been reported for MRI-guided interventions using the Innomotion and NeuroArm systems [17-20]. However both designs are complex and of a large size which takes up the limited space in the MRI bore, requiring a sufficient amount of setup time. Existing template-based systems, such as the InVivo grid localization system as well as the HDR prostate template by SeeDOS, provide a simple mechanism but lack the physical size and angulation capabilities necessary for percutaneous targeting of the spinal cord.

An Initial Manual Approach

Spinotemplate, the initial device developed as part of this project, percutaneously guides therapeutics injections under MRI guidance into the spinal cord, allowing accurate and minimally invasive administration of spinal treatments. The major contribution of this work is enhancing the positioning of the therapeutic injection via an MRI-guided

template-based platform with minimal adjustments to the positioning of the device once on the patient. The template-based guidance enables a simplified workflow for trajectory planning, percutaneous spinal access, therapeutics injections, and subsequent imaging validation, thereby reducing planning time and improving targeting accuracy at the spinal cord. This chapter examines the accuracy and workflow of MRI-guided cellular therapeutics injections using SpinoTemplate.

The core requirements of the SpinoTemplate design stemmed from the surgeons and MRI interventional radiologists who would operate the device at Emory. Their requirements included:

- Fabrication from MR-safe materials, preferably those which do not create image-degrading artifacts in order ensure safety and utility.
- A needle injection (cannula and stylet) must be guided and inserted through the gaps between vertebrae into the spinal cord (Fig. 4.1) so that the procedure can be performed percutaneously, i.e. minimally invasive.
- A 16-gauge cannula is necessary to allow a needle from a microinjection system at Emory to be used.
- Needle insertions are performed by hand in order to obtain realistic force feedback.
- A design capable of performing multiple insertions along an approximately 10cm length of the spinal cord without adjusting fixation to the patient, which reduces procedure time.
- The method of attachment to the surgical structure must be as minimally invasive as feasible, furthering the dissociation from invasive procedures.
- The design shall be simple to operate and must be disposable or able to be sterilized for future in-vivo trials.

(a) Transverse View (b) Sagittal view

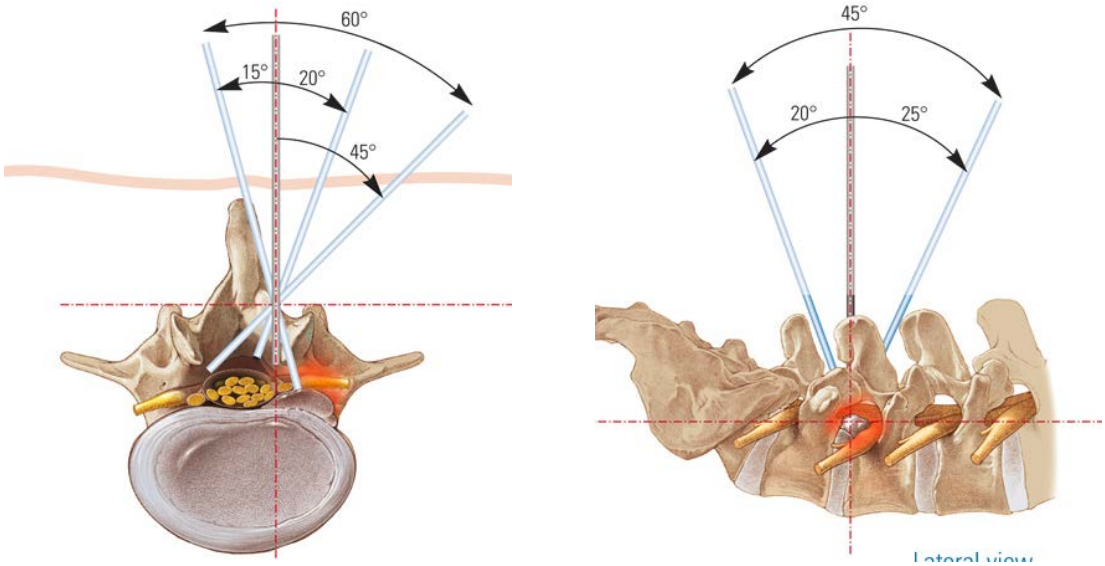

Figure 4.1 - Transverse view showing possible needle paths to enter spinal cord without removing bone [1].

System Design

A template-based positioning and guidance system was determined to be the most efficient way of meeting these requirements (Fig. 4.2a). The positioner consists of two primary components: the template and the support structure. In order to maintain MRI safety and compatibility, all hardware is fabricated from non-metallic and non-magnetizable materials, primarily polyoxymethylene. The support structure serves two purposes: positioning the template and attaching to the patient. The template guides the needle used for cell injection. The support structure contains holes through which pins can be inserted into the template in order to stabilize it at a certain angle. Angles are available in discrete steps of 5˚ between -45˚ and 45˚, with 0˚ being the flat, baseline position. Although a smaller step angle would be ideal, the 5˚ step was chosen to ensure structural rigidity of the support frame and ensure the pins were of sufficient diameter to

not shear if a surgeon applied a large amount of force. The pinning method places all control in the hands of the surgeon, eliminating control and power lines needed for robotic approaches. In combination with the ability to insert a needle to any depth, constrained only by the length of the needle, the guidance system combines aspects of both continuous and discrete workspaces. Within certain transverse planes, the combination of set insertion points along a row in the template with pinning rotation at discrete angles generate a pattern of potential insertion paths which approach continuous coverage at the likely depths of the spinal cord (Fig. 4.3a).

The positioner is designed to attach to living subjects via a neoprene wrap and sutures. The neoprene wrap is similar to waist wraps available at exercise stores, attached to the frame of the support structure. Material is removed within the workspace of the template so that the skin is accessible. The frame has slits and holes designed to allow the positioner to be sutured to the body, providing a less invasive method of affixation than bone screws. For ex vivo trials, an acrylic box and a support structure were substituted in order to contain fluids draining from the subject.

The choice of a template was driven by the need to accurately guide a needle and target as many potential points as possible. The holes in the template are sized to fit a 16 gauge needle. Based on the diameter of the needle, a grid spacing of 3mm was chosen for the holes in the template (Fig. 4.2b), which maintains a balance between the mechanical strength and rigidity of the template and the targeting resolution. The grid of holes spans a distance of approximately 10cm by 11cm, allowing multiple injections along the spinal cord without needing to adjust the attachments of the positioner.

(a) SpinoTemplate at +25˚ (b) Template grid & fiducials

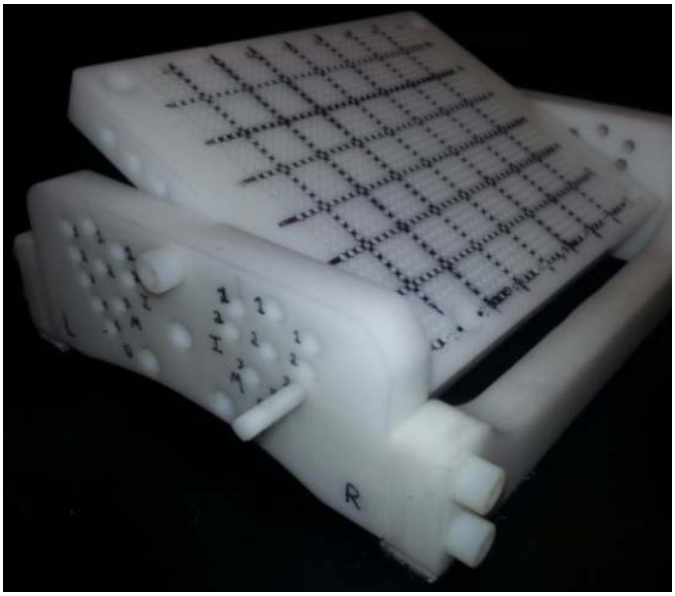

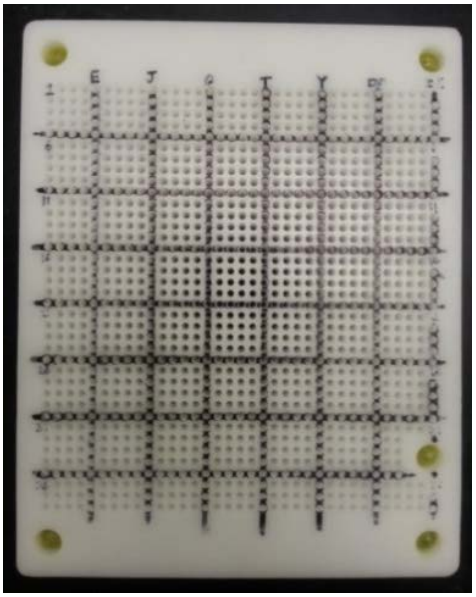

(c) SpinoTemplate on patient (d) Patient in scanner

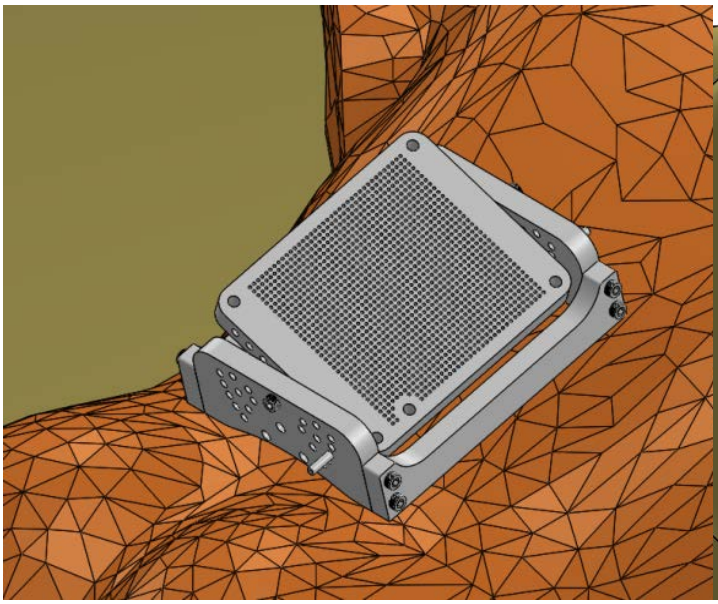

Figure 4.2 - (a) The positioning device, including template and support structure. (b) Top view of template, showing full grid of holes and the five wells with fiducial markers. (c) CAD image demonstrating the positioning of SpinoTemplate above the lumbar spinal cord. (d) Substantial clearance within a 60cm closed-bore scanner.

(a) Possible paths in a transverse plane

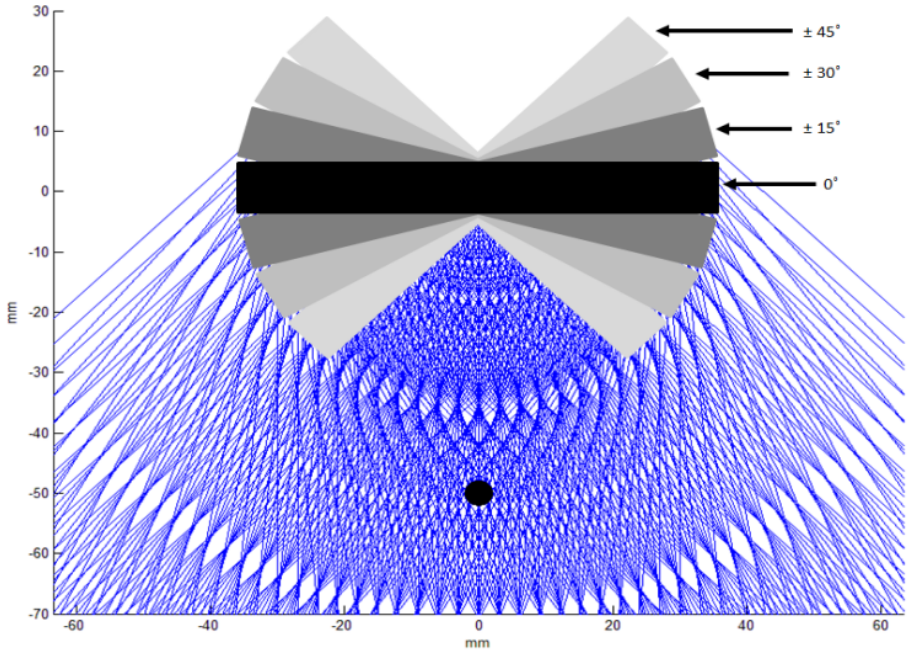

(b) Template axes

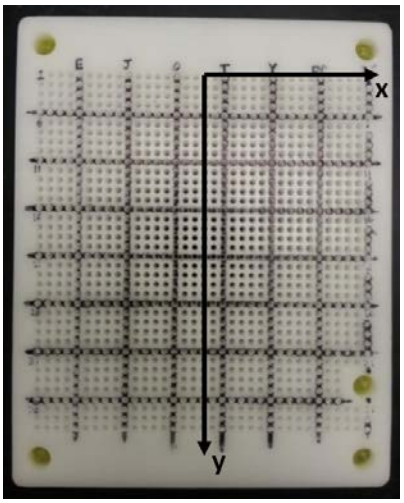

(c) Diagram for targeting solutions

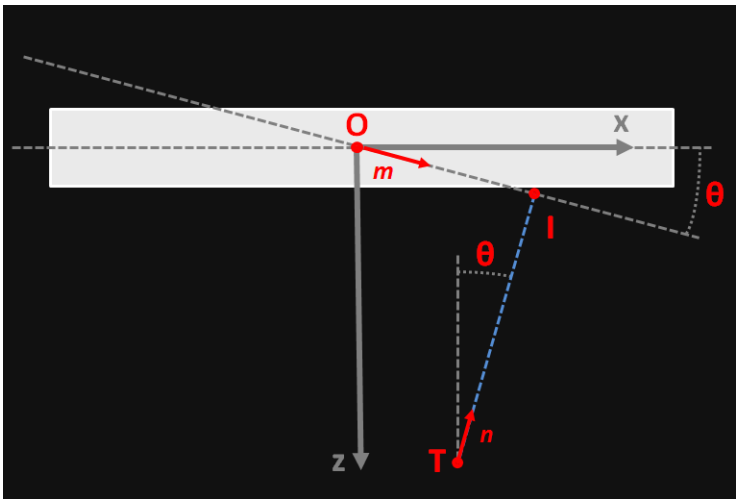

Figure 4.3 - Views of the workspace in the transverse plane. Base of support frame at -40mm. a) Center lines of all possible paths in a transverse plane, with a 4mm diameter-"spine" (black circle). Template (black rectangle) is shown in its 0˚ orientation, as well as additional possible orientations. b) Template with axes overlaid. The y axis runs through the pivot line of the template, while the x axis runs along the top row of the grid. c) Diagram used to solve for targeting parameters once the target, T, is transformed into robot coordinates

Five wells are embedded in the template. The four located in the corners are used for registration of the positioner to MRI coordinates. The fifth well is positioned so that the identities of the registration wells are immediately apparent on the MR images. Fiducial markers (Beekley® PinPoints, ~6mm diameter spheres) appear as bright points on a dark background on the MR images. By entering the coordinates of the center of the markers into custom trajectory calculation software (programmed in LabView™), the positioner can be registered to the MR coordinate system. Registration is done with the template at the 0˚ position. A transformation matrix M is determined by comparing the MRI coordinates of the fiducial markers to the known positions of the fiducials in the template coordinate system. The target point P_{MRI} in the MRI coordinate system is then transformed into $P_{Template}$, the target in the template coordinate system, using M. Targeting equations then give the proper settings (row, column, depth) based on the target's point in the template coordinates and the desired insertion angle. The user is informed if a target is outside of the targetable volume.

After registration has been successfully accomplished, users can select the angle at which to position the template. A target point is selected, and the trajectory calculation software software provides the hole (in the form of a numerical row and alphabetical column) on the template and the length of the needle which will provide the most accurate targeting result, based on the template's angle. It is also possible to dictate the angle, based on the target point and a point along the needle's trajectory. A brass needle was used in tests for visualization as brass was found to provide an easily identifiable signal void while producing minimal artifacts to affect surrounding tissue or phantom matter.

Workflow

Several trials were spent optimizing the workflow of the procedure to successfully advance the needle to reach the target in geometric phantoms and ex-vivo swine spines. The workflow is listed below.

1. SpinoTemplate was mounted above the subject, via support blocks and Velcro for phantom trials and excised ex vivo samples, and a neoprene wrap and for other ex vivo samples. An MR surface coil was laid over the platform and subject.
2. High-resolution images of the spine (Fig. 4.5) and fiducial markers embedded in the platform were made using a 3D, magnetization-prepared, T1-weighted (T1w) fast gradient echo sequence (MP RAGE).
3. The images were analyzed to determine an acceptable intra-laminar gap through which the needle would be inserted in order to reach the target point. The target point and desired angle were entered into the targeting software, which reports the necessary settings on the platform and needle. The template angle was then adjusted to match the desired trajectory and the proper template hole was identified.
4. The 16 gauge rigid outer cannula with a rigid central stylet was advanced manually. The stylet was removed and gadolinium injected through the cannula. Alternately, a solid brass needle was inserted.
5. The needle was extracted and a T2*-weighted gradient echo sequence confirmed the location of the needle tract for gadolinium injections. For brass needle trials, the needle was kept in the subject during imaging and the artifact used to identify the needle trajectory.
6. Steps 3-5 are repeated for each insertion.

Workspace Analysis and Targeting

Figure 4.3 shows the needle targeting workspace of the SpinoTemplate. Within the transverse planes aligning with the template, the design of the template creates a high density of potential targeting paths are arranged between 40mm and 70mm below the template (0mm to 30mm below the support frame), providing numerous targeting angles and insertion depths for the target anatomy (e.g. circle in Fig. 4.3a). The locations of the template holes and the angulation position result in a maximum targeting error of 1.5mm between transvers planes and 1.2mm between planes. However, this resolution is effectively reduced in all but a narrow band at 70mm below the template, with an in-pane maximum error under 0.5mm, due to the convergence of multiple targeting angles at the target depth.

Definition of axes is shown in Fig. 4.3c-d. Based on a user-selected insertion angle, the following equations were used to relay to the user which row and column on the grid should be used for the insertion, and how much of the needle should be inserted. Additional checks were implemented to report if the target point, *T*, was beyond the targetable volume.

$$I_x = \|m\| cos\theta = T_x + \|n\| sin\theta$$

$$I_z = \|m\| sin\theta = \mathrm{T}_z - \|n\| cos\theta$$

$$\begin{bmatrix} T_x \\ T_z \end{bmatrix} = \begin{bmatrix} cos\theta & -sin\theta \\ sin\theta & cos\theta \end{bmatrix} \begin{bmatrix} \|m\| \\ \|n\| \end{bmatrix}$$

$$\mathrm{Row} = \frac{\sqrt{I_x^2 + I_z^2} + 54}{3}$$

$$\mathrm{Column} = \frac{T_y}{3} + 1$$

$$\mathrm{Insertion\ Depth} = \sqrt{(I_x - T_x)^2 + (I_z - T_z)^2} + \frac{template\ thickness}{2}$$

System Validation

The template was tested in a model of pyramid phantom arrays (Fig. 4.4a-b), ex-vivo mature swine spines (Fig. 4.4d, Fig. 4.5b-c) and euthanized piglets (Fig. 4.5a), with a resulting system median targeting accuracy of 2.1 mm. With the 16-gauge needle used for the study, this error is equivalent to slightly over 1.2 needle diameters.

Results of the system targeting error are shown in Fig. 4.6. Preliminary results showed successful MRI-guided injections in ex-vivo swine spines. In all ex-vivo trials, the needle was successfully guided between the vertebrae into the spinal cord. The results from piglet trials indicate transverse error under 1mm and axial error less than 2mm. Voxel size for the images used in these calculations was 0.43mm×0.43mm×1.0mm.

The procedure requires approximately 35 minutes to complete a single injection, which includes template setup, attachment of the template to the subject, template-scanner registration, target localization, trajectory planning, needle injections and confirmation scans. The registration and anatomy scans were valid for further injections, resulting in only the duplication of trajectory planning and needle insertion in additional injections. This resulted in an average of additional 5 minutes per additional injection during a procedure.

(a) Targeting phantom

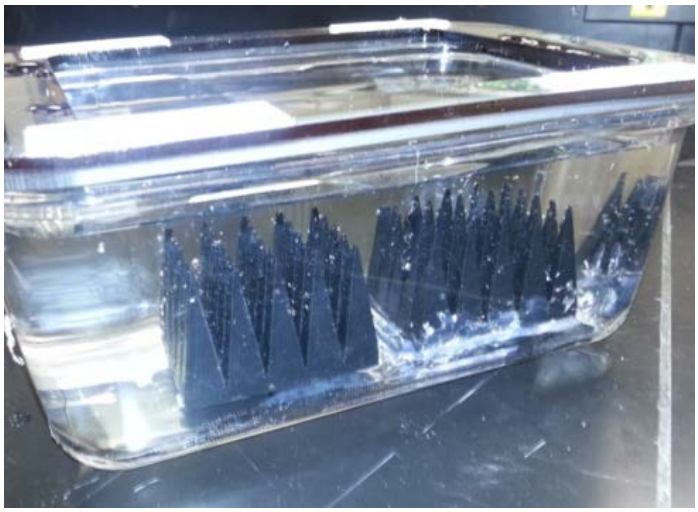

(b) Phantom in MRI

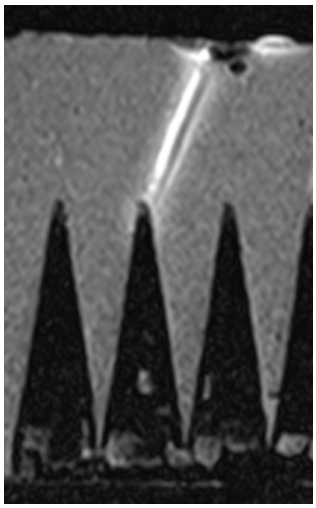

(c) Measured errors

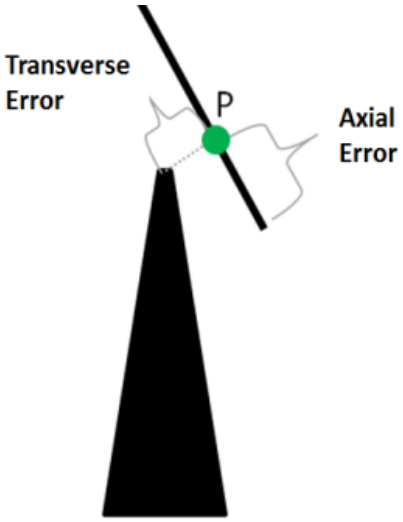

(d) Template in ex-vivo study

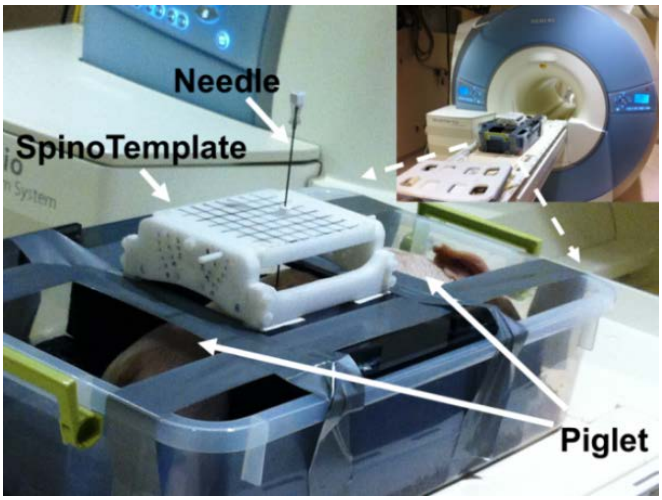

Figure 4.4 - (a) 3D-printed plastic pyramid phantom model for quantification of the needle targeting error. (b) MR images showing pyramid tip targeted by the needle. (c) Targeting errors were measured in both transverse and axial directions of the needle related to pyramid tip. (d) SpinoTemplate mounted above an ex-vivo sample of swine lumbar spine

(a) Sagittal ex-vivo MR image

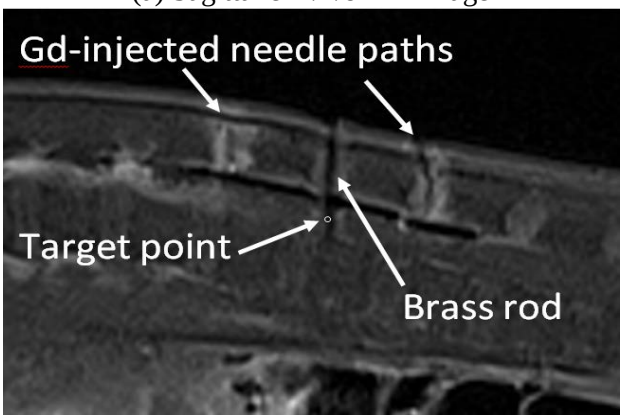

(b) Transverse ex-vivo MR image

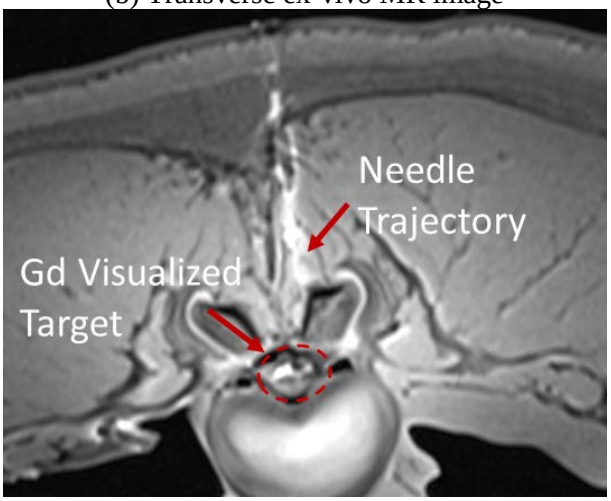

(c) Sagittal ex-vivo MR image

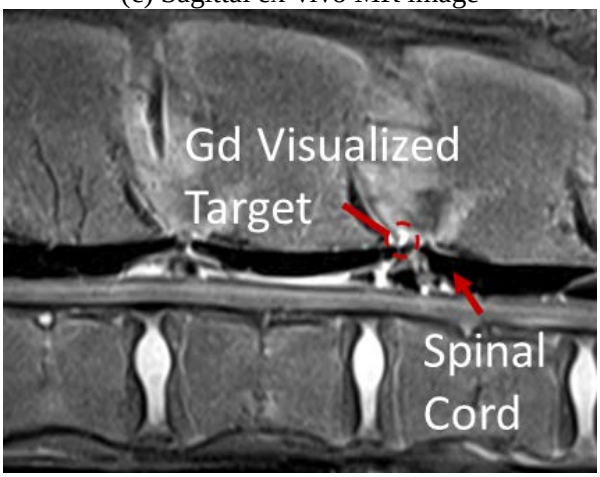

Figure 4.5 - (a) Sagittal image of ex-vivo piglet trial showing an inserted brass rod used targeting validation. Target point is inside spinal cord. (b) Transverse image of ex-vivo lumbar section after targeting and injection of gadolinium (c) Sagittal image showing gadolinium and drainage of CSF space

(a) Targeting error along different axes

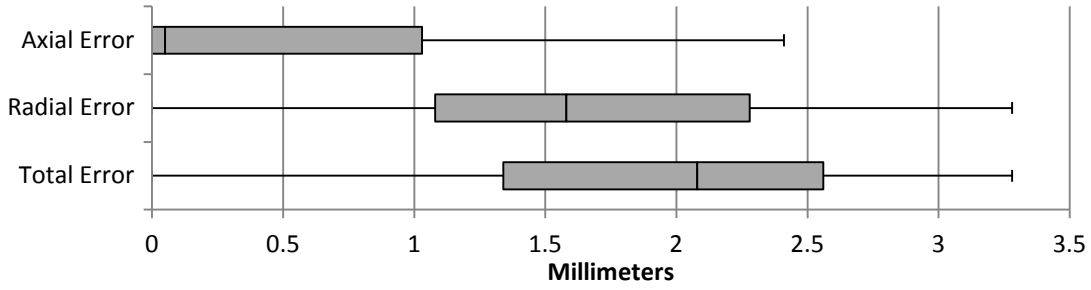

(b) Needle Radial Error

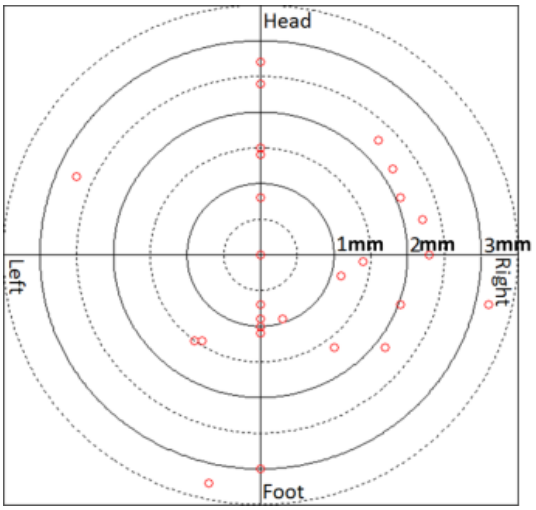

(c) Needle Axial Error

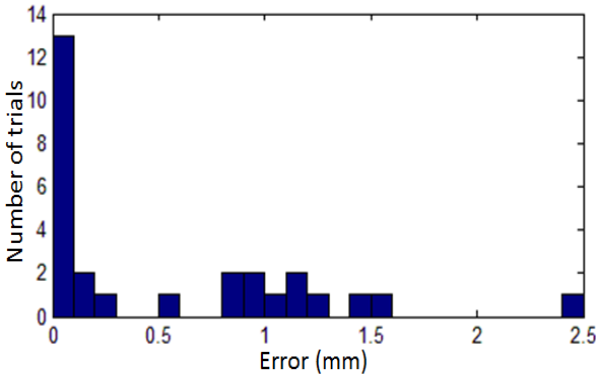

Figure 4.6 -Plots of the needle targeting error in phantom studies. a) Quartile plot of overall targeting error. b) Plot of radial error. Solid rings every millimeter, dashed rings every 0.5 millimeters. c) Axial/insertion error

Discussion

The major conclusion from SpinoTemplate was that targeting of specific locations in a pyramid phantom model, ex-vivo mature swine spines, and euthanized piglets were all possible to accomplish in a straightforward and accurate manner. This study showed promise as a stepping stone in developing a robotic MR-guided therapeutic delivery system as part of a minimally invasive procedure to infuse cells into the ventral horn of the spinal cord, as well as other regions along the length of targetable spinal tissue. While

the end goal of the spinal study is a robotic guide, the development of SpinoTemplate offers an alternative to available MR-compatible interventional robots. More complex manipulators require extensive set-up and complex hardware and software to operate, while SpinoTemplate is kept intentionally simple to offer ease of use. Adding a second rotation axis would offer the benefit of additional targeting paths, but slightly increase the complexity of the device; the increased paths outweigh the cost, however, and would be included in future version of SpinoTemplate development, should that arise.

The next step in this project's evolution, the SpinoBot, certainly will require the 4^{th} axis to provide full targeting coverage. The registration and targeting algorithm of the SpinoTemplate are based solely upon the gadolinium markers mounted on the template, allowing the supporting structure to be redesigned to allow use in subjects of differing sizes or completely different species, enhancing the value of the template via its flexibility as a surgical platform. Discussions with members of the Emory team have encouraged the use of such modular abilities in future SpinoBot designs, whether for registration, fixation, or other areas.

Ex vivo trials and discussion with Emory surgeons have shown that puncturing the lamina surrounding the spinal cord requires a significant amount of force, potentially lending value to developing a motorized insertion axis as the application farce can be carefully regulated. Furthermore, each insertion requires the patient to be removed from the scanner bore for the physical procedure id done by hand, increasing the overall time required for the procedure. A motorized insertion axis may be a desirable feature particularly when multiple insertions are planned. Unnecessary patient movement can also be reduced, which minimizes the possibility of registration error which can affect the

geometry of the patient's anatomy relative to the template. However, use of a motorized insertion axis causes more complicated ease of use and regulatory concerns, and is not high on the list of potential additions to this project.

References

[1] M. Asheuer, F. Pflumio, S. Benhamida, A. Dubart-Kupperschmitt, F. Fouquet, Y. Imai, *et al.*, "Human CD34+ cells differentiate into microglia and express recombinant therapeutic protein," *Proc Natl Acad Sci U S A*, vol. 101, pp. 3557-62, Mar 9 2004.

[2] J. Goolsby, M. C. Marty, D. Heletz, J. Chiappelli, G. Tashko, D. Yarnell, *et al.*, "Hematopoietic progenitors express neural genes," *Proc Natl Acad Sci U S A*, vol. 100, pp. 14926-31, Dec 9 2003.

[3] M. Hoehn, E. Kustermann, J. Blunk, D. Wiedermann, T. Trapp, S. Wecker, *et al.*, "Monitoring of implanted stem cell migration in vivo: a highly resolved in vivo magnetic resonance imaging investigation of experimental stroke in rat," *Proc Natl Acad Sci U S A*, vol. 99, pp. 16267-72, Dec 10 2002.

[4] A. Taguchi, T. Soma, H. Tanaka, T. Kanda, H. Nishimura, H. Yoshikawa, *et al.*, "Administration of CD34+ cells after stroke enhances neurogenesis via angiogenesis in a mouse model," *J Clin Invest*, vol. 114, pp. 330-8, Aug 2004.

[5] Z. M. Zhao, H. J. Li, H. Y. Liu, S. H. Lu, R. C. Yang, Q. J. Zhang, *et al.*, "Intraspinal transplantation of CD34+ human umbilical cord blood cells after spinal cord hemisection injury improves functional recovery in adult rats," *Cell Transplant*, vol. 13, pp. 113-22, 2004.

[6] J. D. Glass, N. M. Boulis, K. Johe, S. B. Rutkove, T. Federici, M. Polak, *et al.*, "Lumbar intraspinal injection of neural stem cells in patients with amyotrophic lateral sclerosis: results of a phase I trial in 12 patients," *Stem Cells,* vol. 30, pp. 1144-51, Jun 2012.

[7] L. Mazzini, I. Ferrero, V. Luparello, D. Rustichelli, M. Gunetti, K. Mareschi, *et al.*, "Mesenchymal stem cell transplantation in amyotrophic lateral sclerosis: A Phase I clinical trial," *Exp Neurol,* vol. 223, pp. 229-37, May 2010.

[8] L. Mazzini, K. Mareschi, I. Ferrero, M. Miglioretti, A. Stecco, S. Servo, *et al.*, "Mesenchymal stromal cell transplantation in amyotrophic lateral sclerosis: a long-term safety study," *Cytotherapy,* vol. 14, pp. 56-60, Jan 2012.

[9] J. Riley, T. Federici, M. Polak, C. Kelly, J. Glass, B. Raore, *et al.*, "Intraspinal stem cell transplantation in amyotrophic lateral sclerosis: a phase I safety trial, technical note, and lumbar safety outcomes," *Neurosurgery,* vol. 71, pp. 405-16; discussion 416, Aug 2012.

[10] G. R. Sutherland, P. B. McBeth, and D. F. Louw, "NeuroArm: an MR compatible robot for microsurgery," *International Congress Series,* vol. 1256, pp. 504-508, 6// 2003.

[11] F. Ringel, D. Ingerl, S. Ott, and B. Meyer, "VARIOGUIDE: A NEW FRAMELESS IMAGE-GUIDED STEREOTACTIC SYSTEM—ACCURACY STUDY AND CLINICAL ASSESSMENT," *Neurosurgery,* vol. 64, pp. ons365-ons373, 2009.

[12] J. Maderer and M. Feeney, "Putting the Right Face on an Assistive Robot," *Biomedical Safety & Standards,* vol. 44, pp. 113-114, 2014.

[13] K. Cleary, A. Melzer, V. Watson, G. Kronreif, and D. Stoianovici, "Interventional robotic systems: Applications and technology state-of-the-art," *Minimally Invasive Therapy & Allied Technologies,* vol. 15, pp. 101-113, 2006/01/01 2006.

[14] A. Bertelsen, J. Melo, E. Sánchez, and D. Borro, "A review of surgical robots for spinal interventions," *The International Journal of Medical Robotics and Computer Assisted Surgery,* vol. 9, pp. 407-422, 2013.

[15] R. Taylor, P. Jensen, L. Whitcomb, A. Barnes, R. Kumar, D. Stoianovici, *et al.*, "A Steady-Hand Robotic System for Microsurgical Augmentation," in *Medical Image Computing and Computer-Assisted Intervention – MICCAI'99*. vol. 1679, C. Taylor and A. Colchester, Eds., ed: Springer Berlin Heidelberg, 1999, pp. 1031-1041.

[16] Y. Koethe, S. Xu, G. Velusamy, B. Wood, and A. Venkatesan, "Accuracy and efficacy of percutaneous biopsy and ablation using robotic assistance under computed tomography guidance: a phantom study," *European Radiology,* vol. 24, pp. 723-730, 2014/03/01 2014.

[17] A. Melzer, B. Gutmann, T. Remmele, R. Wolf, A. Lukoscheck, M. Bock, *et al.*, "INNOMOTION for percutaneous image-guided interventions: principles and evaluation of this MR- and CT-compatible robotic system," *IEEE Eng Med Biol Mag,* vol. 27, pp. 66-73, May-Jun 2008.

[18] C. Lacey and G. Sutherland, "Advancing neurosurgery through translational research," *Neurosurgery,* vol. 72 Suppl 1, pp. 176-81, Jan 2013.

[19] A. Mert, L. S. Gan, E. Knosp, G. R. Sutherland, and S. Wolfsberger, "Advanced cranial navigation," *Neurosurgery,* vol. 72 Suppl 1, pp. 43-53, Jan 2013.

[20] G. R. Sutherland, S. Wolfsberger, S. Lama, and K. Zarei-nia, "The evolution of neuroArm," *Neurosurgery*, vol. 72 Suppl 1, pp. 27-32, Jan 2013.

CHAPTER 5

DEVELOPMENT OF A ROBOT FOR SPINE INTERVENTIONS

Progression to an Actuated System

The device presented in this chapter, SpinoBot, build on the previous manual template by providing continuous translational coverage of the targeting volume in conjunction with discrete angulation capabilities around two axes of rotation. The major contribution of this work was enhancing the positioning of the therapeutic injection via an MRI-guided template-based platform while maintaining minimal adjustments to the positioning of the device once on the patient. This chapter examines the accuracy and workflow of MRI-guided cellular therapeutics injections using SpinoBot.

Hardware Design

The design of Spinobot (Fig. 5.1a,b) was performed under the specifications listed in Table 5.1 after consultations with the interventional radiologist and neurosurgeon in the team. The robot is designed to provide multiple insertion angles along a 10cm section of spinal cord. To accomplish this goal, 2 motorized degrees of freedom provide translation along the robot's X and Y axes, offering 60mm of lateral motion and 140mm of head-foot motion respectively. Needle angulation is achieved through a passive radial template (Fig. 5.2a), which offers ±20˚ of rotation off of vertical in 4˚ increments. The guidance paths in the template converge at an RCM located 10mm below the rails of the robot; this distance positions the RCM in the approximate depth of the spine (Fig. 5.2b), minimizing the fine-tuning adjustments needed if a surgeon chooses

a different needle path. This template maintains the angulation capabilities and simplicity of the manual template [1], while increasing its coverage via mounting on a frame with continuous translation.

The frame of the robot is designed to be able to mount directly to a subject [2]. In the trials presented below, this was via direct mounting to a testing grid or the container for a cadaver specimen. Lower grooves in the rails of the frame provide a mounting point for spinal attachment components for live trials. Bars stretch over the moving components of the robot to allow a body coil to be strapped on top of the robot while still maintaining its ability to maneuver. On the long axis of the frame, upper grooves held the positioning sled in place. A timing belt stretched between fixed points along the Y axis. The timing belt and motor for the X axis were on the positioning sled. The X axis belt directly manipulated the template support, into which the template was inserted. A removable template permits efficient redesigns of the end effector.

Table 5.1	**Design specifications of the robot**
Designed with MR safe materials, preferably completely non-metallic	
Guide an injection into the spine percutaneously	
Constrain a 16-gauge cannula from a microinjection system to allow stem cell infusions	
Attach to a subject in a minimally invasive fashion	
Perform targeting along at least 10cm of spinal cord without remounting the robot	
Translational positioning of the needle in the head-feet and left right directions of the patient.	
Rotational positioning of the needle (in pitch and yaw directions) is used for <5% of spinal patients, therefore motorized rotational stages are not necessary.	
Relative ease of operation	
Work across multiple imaging suites from differing vendors	
Removable end stage for ease of sterilization	

(a) Assembled robot, isometric view

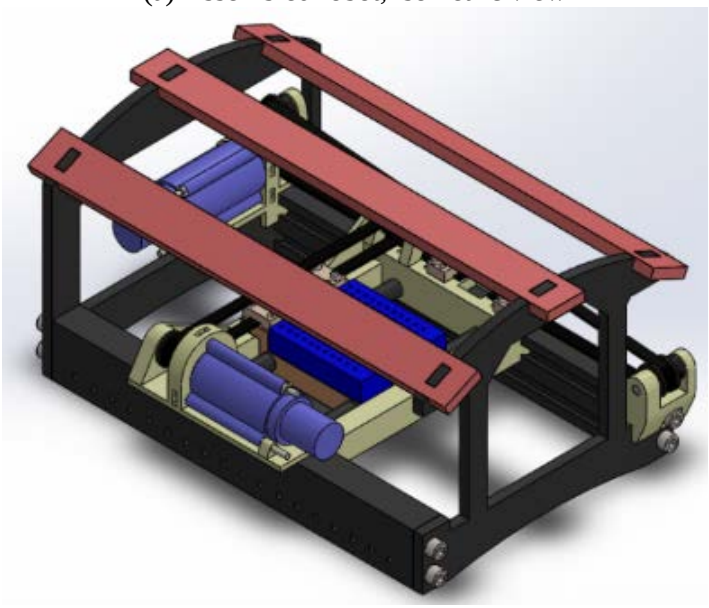

(b) Exploded view

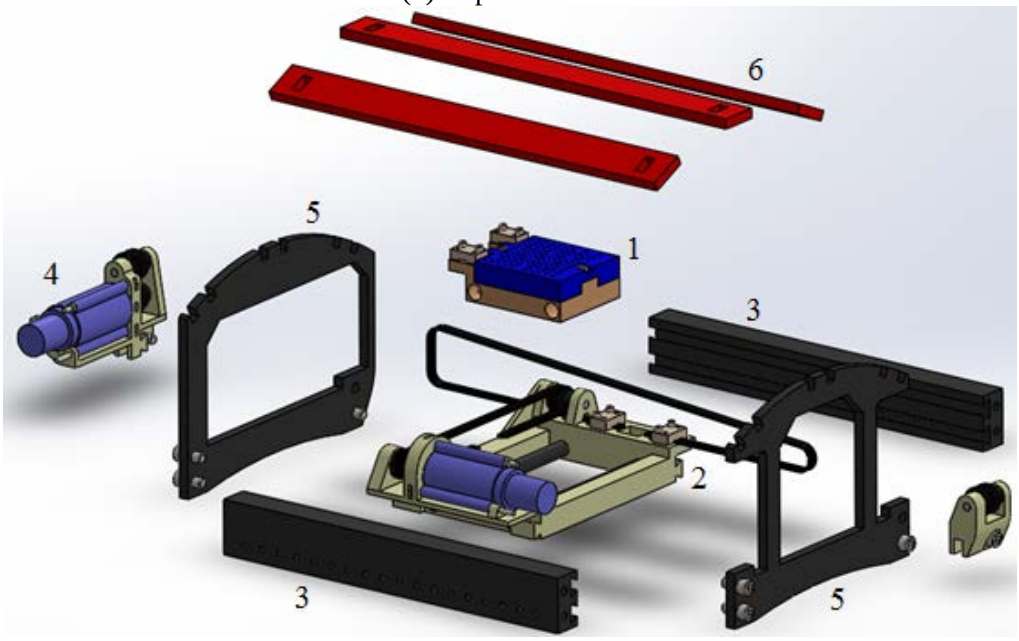

Figure 5.1 - (a) Isometric view of the assembled system. (b) Partially exploded view of the robot, highlighting 1) radial template and lateral sled, 2) lateral motor and belts on longitudinal sled, 3) frame rails, 4) longitudinal motor, 5) frame caps, and 6) coil support bars.

(a) Radial template, isometric view

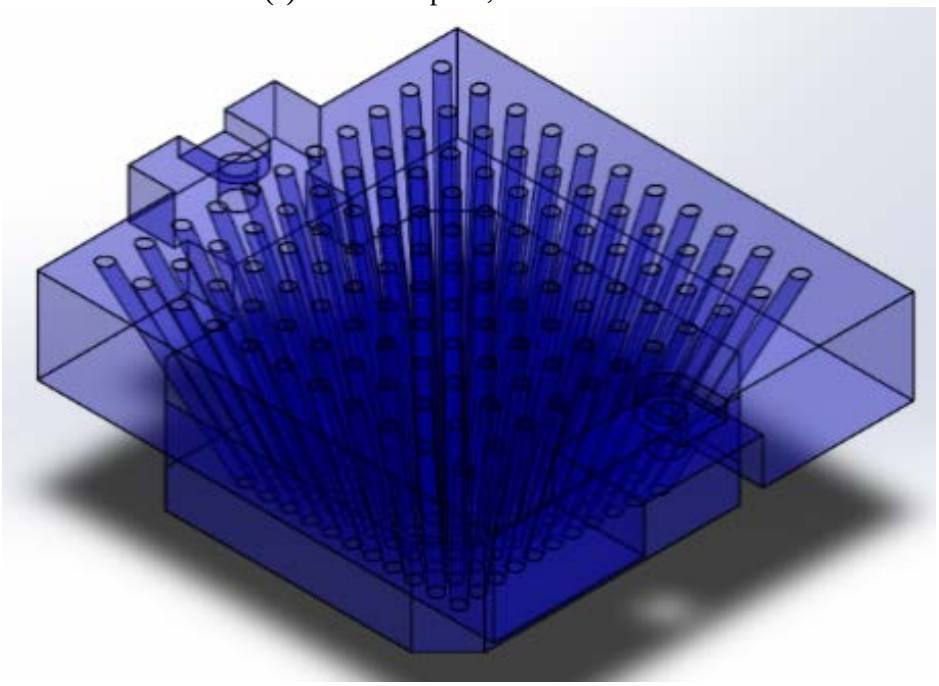

(b) Robot workspace in green

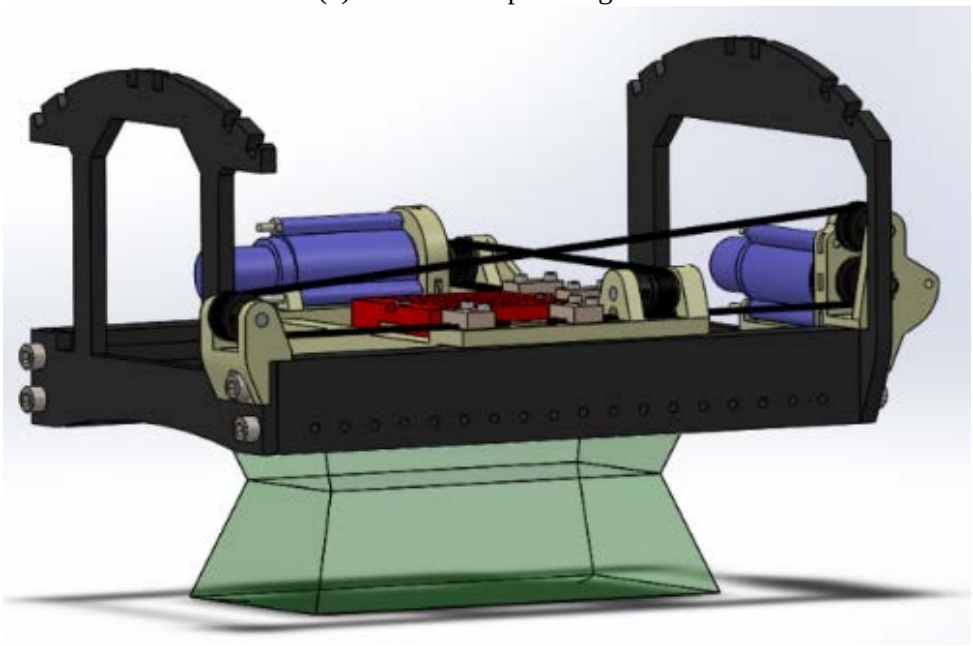

Figure 5.2 - (a) The radial template used for achieving multiple targeting angles, shown as transparent for better visualization of the needle paths. (b) The workspace of a 100mm needle, shown in green.

(a) Assembled robot, isometric view

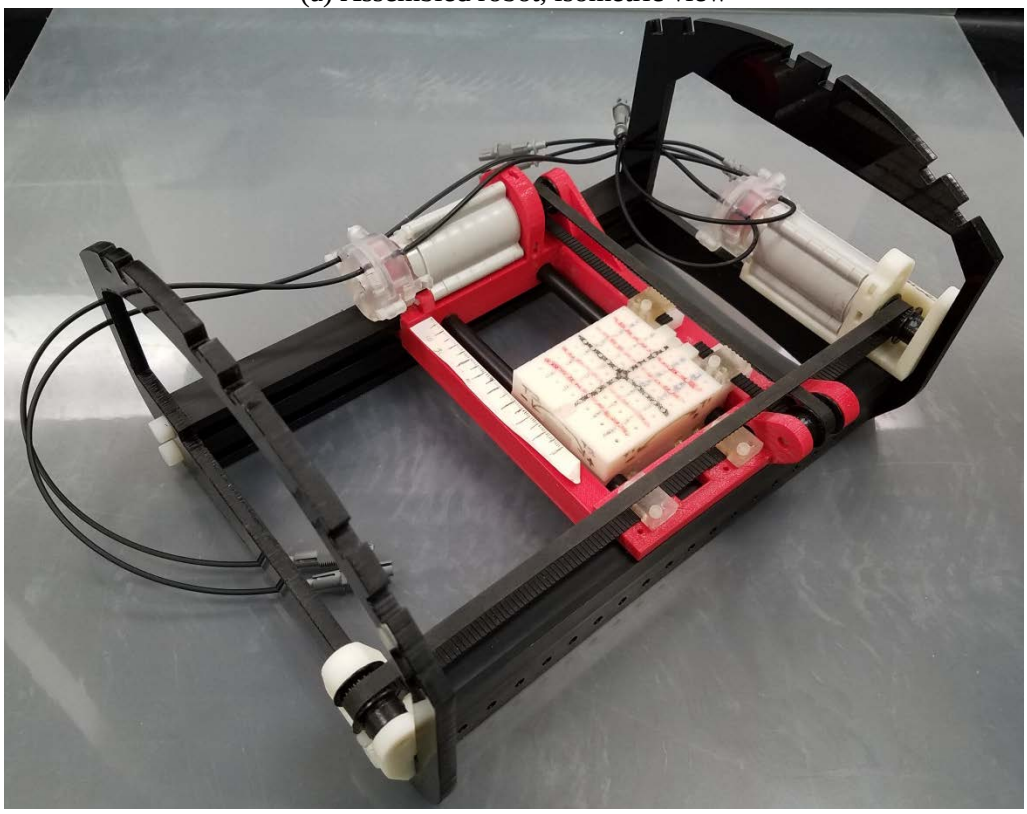

(b) Assembled robot from foot

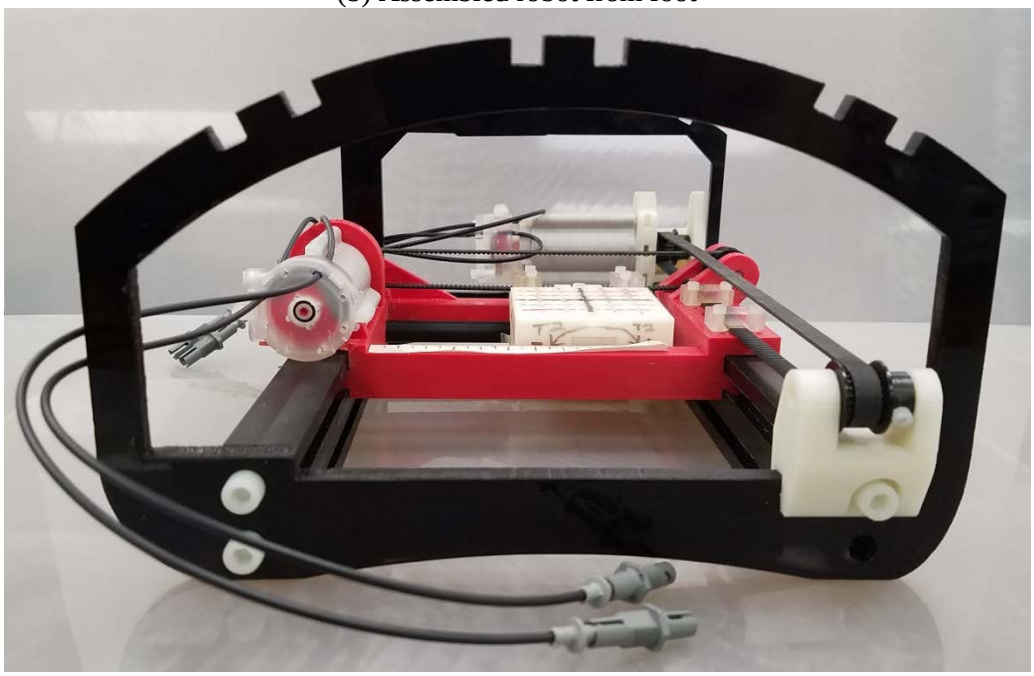

Figure 5.3 – Views of the assembled robot.

Actuation was provided by an updated design of a fixed-vane pneumatic motor (Fig. 5.3) used in previous projects [3, 4]. The size of the motor was reduced to match the form factor of hobby DC motors (24 mm in diameter, 2.7mm in height, Fig. 2.3b). Fiber optic channels and encoding method remained the same.

The workspace of the robot forms a rectangular hourglass shape centered underneath the frame. The narrowest point of the hourglass falls in the XY plane of the

(a) Motor with all connecting lines

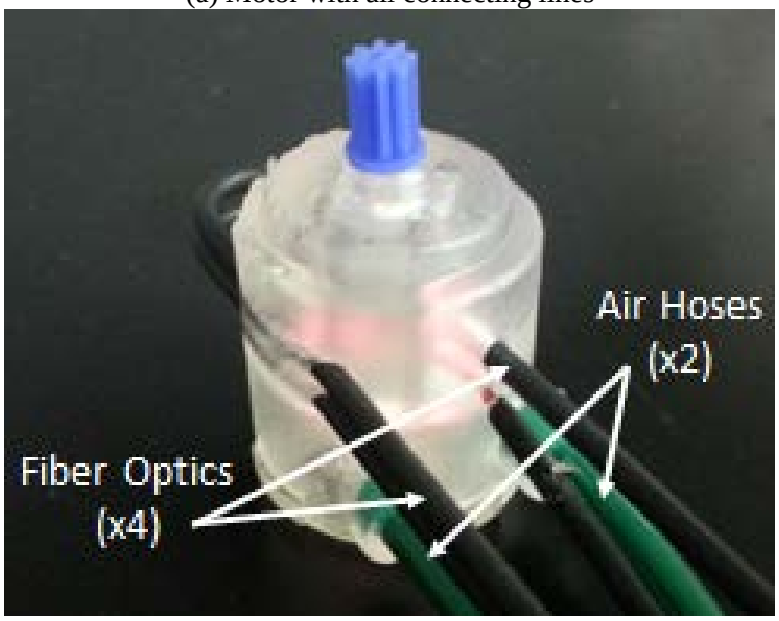

(b) Motor assembly

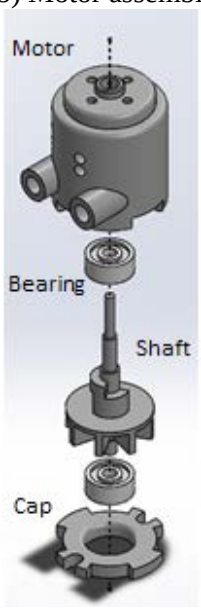

(c) Size comparison

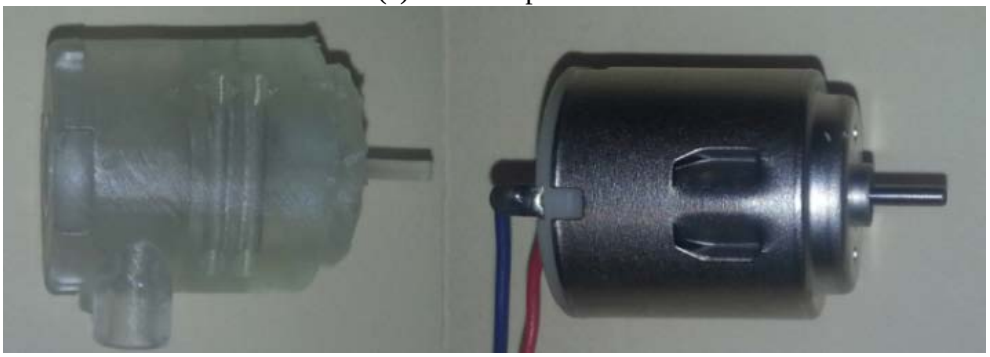

Figure 5.4 - (a) Assembled motor with fiber optics and pneumatics in place. Red light from the fibers is visible. (b) Exploded view of the miniature airmotor. (c) Side-by-side comparison of an highly magnetic electric motor (top) and a miniature airmotor encoder unit (bottom), demonstrating equivalent size.

robot, due to the choice of defining the RCM as falling in the XY plane. The height of the lower half of the hourglass shape is dependent on the length of the needle or other tool inserted through the guidance channels – the Fig. 5.2b depicts the workspace of a 100mm length needle.

Robot registration was performed using spherical fiducials embedded in the template support. This allowed a "floating" registration of the robot, providing accurate determination of the XY plane but not its precise location. Rulers on the side of the robot were used for an initial reading of position prior to scanning and combined with registration to estimate the robot's position. This estimate, coupled with a 5mm zone around the edges of the workspace into which the robot was prohibited from entering, ensured that the robot did not hit the rails. The estimated position was used only for this purpose; positioning and targeting were performed using relative coordinates from the registration, maintaining accuracy.

The control box for the robot was built around a NI USB-6009 DAQ card. The analog inputs on the card read the fiber optics signals while the digital lines toggled the solenoid valves used to control the motors. Fiber optic lines ran through the motors and encoded rotation.

Software Design

Control software was implemented in LabView. In the GUI, users are presented with an initial screen to perform MRI coordinate registration. Once completed, a control window allows the user to enter targeting coordinates and toggle targeting control between manual and automatic. This control program operates from a laptop independent from the MRI computers, requiring manual selection and entry of targeting points by

operators. This requires some extra time and effort by the operators, but allows the system to be operated in any imaging suite.

Control software was implemented in LabView. In the GUI, users are presented with an initial screen to perform MRI coordinate registration. Once completed, a control window allows the user to enter targeting coordinates and toggle targeting control between manual and automatic. This control program operates from a laptop independent from the MRI computers, requiring manual selection and entry of targeting points by operators. This requires some extra time and effort by the operators, but allows the system to be operated in any imaging suite.

All targeting calculations were based off of two points: the target point and a point through which the needle should pass to arrive at the target. The MRI coordinates of these points were converted to the robotics coordinate system and used to calculate the closest needle guidance channel to the desired angle and position the robot to align the

Table 5.2	**Variables used in targeting equations**
T	Target point in MR coordinates
P	Point on targeting path in MR coordinates
M	Transformation matrix from MR to robot coordinate system
T'	Target point in robot coordinates
P'	Point on targeting path in robot coordinates
v_t	Ideal targeting vector with components $\langle i, j, k \rangle$
θ_1, θ_2	Angular components of $\vec{v}_t$
θ_1', θ_2'	The angles used in the targeting template
v'_t	Actual targeting vector with components $\langle m, n, o \rangle$
G	Robot goal position for targeting
H	Distance from RCM to surface of targeting template
L	Length of needle to be inserted

selected channel with the target point. The targeting equations are based on a target point T, a point P along the desired path to the target, and the registration matrix M. First P and T must be converted to root target coordinates and the targeting vector vt determined.

$$P' = P \times M$$

$$T' = T \times M$$

$$P' - T' = \hat{v}_t = \langle \hat{\imath}, \hat{\jmath}, \hat{k} \rangle$$

A pair of angles θ1 and θ2 defined the angulation of vt relative to the z axis, and were rounded to the nearest multiple of 4 to comply with the template spacing to obtain template targeting angles θ1' and θ2'.

$$\theta_1 = \tan^{-1} \frac{\hat{\jmath}}{\hat{k}}$$

$$\theta_2 = \tan^{-1} \frac{\hat{\imath}}{\sqrt{\hat{\jmath}^2 + \hat{k}^2}}$$

$$\begin{bmatrix} \theta_1' \\ \theta_2' \end{bmatrix} = 4 * \text{round}(\frac{1}{4} \begin{bmatrix} \theta_1 \\ \theta_2 \end{bmatrix})$$

If either θ1' or θ2' is greater than 20˚, the targeting solution is invalid. If a targeting solution is valid, the robot goal position (Gx, Gy) and insertion depth (D) are calculated from T ' and a new targeting vector v't determined by θ1' and θ2'. H is the distance from the XY plane and RCM to the top of the targeting template.

$$\hat{v}_t' = \langle \hat{m}, \hat{n}, \hat{o} \rangle = \langle \cos\theta_1' * \sin\theta_2' , \sin\theta_1' , \cos\theta_1' * \cos\theta_2' \rangle$$

$$k = \frac{T_z'}{\hat{o}}$$

$$\begin{bmatrix} G_x \\ G_y \end{bmatrix} = \begin{bmatrix} T_x \\ T_y \end{bmatrix} - k * \begin{bmatrix} \hat{m} \\ \hat{n} \end{bmatrix}$$

$$L = \frac{H - T_z'}{\cos\theta_1' * \cos\theta_2'}$$

This method can be used due to the choice of placing the RCM in the XY plane. Once the target position was acquired, the software displayed the goal position for each

axis and the required angulation and needle depth. The robot could be moved to the target point either by operator control or via automatic positioning, which used a PD controller to modify the high pulse times of a PWM signal to the solenoid valves. The controller functioned similarly to the controller in Chapter 3, with an additional term reducing the high time based on increasing motor velocity.

Bench Tests

Methods

Bench tests of the robot's X/Y positioning capabilities were performed using a 0.5mm resolution grid mounted beneath the robot and aligned along the same X and Y axes. A diamond-tip rod was inserted through the central hole of the template (parallel the robot's Z axis) and positioned to float 1 millimeter above the grid. The tip of the rod was used to pick the robot's location on the test grid. The robot was moved into position and registered at the origin of the grid and progressed through a series of repositioning movements (n=40). The goal position was entered into the control software and the moved to the target point. The goal position, the robot's reported position, and its actual position were recorded for each movement.

Full positioning bench trials (n=25) were performed using an Aurora EM tracker. A target point was chosen blow the XY plane of the robotic coordinate system to ensure translational repositioning was necessary for each insertion angle. The full system test utilized a range of angles in the radial template up to $\pm 16^{\circ}$.

Results

Translational bench tests showed a small control error (difference between goal position and reported position). The control error mean was 0.02mm with a standard

deviation of 0.22mm. The targeting error (difference between goal and actual positions) was more significant, with a mean of 0.21mm and a standard deviation of 1.19mm (Fig. 5.4a). The full system targeting tests with the Aurora EM tracker yielded a mean targeting error of 0.43mm and a standard deviation of 0.48mm (Fig. 5.4b). An important note is that he tracker has a system accuracy of 0.7mm.

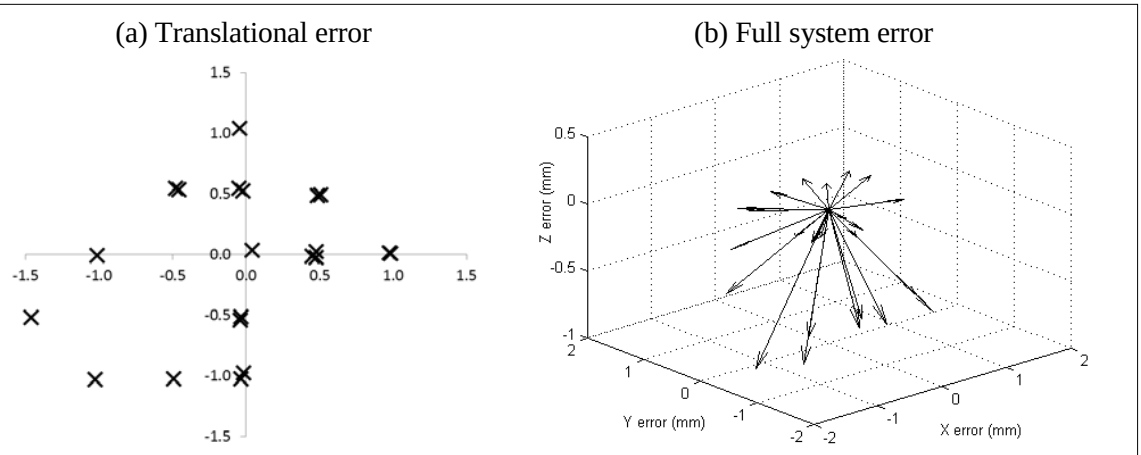

Figure 5.5 - Error visualization from bench tests a) XY translational error. b) Each vector represents the offset from the target point to the needle tip for one of the tested angulations.

Cadaver Trials

Method

Cadaver trials (n=3) were performed using 16-inch stillborn piglets, chosen for their economical price and small anatomy (Fig. 5.6). The cadavers were fixed inside a container with a cut-out lid and the robot attached to the container cover. The cadaver was imaged using the imaging sequence scan specified above which obtained the target anatomy as well as the robot fiducials. After registration of the fiducials, target planning for a point was performed. The robot was adjusted, and a brass needle inserted to the prescribed depth. A confirmation scan, adjusted to a smaller volume of interest to reduce time, was taken to determine the location of the needle tip. When the needle tip deflected off of the vertebrae, the robot was adjusted and an alternate needle guide was used. Once

the needle tip was inside the vertebrae, the target point, needle tip coordinates, and a point on the needle were recorded in order to calculate transverse and insertion errors.

Results

Cadaver trials demonstrated a mean accuracy of 2.84mm for successful insertions. Successful insertion into the spine is shown in Fig. 5.7. The procedure steps and procedure time are listed in Table 5.3, showing an efficient workflow for MRI-guided spinal interventions.

The Repetition phase requires less time than the initial sweep through Planning, Positioning, and Confirmation phases due to the ability of the operators to plan the subsequent insertion during the confirmation scans. Based on the trials performed for this study, it is estimated that with a 60 minute baseline to perform the first insertion and with 10 minutes per additional insertion, a surgical team could perform 6 MRI-guided spinal insertions in a 2 hour procedure, which includes time to clean the imaging suite.

Table 5.3	**Workflow**	
Phase	Description	Duration
Setup	Moving subject and robot into scanner and preparing control hardware	25 min.
Initial Scans	Localizing scans and high-resolution volumetric images of target anatomy	20 min.
Planning	Choice of target and needle path points by operator	5 min.
Positioning	Relocation of the needle guide to the target point	3 min.
Confirmation	Confirmation scan to verify final tip position	7 min.
Repetition	Repeating Planning, Positioning, and Confirmation for additional insertions	10 min.
Breakdown	Removal of equipment and subject from scanner and control rooms	20 min.

(a) Robot & coil

(b) System view from control room

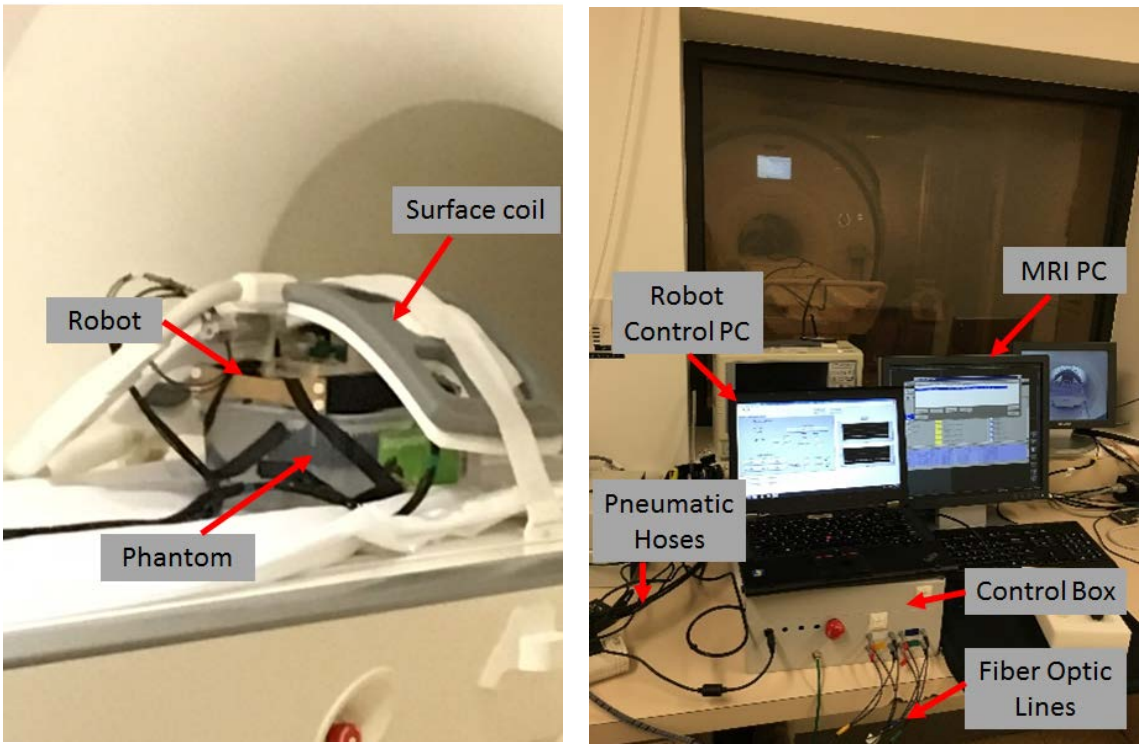

Figure 5.6- (a) The setup on the MRI table prior to an experiment. The robot is positioned on top of the phantom or subject, after which a body coil is strapped across the supporting bars of the robot. (b) View of the complete system from the MR control room.

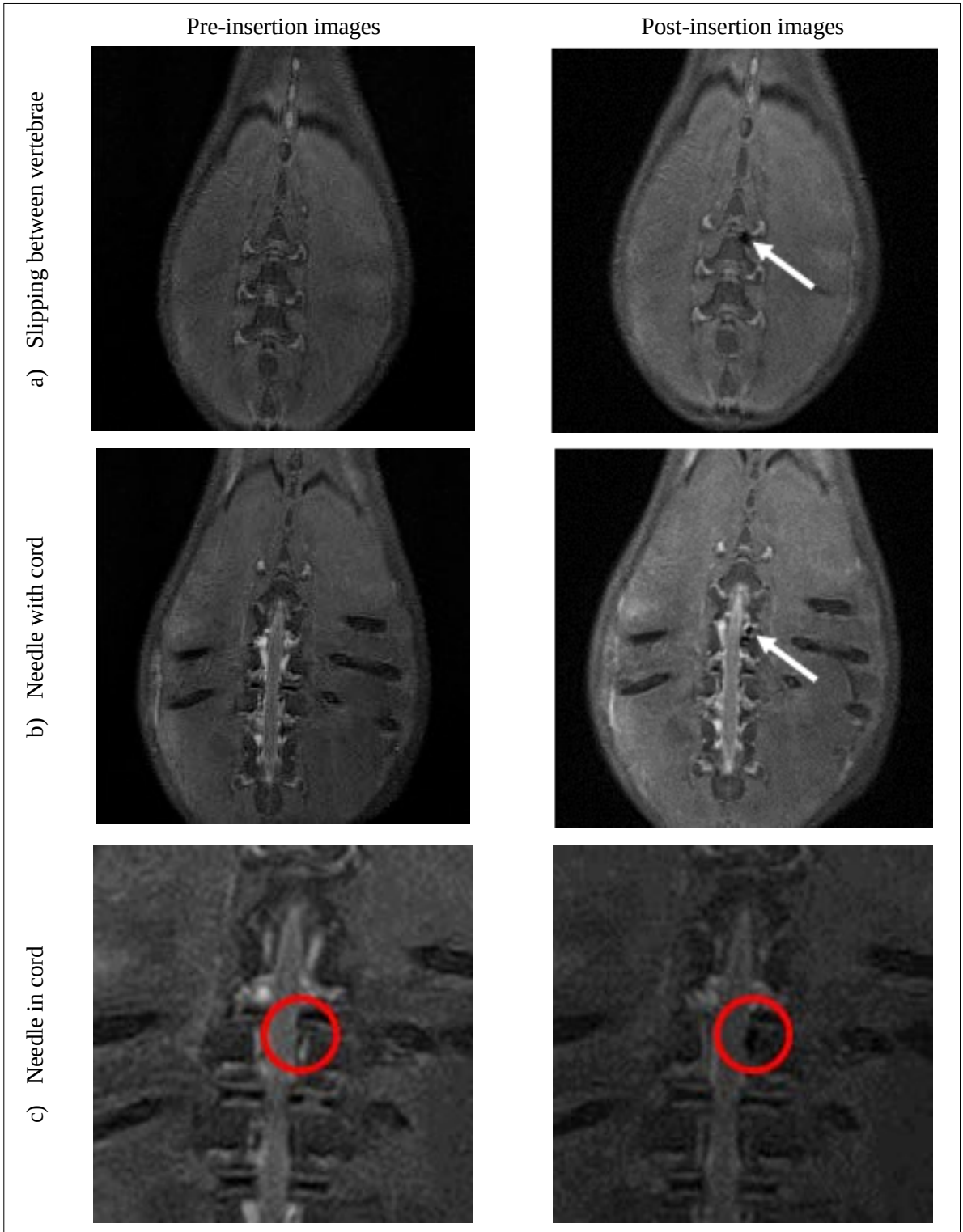

Figure 5.7 - Matching images of a swine trial (a) pre-insertion and (b) post-insertion. From left to right: 1) A coronal view of vertebrae superior to the spinal cord, showing the needle passing between vertebrae. 2) A section of the spinal cord, with the needle at the edge of the cord. 3) A second swine trial where the needle punctured the lamina and the tip rested inside the cord.

Discussion

Currently, direct injection into this target area requires open surgery, so large studies with human subjects are not feasible. Our system has the potential to allow for large-scale research into what small animal models have shown to be a very promising treatment for ALS, a fatal disease with no cure. SpinoBot provides a minimally invasive method of directly injecting cellular therapeutics into the spinal cord. Using MRI-guidance, the robotic system helps accurately target the ventral horn of the spinal cord for percutaneous injection of stem cells. The design requirements put in place by neurosurgical advisors and the degree of accuracy attained (0.48mm on benchtop, 2.84mm in cadavers) highlight a system that can be effectively used for MRI-guided interventions. The workflow developed over the course of experimentation with the system resulted in a time-efficient process, enabling several MRI-guided and MRI-verified insertions in a 2 hour session in the MR suite. During cadaver trials, a regular occurrence resistance to insertion once the needle was past the skin, which is to be expected when puncturing the spinal cord lamina, but may have also been present when making contact with vertebrae.

With a person or small group each dedicated to setting up the subject, robot, and control hardware, initial setup time should reduce. As the entire system was installed and removed from the MR suite for each trial, a more permanent housing in the suite should also reduce setup and breakdown times. Interventional radiologists on a surgical time would most likely be able to develop more finely tuned imaging sequences for their needs, reducing scan times.

The use of a template which can easily be removed from the robot allows numerous future possibilities for improving the design. Development of a continuous angulation end effector, as discussed in the following chapter, could reduce error as it would permit any angulation within its limits without needing to be coerced to a nearby angle, assisting in reducing error caused by the need to modify the desired angle slightly to conform to the template. Collaborators at Emory have also used a continuous-motion manual guide which pivots about a large ball joint – a socket for the ball would be a simple insert for such a guidance channel if this avenue is pursued in the future.

Limitations

Improvement of the radial template is possible using precise milling techniques or molded templates to reduce the clearance between the needle and guidance holes, because the clearance can cause error. The 3d-printed template used in these trials forces a compromise between a looser fit around the needle causing greater error, and a tighter fit which causes noticeable resistance to insertion due to the ridges inherent to FDM printers.

Although the patient is imaged in the MRI bore, the insertion takes place outside of the bore. When multiple insertions are necessary, the patient must be wheeled in and out of the bore, increasing procedure time and causing patient movement which can cause registration error and affect the positioning of the patient's anatomy relative to the template. A motorized insertion axis could therefore reduce both procedure time and registration error, especially for procedures involving multiple insertions. Coupled with the addition of two axes of rotation stages in place of the current rotational template grid,

this would maximize the number of available needle paths and reduce procedure time drastically, eliminating the need for patient removal from the bore.

References

[1] A. Squires, J. Oshinski, J. Lamanna, and Z. T. H. Tse, "SpinoTemplate: A Platform for MRI-Guided Spinal Cord Injections," *Journal of Medical Robotics Research,* vol. 1, p. 1640006, 2016.

[2] Jason Lamanna, Lindsey Urquia, Carl Hurtig, Juanmarco Gutierrez, Cody Anderson, Pete Piferi, *et al.*, "Minimally Invasive Magnetic Resonance Imaging-Guided Delivery of Neural Stem Cells Into the Porcine Spinal Cord," presented at the International society of Magnetic Resonance in Medicine, Toronto.

[3] A. Squires, S. Xu, R. Seifabadi, Y. Chen, H. Agarwal, M. Bernardo, *et al.*, "Robot for Magnetic Resonance Imaging Guided Focal Prostate Laser Ablation," *Journal of Medical Devices,* vol. 10, p. 030942, 2016.

[4] Z. Tse, H. Elhawary, A. Zivanovic, and M. Lamperth, "A one degree of freedom MR compatible haptic system for tissue palpation," in *Proceedings of the 13th Annual Meeting of the British Chapter of the International Society for Magnetic Resonance in Medicine*, 2007.

CHAPTER 6

REFINEMENT OF A ROBOT FOR SPINE INTERVENTIONS

Progressing to Motorized Actuation

Actuating Rotation

The discrete angulation of the radial template, while presenting a compact solution for multiple targeting angles, creates a limitation in the system's ability to reach a target point. While in some cases the constraint of targeting angles to the template is sufficient for targeting requirements there are cases, particularly in smaller subjects, where the difference of a couple degrees determines whether a needle slips between vertebrae or deflects off bone. Development of a fully actuated, two degree-of-freedom end effector for needle guidance provides continuous coverage of targeting angles and provides sub-degree angulation adjustments.

The design of the radial template used in the first iteration of the spine robot intentionally provided the ability to replace it with an actuated insert without affecting the motion or accuracy of the XY stage. With the location for the rotation stage in place, the primary design hurdle was fitting a pair of motor and gearbox combinations in the space available (Fig. 6.2). Numerous initial designs were developed in Solidworks, but none were chosen to be fabricated due to convoluted arrangements of components in order to maintain independent rotation axes. Rotation of fibers optics and pneumatic hoses also presented issues.

The ultimate solution to volume constraints was inspired by the CoreXY system used in the prostate robot. The developed rotation stage uses a pair of fixed motors to attain rotation in two angles, with head-to-foot rotation (θ) covering ±35˚ and left-to-right rotation (φ) covering ±30˚. The design is similar in some regards to an automotive differential with the input and output shafts reversed. The floating frame of the rotation stage pivots on the large hub of the input gears, while the needle guide rotates within the floating frame on an axis perpendicular to the rotation axis of the floating frame.

The pneumatic motors were again modified during the last stages of development (Fig. 6.3). The final design reduces the air gap between fibers to 1.5mm, as opposed to between 7 and 10 mm in older designs, ensuring less loss of light intensity. This comes at the cost of a larger motor housing; while the output/front half of the motor body maintains the same dimensions as a RC-260 DC motor to ensure proper fit with the gearboxes, the rear half has an increased diameter to allow the optical fibers to run parallel to the motor shaft. A thin disc connecting the vanes of the rotor interrupts the fibers, creating a quadrature signal during rotation. The reduced air gap maintains a stable TTL output from the fiber receivers, which would occasionally drop out in the previous versions of the motor. Eight possible fiber paths allowed fibers to be installed in locations most advantageous in permitting full range of motion.

The control of two rotational axes via a pair of linked input motors occurs due to the symmetry of the gear system about the miter gear attached to the needle guide. The rotation of a one input while the other remains fixed causes rotation of both the floating frame and the needle guide; action by both motors allows control of rotation about both axes (Fig. 6.1). Rotation of the inputs in the same direction causes opposing forces to be

applied to the gear attached to the needle guide, negating its rotation, with the resulting forces applying rotation to the floating frame. If the inputs are rotated in opposite directions, forces act cooperatively to rotate the needle guide, and no action is applied to the floating guide. With miter gears joined directly to the input shafts and the needle guide, the following simple equations define rotations in the θ and φ directions using input motor rotations R_1 and R_2, reduced through a gear ratio of G_r:

$$d\theta = \frac{dR_1 + dR_2}{2G_r}$$

$$d\varphi = \frac{dR_1 - dR_2}{2G_r}$$

Targeting Options

With the addition of the actuated rotation stage, targeting calculations were simplified relative to the previous version of the SpinoBot which utilized the radial template. With continuous rotation, the angle specified by the target and path points could be met exactly, eliminating all calculations necessary to snap the targeting vector to the template's needle channels and the subsequent update to the XY position.

While the calculation of targeting angles based on the two points selected by the operator remains the default method of angle selection, a second targeting option in the form of operator-defined angles was added at the request of end users. The selection of a path point is replaced by the explicit definition of θ and φ by the operator. A removable manual protractor to assist in this process was added to the floating stage, which could be used to define θ and φ even without registration.

(a) Ideal Rotation Stage

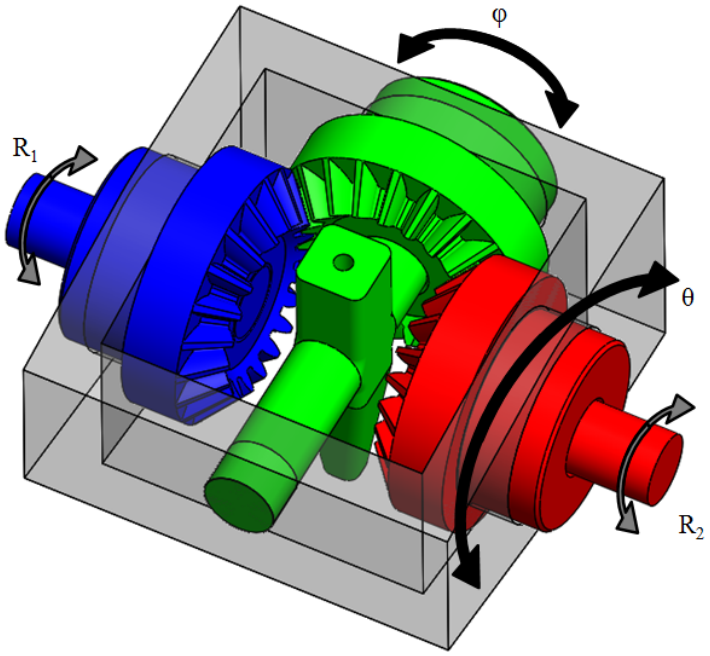

(b) Actual Rotation Stage

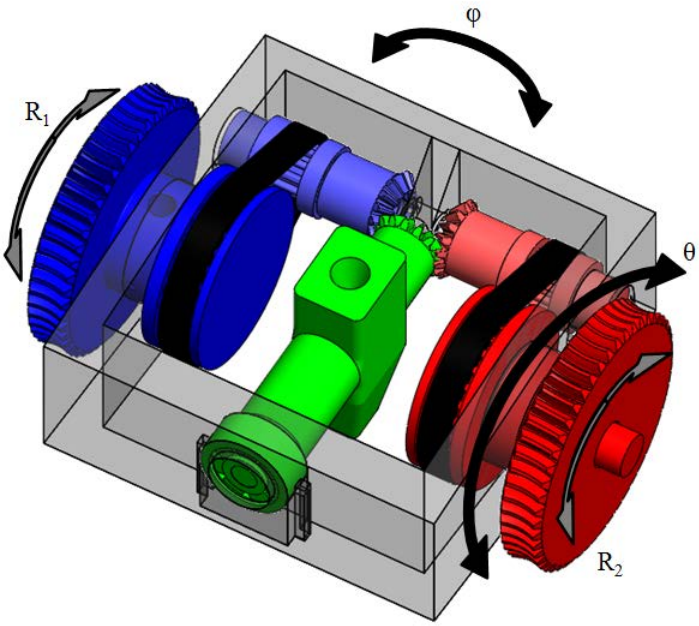

Figure 6.1 – Presentation of the fixed motor rotation stage. (a) The ideal configuration involves two input shafts driving a configuration of three miter gears. Rotation in the θ direction occurs when R1 and R2 rotate in the same direction, while rotation in the φ direction occurs when they rotate in opposing directions. (b) The actual design obeys the same relations, but utilized a timing belt in addition to miter gears to allow greater rotation of the needle guide.

The realized system could not match this ideal scenario as appropriately sized miter or bevel gears could not be sourced to fit within the limited volume of the floating frame while maintaining the required angulation capabilities. Instead, timing belts were used in addition to smaller miter gears between the inputs and the needle guide, adding an additional factor G_b to the calculation of φ:

$$d\varphi = \frac{dR_1 - dR_2}{2G_r G_b}$$

Registration

The implementation of a continuous end effector for rotation necessitated the addition of angulation calculation to robot registration as targeting angles were no longer inherently registered with the XY system, as occurred using the radial template. Angulation calculation was accomplished by selecting two points within the guidance channel of the needle guide. Made of plastic, the guide itself is invisible in MR images. Visualization of the needle guide is made possible by empty space in the form of a cylindrical shell surrounding the guidance channel. This space was filled with fluid extracted from the same fiducial markers used for registration to ensure visibility, as minor experimentation with developing our own contrast agent were not successful. The locations of the fiducials for coordinate registration were moved to between the subject and the needle guide to ensure their visibility in any imaging sequence which captured both the needle guide and the subject.

(a) Fully assembled SpinoBot

(b) Actuated 2-DOF rotation stage

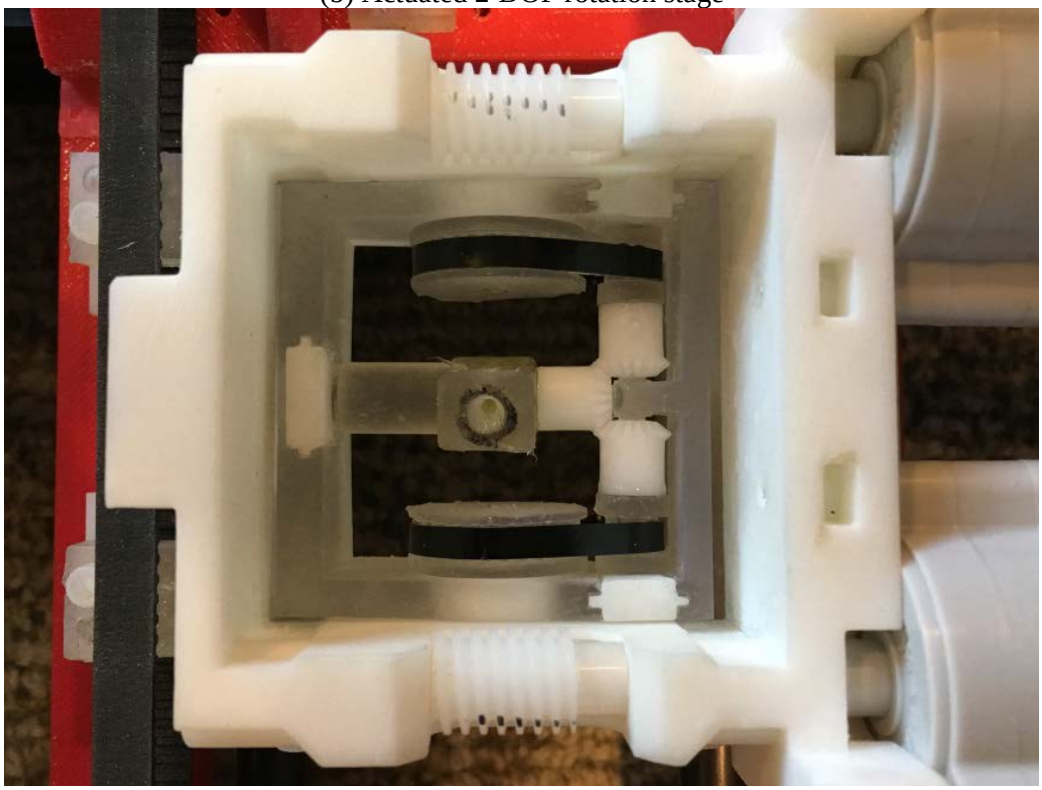

Figure 6.2 – (a) Image of the assembled SpinoBot in its final design. (b) Close-up of the actatuated rotation stage. The outer dimensions of the translucent floating frame measure 48x47mm.

(a) Motor components (b) Alignment of rotor and fibers for quadrature

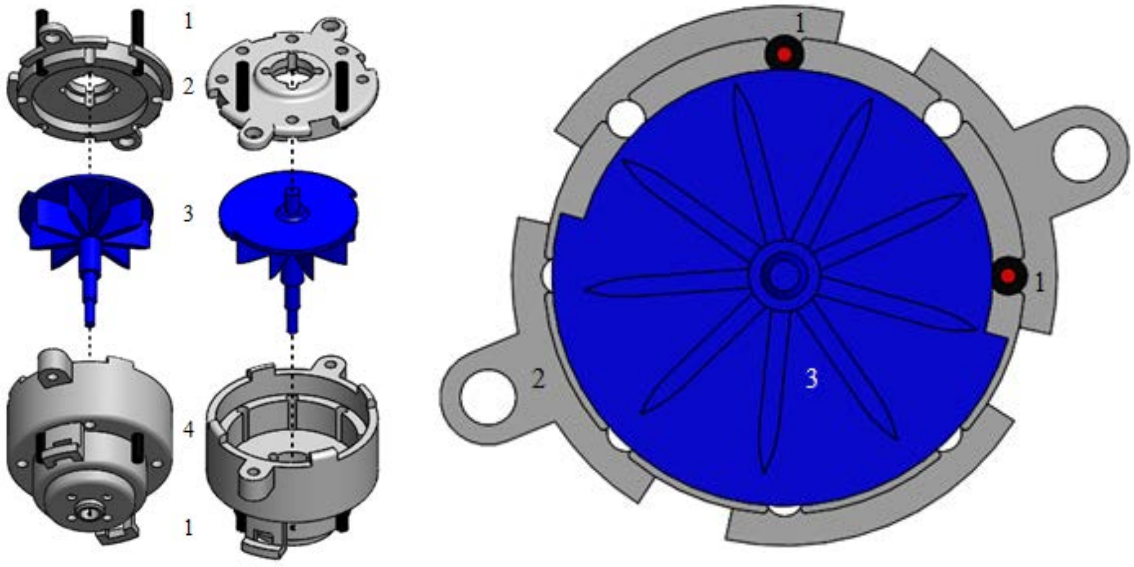

Figure 6.3 - (a) Motor components including 1) fiber optic cables, 2) motor cap, 3) rotor, and 4) motor body. (b) The rotation of the rotor interrupts the optical signal over half of a rotation. Offsetting the pair cables by 90˚ thus gives the quadrature signal.

System Calibration for Submillimeter Accuracy

Testing of the several devices presented in this dissertation always presented small amounts of error caused by deviation of the real world from idealized gear trains and belt systems. Gear backlash and fractionally mistightened timing belts create a situation wherein a motor, upon reversing, effectively jumps ahead of the end effector as motion is lost as the gear train and belts reverse into the backlash behind the previous direction of actuation.

This issue was compensated for by establishing a buffer on each axis which accounted for the backlash upon reversing direction (Fig. 6.4). The input dC_{in} to each buffer was the count from the quadrature encoder on a motor, while the output dC_{out} was a modified count which was used by to update the robot position. The buffer value from the previous loop was updated by the motor quadrature count in the current loop.

$$B_{n+1} = B_n + dC_{in}$$

If the resulting value of Bn+1 is greater than Bmax or less than 0, an output value dCout is calculated; if Bn+1 falls between 0 and Bmax, dCout is 0. The value of Bmax was determined empirically by tracking the lost distance or angle with the Aurora EM tracker and converting the result to a quadrature count.

$$if\ B_{n+1} > B_{max}:\ \ dC_{out} = B_{n+1} - B_{max}$$

$$elseif\ B_{n+1} < 0:\ \ dC_{out} = B_{n+1}$$

$$else:\ \ dC_{out} = 0$$

The final step is to coerce the buffer value to within the range of [0, Bmax] before passing it to the next loop.

$$B_{n+1} = \max(0, \min(B_{n+1}, B_{max}))$$

(a) Buffer increasing without exceeding buffer maximum

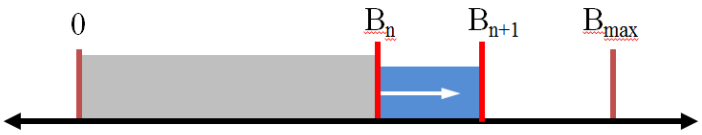

(b) Buffer passes maximum

(c) Buffer at maximum

Figure 6.4 – Example of the count buffering system. In situation (a), the B_{n+1} falls between 0 and B_{max}, so no count is passed to distance calculations. In (b), B_{n+1} exceed B_{max} and the difference is passed on to B_{max}. Once the buffer limit has been reached, the entirety of the count passes through, shown in (c).

Comparison of translation positioning accuracy pre- and post-buffer is shown in Fig. 6.5. The reported and actual positions were recorded, with the mean plotted on the horizontal axis and the difference on the vertical axis. Prior to implementation of the buffer, large and consistent errors are clearly visible when an axis reverses direction. Two smaller errors are visible for reversal on the X axis, but analysis of the data revealed that these points were subsequent test points, during which the end effector did not move during the first data point. Summation of the two points placed the result in the same range as the other X axis reversal errors, further contributing to evidence of systemic error during reversals. Implementation of the buffer removed the systemic error, and a two-sample t-test rejected the null hypothesis that reversal and unidirectional actuation were statistically different ($p=0.61$), confirming this belief.

Determining proper buffering values for the rotation axes proved more difficult due to the interdependent nature of the angulation components. Data was collected for angulation, recording target θ and φ, actual θ and φ, and most recent motor direction (CW and CCW). Initial results suggested that there was no error on the θ axis resulting from reversal of motor direction or needle guide direction (Fig. 6.6). This was supported by a t-test which failed to confirm a difference due to either form of reversal ($p=0.33$, $p=0.37$).

There was clear evidence for significant error in the φ axis (Fig. 6.7). After analysis of the data, a buffer value was selected which applied only to φ calculations, leaving θ calculations independent. Application of this method resulted in errors shown in Figure 6.8. Initial analysis suggested no difference between continuation and reversal, confirmed by a final t-test which strongly implied no influence by motor reversal ($p=0.67$), and also implied little influence due to needle guide reversal ($p=0.17$).

a) Translational error without buffering

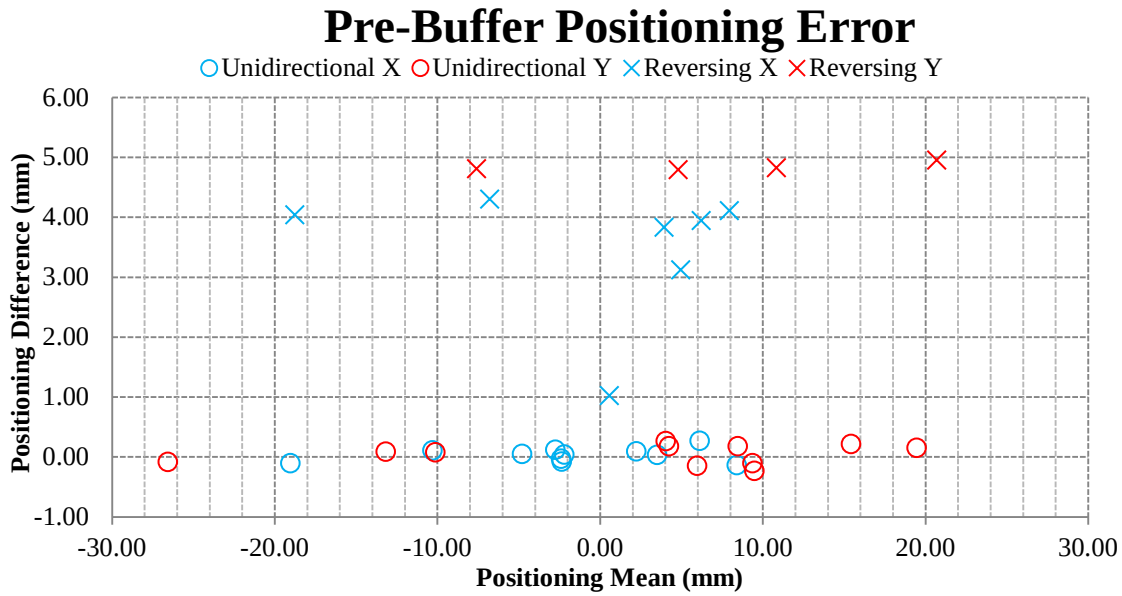

b) Translational error with buffering

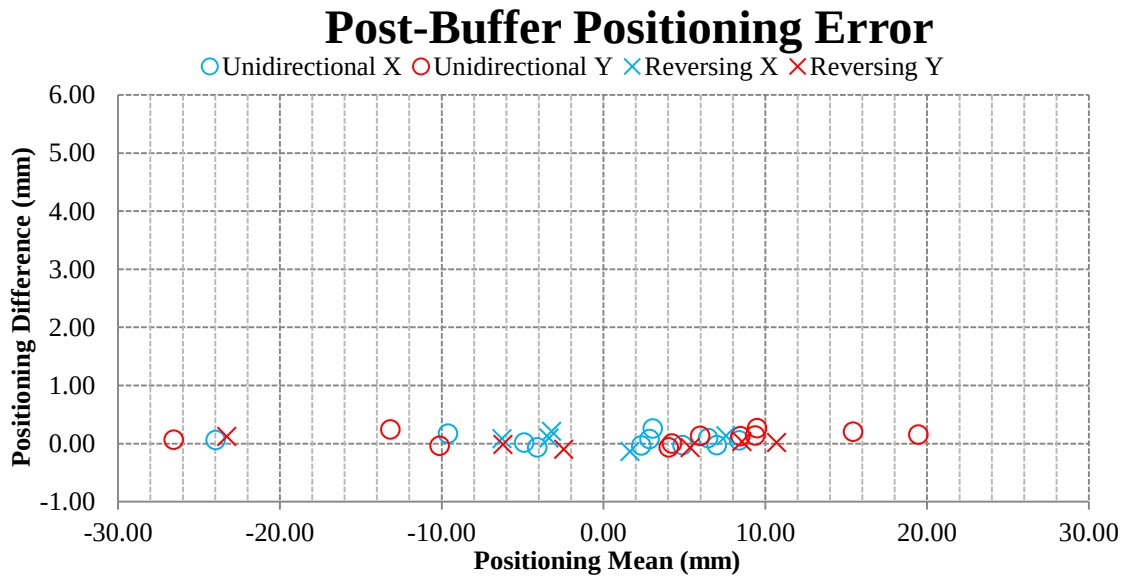

Figure 6.5 – Plots of translational error before and after implementation of reversal buffering.

a) Theta axis error relative to motor direction

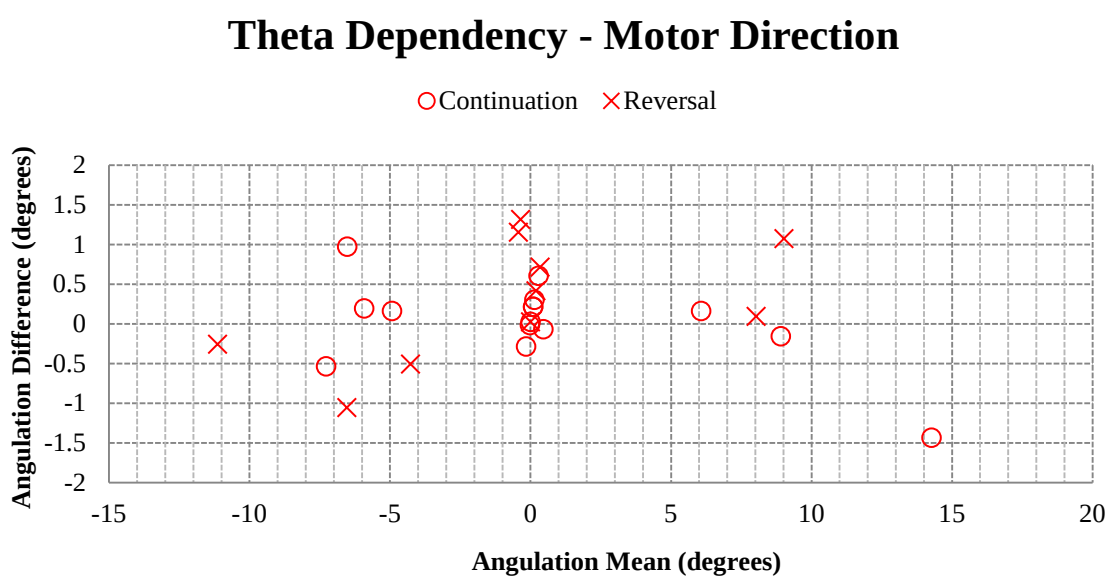

b) Theta axis error relative to needle guide angulation

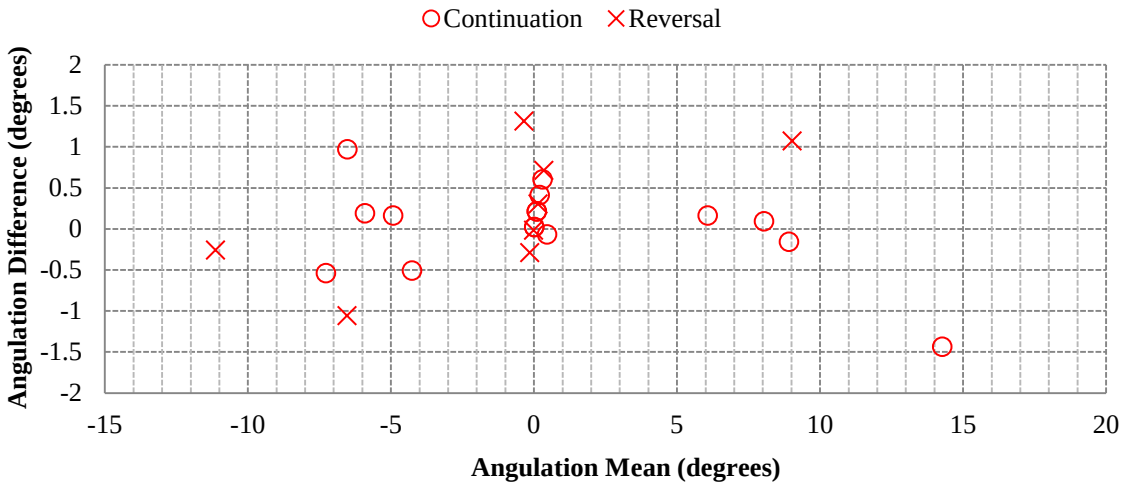

Figure 6.6 – Plots of θ error. No significant difference was found between continuing and reversing direction, relative to both motors and the needle angulation guide.

a) Phi axis error relative to motor direction

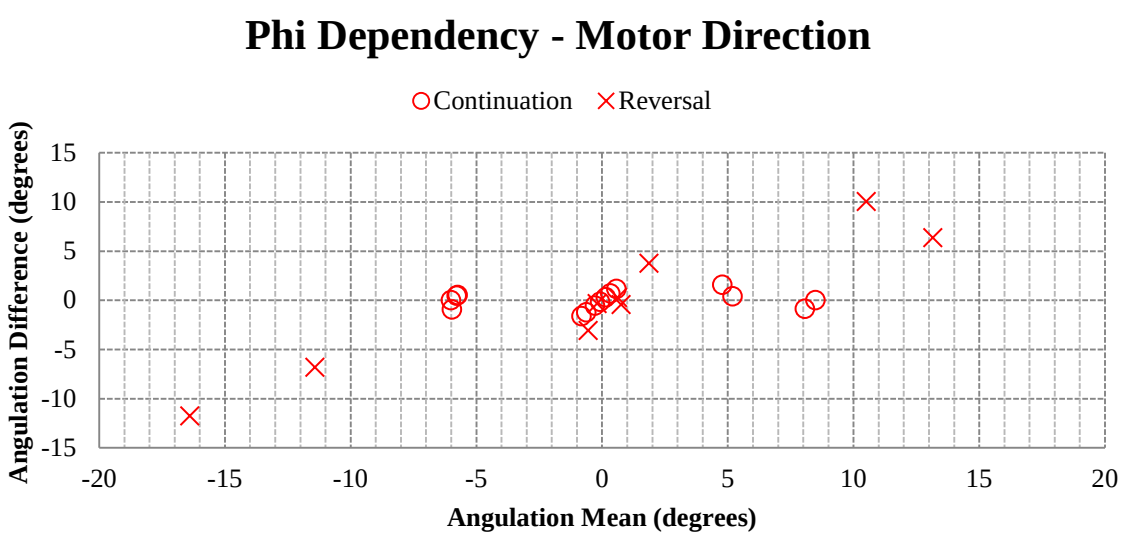

b) Phi axis error relative to needle guide angulation

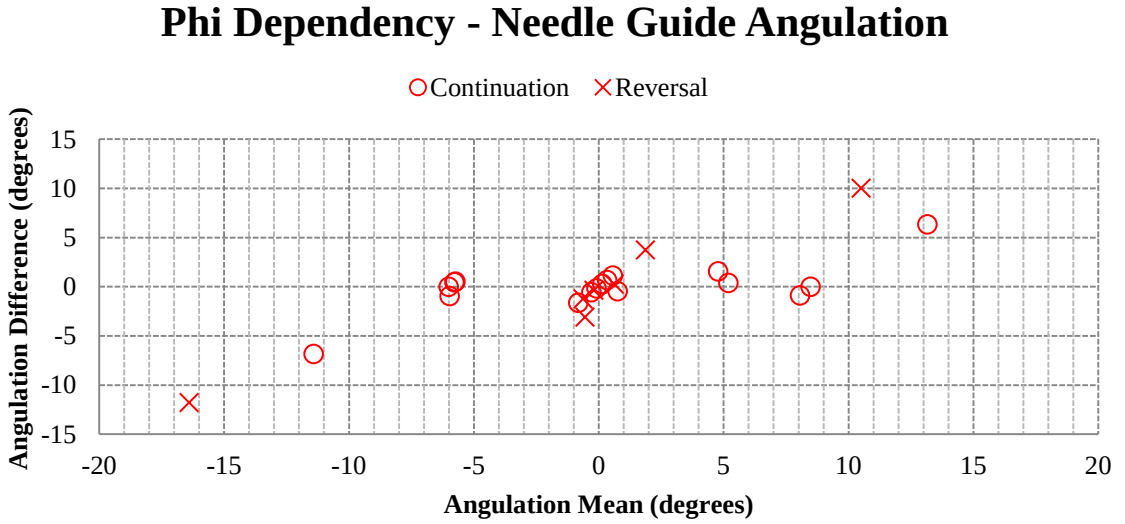

Figure 6.7 – Plots of systemic φ error prior to implementation of buffering.

a) Phi axis error relative to motor direction

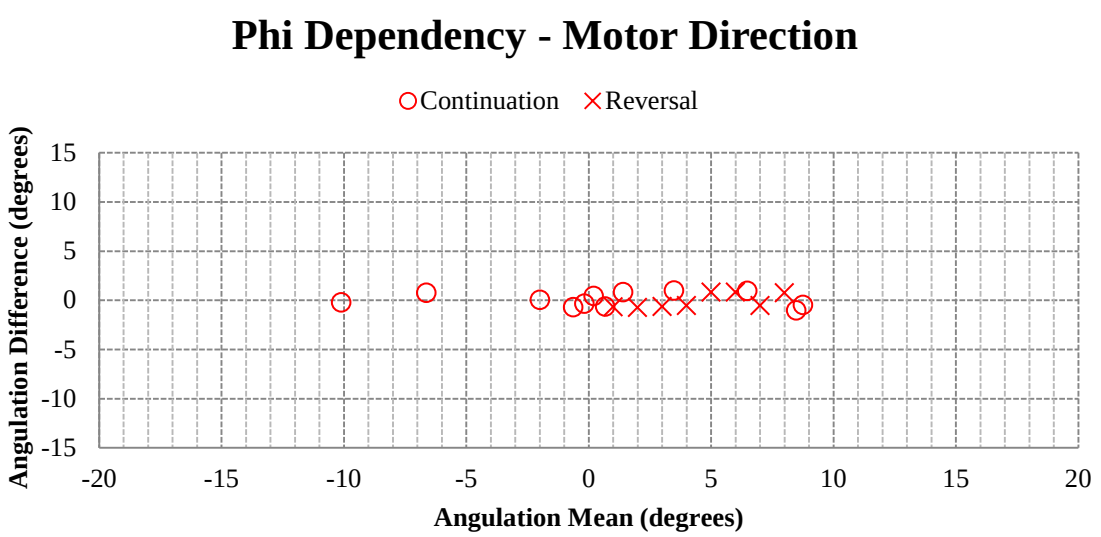

b) Phi axis error relative to needle guide angulation

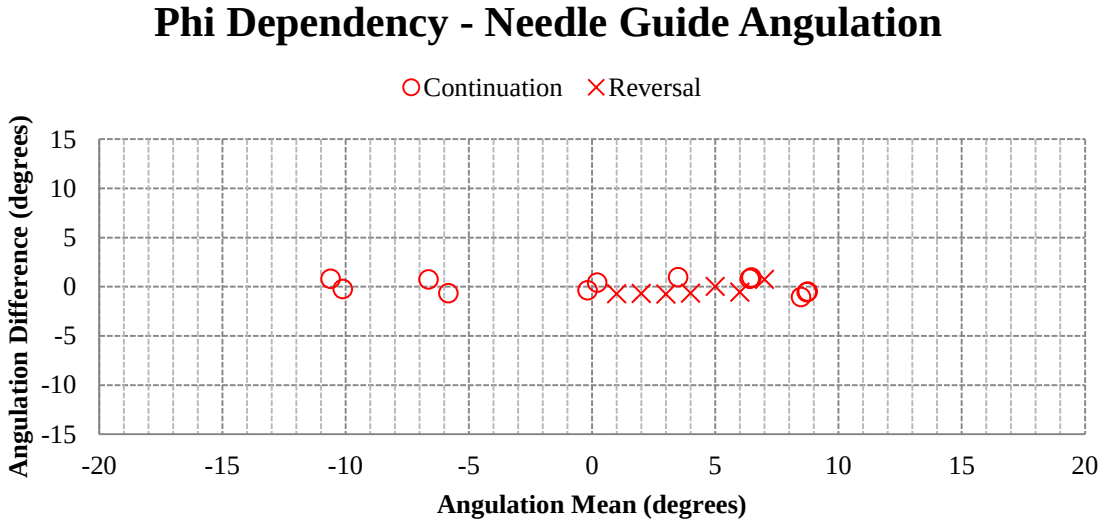

Figure 6.8 – With the use of the buffering system, error on the φ axis is decoupled from reversal of both motor direction and needle guide angulation.

Bench Testing

Method

Bench testing was performed using the Aurora EM tracker to validate the targeting accuracy of the 4 degree-of-freedom system. The first trials maintained a fixed orientation of the rotation stage in order to test the XY stage accuracy after the inclusion of the buffering system. Targets were determined at random between 10 and 30mm of the current position on each axis; the initial position, final position, and goal position were recorded for each step (n=30).

Following the validation of the XY stage, the rotation stage was tested to confirm rotation accuracy. Again using the EM tracker, Euler angles were obtained as the needle guide was rotated and compared to the reported position (n=40). Finally, total system tests were performed, combining both translation and rotation for full system tests. A target point was selected using the EM tracker, and the robot positioned according to registration and targeting calculations. The tracked wand was then inserted to the prescribed depth, just as a needle.

Results

The addition of the buffering system caused an improvement in the positioning of the XY stage. Earlier trials had a small mean error with a larger standard deviation, most likely stemming from the loss of position during motor reversal. The error mean remained low after the inclusion of the positioning buffer (μ=0.04mm), and the standard deviation reduced to σ=0.09mm. Measurement resolution was 0.7mm.

Rotation accuracy performed with an error mean of 0.6˚ and a standard deviation of 0.3˚ in full system accuracy trials. Full system bench tests returned a positioning error within acceptable levels (μ=1.12mm, σ=0.97mm).

MRI Trials

Phantom Trials

Testing of the full system in the MR suite (Fig. 6.9, 6.10) was first performed using a human spine phantom at Emory University Hospital (3T Siemens Magnetom Trio). The human spine phantom had an impermeable spinal cord, rendering intra-cord targeting impossible and not giving much value to quantitative error calculation. However, SpinoBot successfully guided insertions (n=4) between vertebrae to make contact with the surface of the spinal cord, indicating that the 4 degree-of-freedom system was able to adequately perform targeting.

Ex-vivo Trials: Methods

A 35lb wine cadaver was used to perform ex-vivo trials in Emory University Hospital (Fig. 6.11). The cadaver was secured inside a plastic container and SpinoBot attached above the cervical spine. After covering the exposed portions of the cadaver, a body coil was placed over the supporting bars of the robot. After localizing the subject, an image containing anatomy and the registration fiducial markers was obtained. Two target points were selected, each at a separate gap between vertebrae. Needle insertion was calculated for two angles for each target point. After aligning the needle guide for each insertion, a small incision was made using a MR-safe scalpel where the needle made contact with the skin, after which the needle was inserted to the prescribed depth. A

confirmation scan visualized the needle after each insertion. Gadolinium was injected into the spine after the first insertion to visualize the affected space.

Ex-vivo Trials: Results

All needle insertions proved successful. While not a quantified result, the insertions were described as substantially easier to perform relative to all other trials with the other various spinal insertion assistive devices developed as part of this dissertation. The concentration of gadolinium used for visualization was too high, ultimately not providing results. However, needle visualization provided exceptional results, fully puncturing the spinal cord multiple times (Fig. 6.12).

(a) Robot mounted on phantom

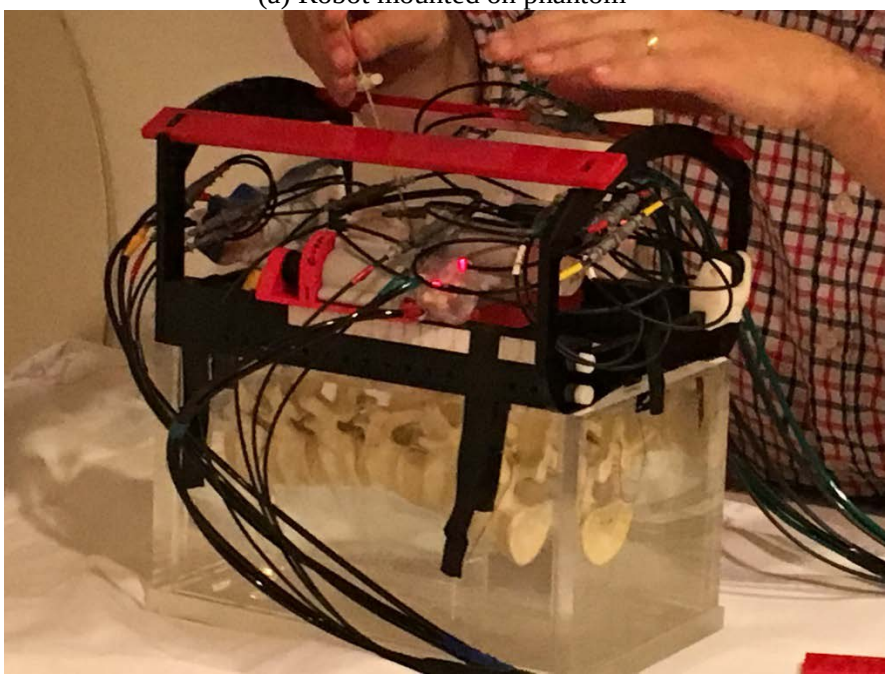

(b) Testing setup, outside bore

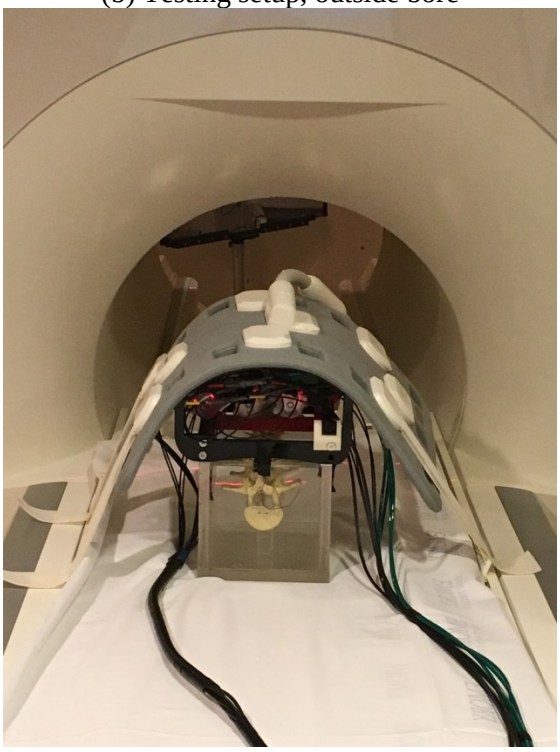

(c) Testing setup, inside bore

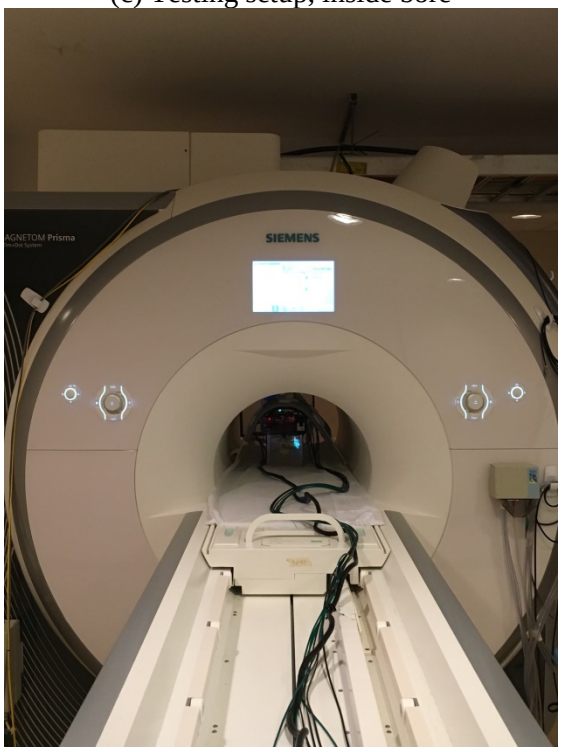

Figure 6.9 – MRI testing. (a) Preparing to insert a needle trough the guidance channel. (b) SpinoBot, phantom, and body coil outside bore. (c) All components inside bore, demonstrating successful development of a sufficiently low profile.

(a) 4-DOF Spinobot fully prepared for trials

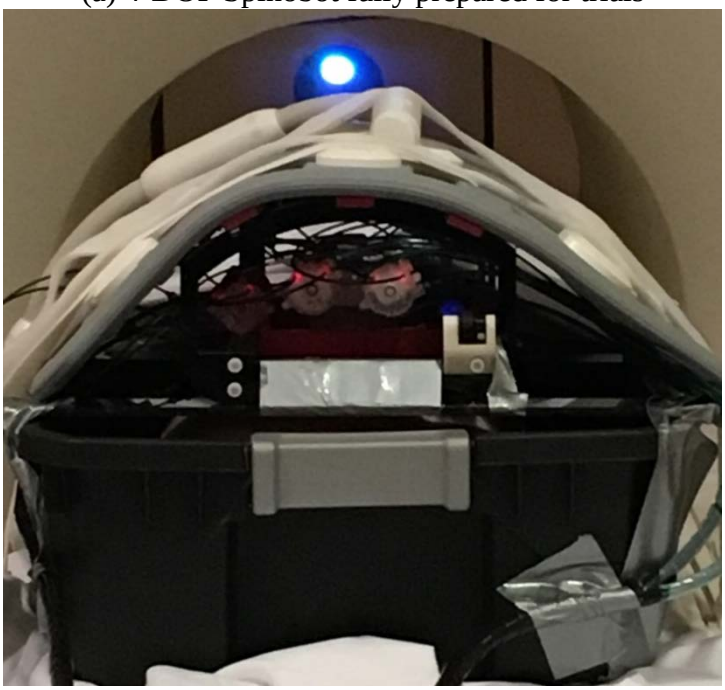

(b) Position of swine and Spinobot

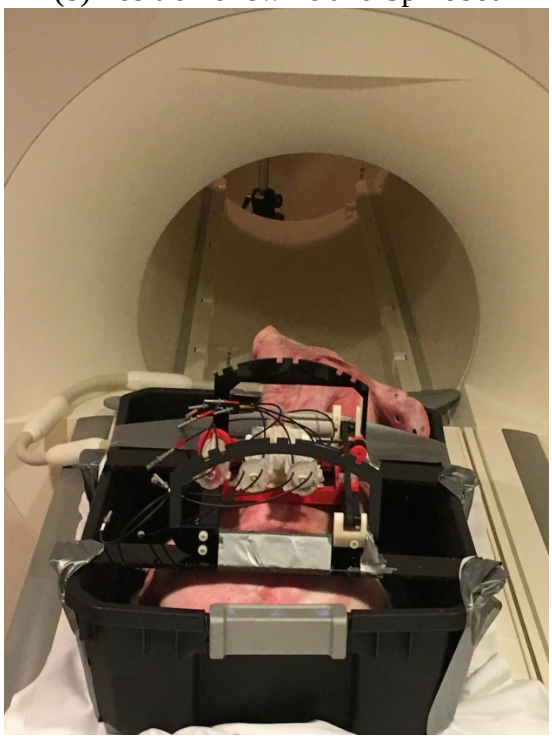

(c) Injecting gadolinium

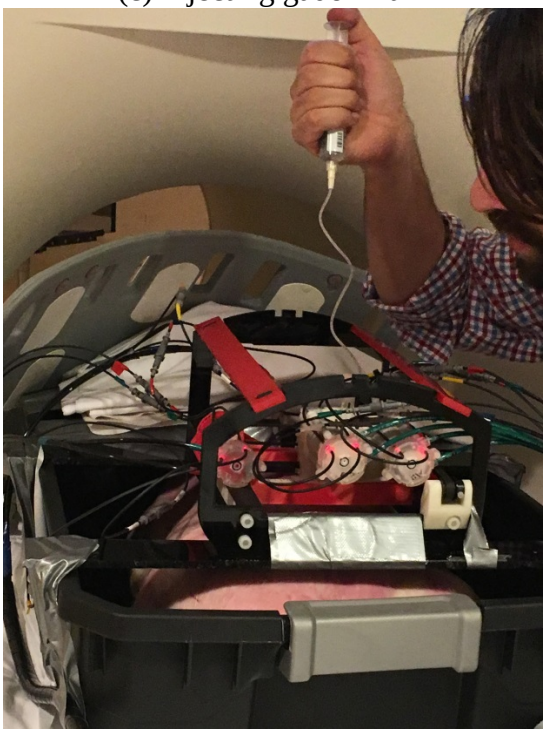

Figure 6.10 – Images of the ex-vivo trials. (a) Full system and subject, prepared for scanning. (b) Without the coil, attachment method is visible. (c) After insertion of a solid needle, a hollow needle is inserted along the same path and used to inject gadolinium.

(a) Picture of needle insertion

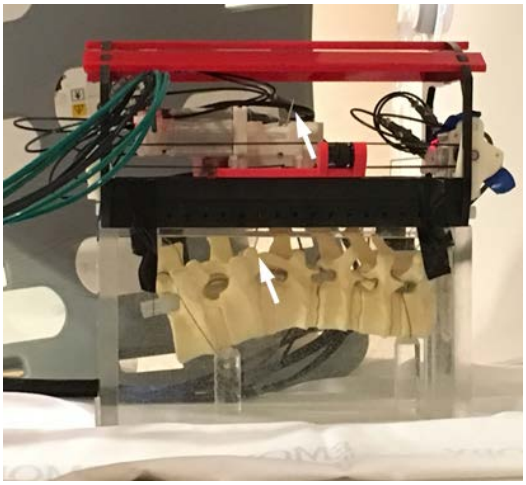

(b) Repositioned registration markers

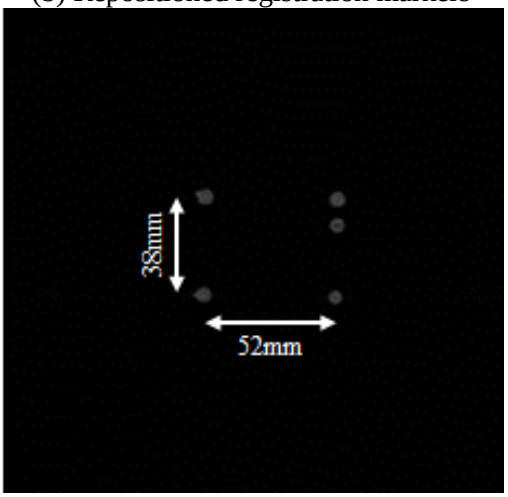

(c) Targeting channel of needle guide

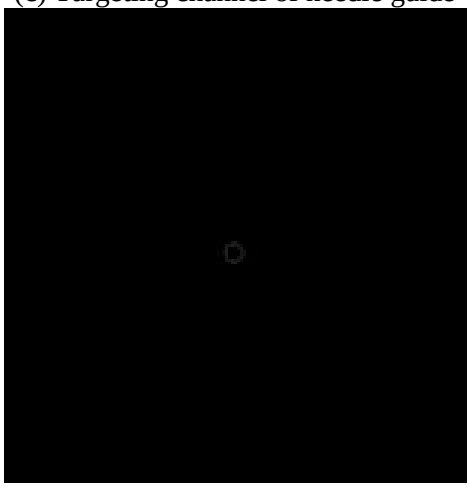

(d) Needle above spine

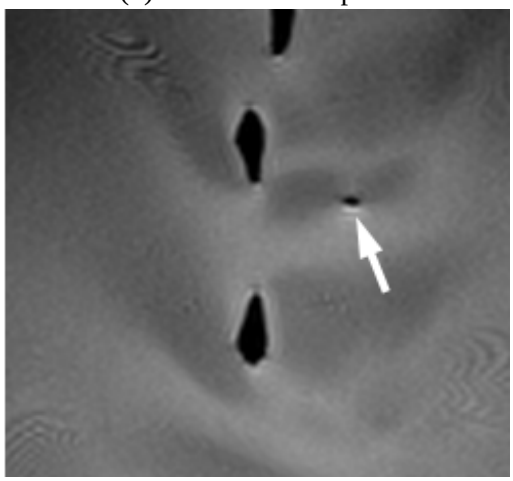

(e) Needle passing between vertebrae

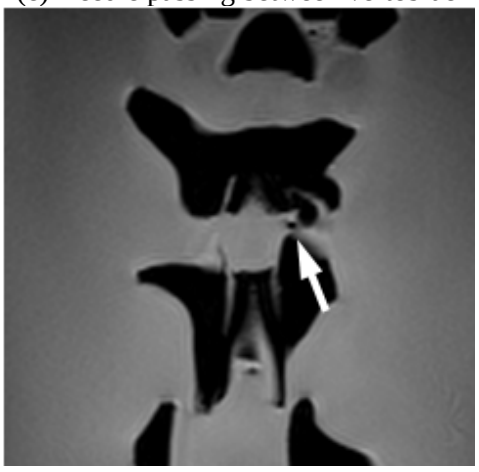

(f) Needle tip rests on phantom cord

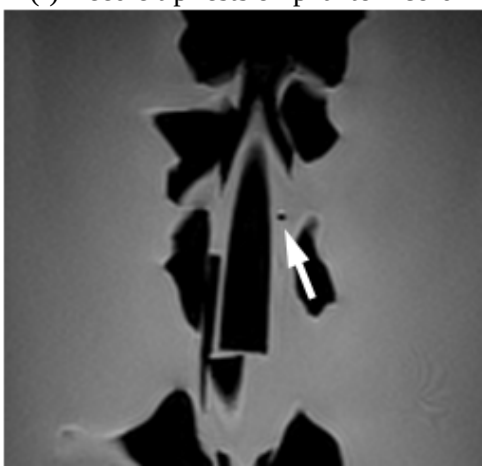

Figure 6.11 – (a) Picture of needle inserted through SpinoBot. It is visible above and below the frame. (b) Condensed fiducial markers just above the phantom. (c) Ring of fiducial fluid in the needle guide. (d) Needle trajectory above vertebrae. (e) Needle slipping the gap between vertebrae. (f) Needle making contact with impermeable spinal cord phantom.

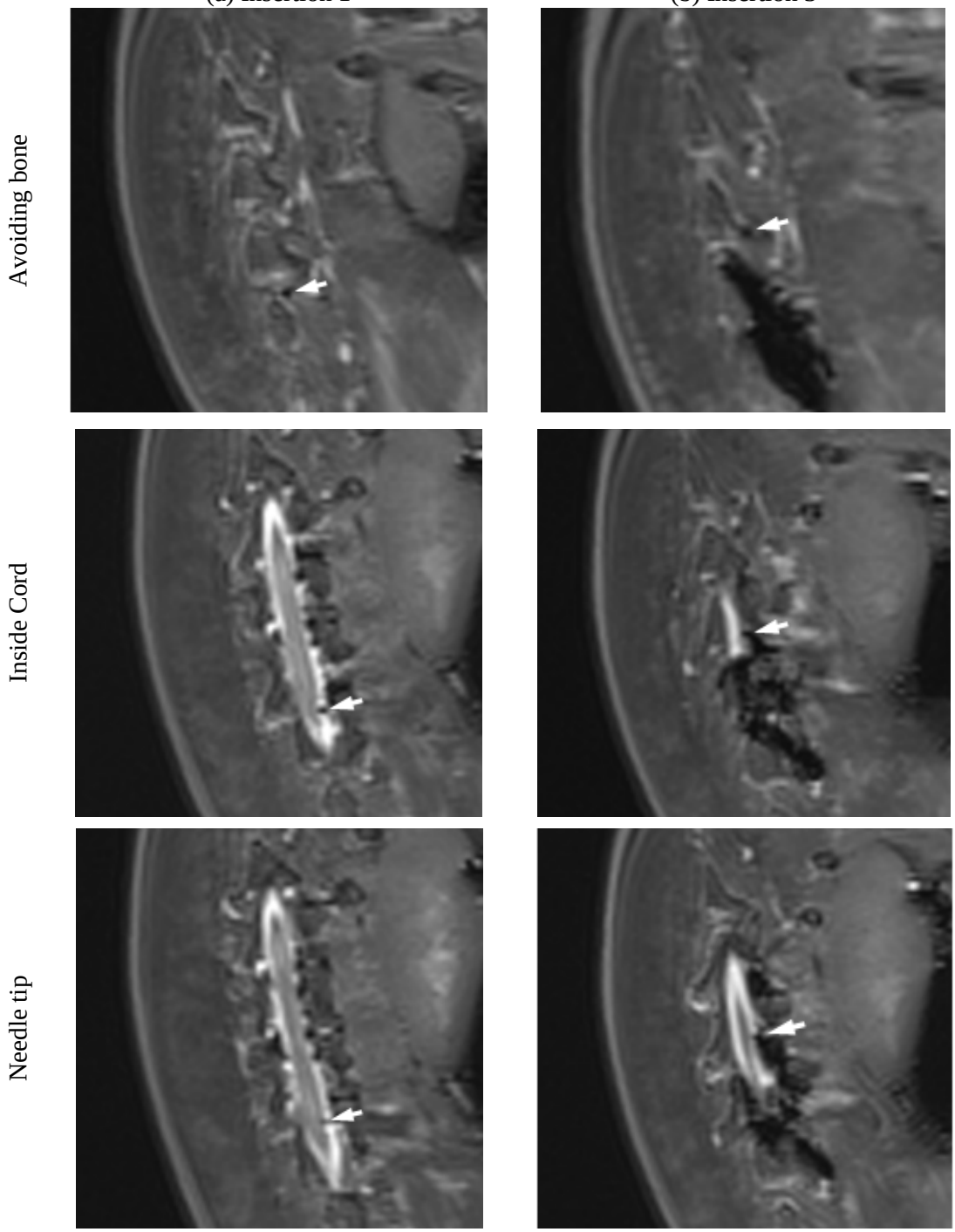

Figure 6.12 – MR images obtained from the cadaver trial using the 4 degree-of-freedom SpinoBot. Needle is indicated by the white arrow. Progressing from the upper images to the lower, the needle trajectory is visible as it avoids the spinous process and punctures the spine.

Discussion

The workflow of the 4 degree-of-freedom system was essentially identical to that of the two degree-of freedom system. Despite the doubling of actuated axes, the system setup remained equivalent, requiring less than 30 seconds additional time to connect the additional motors. This minimal difference maintains the efficiency of the system despite the additional complexity of adding the actuated rotation stage.

One advantage the fully actuated system has lost is the placement of the RCM at the approximate depth of the spine. The positioning of the needle channels converges below the radial template, while the pivot point for targeting with the actuated rotation stage lies above the robot. Placement of the RCM near the spine is relatively forgiving of small errors in positioning, while the higher pivot must be very precise.

Reviews by end users indicated positive reception of the system. One concern frequently raised in discussions about the efficacy of the two DOF robot was the limitations imposed by utilization of the radial template. Continuous actuation of the rotation axes eliminates this concern. The fiducial marker fluid visible in the needle guide enabled registration and confirmation of angulation, but offered an additional benefit. While the system is designed to operate based on the registration of fiducials and provide automatic positioning, an operator can maneuver the robot without any registration whatsoever, aligning the needle guide with the target anatomy by sight or use of other software.

The ease of insertion noted in cadaver trials using this form of the SpinoBot likely stems from design and methodology changes from previous versions. The continuous angulation provides the ability to better avoid vertebrae, and the difference of half a

millimeter can be the difference between successful targeting and grazing the bone, causing deflection. The inclusion of an incision in the skin to assist in needle insertion is a small but important addition to the workflow. Accuracy and ease of insertion both improved when no longer puncturing the skin with the needle. While this incision technically removed the procedure from the realm of percutaneous interventions, the small (<4mm) cut made for each needle insertion would not cause much trauma in a live patient.

CHAPTER 7

CONCLUSIONS AND FUTURE WORK

Aims of this Dissertation

The aim of this dissertation is present the development of robotics systems for MR-guided surgeries and research purposes that are able to function without any metallic components of electromagnetic energy inside the MR scanner room. A further objective is demonstrating the development of these systems in a relatively low-cost fashion. The main systems presented here are intended to aid in the research and treatment of prostate cancer and amyotrophic lateral sclerosis, although the systems can be generalized to uses in other anatomical regions with minor adjustments. The development of these systems will hopefully assist in developing treatments that are more efficient, have less complications, or provide better clinical outcomes – and preferably all three.

Magic Angle Positioning System

Conclusions

Designing the Magic Angle Positioning System served as an introduction to designing MR-compatible devices. The need for a system for use in 9T fields drove the early decision to completely avoid metallic components, which remained in effect during subsequent projects. The early designs of the pneumatic motors were functional but required assumptions in directional pulse counting which were not desirable. Development of modular systems for actuation and positioning first developed in this project.

Prostate Ablation Guide

Conclusions

Targeting and ablation proved successful in phantoms and ex-vivo subjects. The addition of quadrature encoding to the pneumatic motors provides a more accurate method of position reporting, not dependent on software predictions of rotation direction. The use of both actuated and manual degrees of freedom proved to be an effective and intuitive combination, demonstrating that a more complex system, in terms of actuation, is not always a desirable outcome.

Future Work

The design of the prostate robot intentionally mimicked the capabilities of existing prostate treatment templates in the hope that FDA approval is readily acquired if the robot is taken through a standard certification route. An alternate method of achieving human trials is in studies at NIH, where the Center for Cancer Research can use the developed hardware with patients in informed pilot trials. Based on canine cadaver trials, which were successfully able to ablate the prostate despite needing to navigate through the anus and the side of the colon, the chance of successful human trials is high, given the relatively direct access to the prostate.

SpinoBot

Conclusions

Successful targeting of the spinal cord occurred in both pantom and ex-vivo trials. The two degree-of-freedom and four degree-of-freedom versions of the SpinoBot both demonstrated accuracy results meeting the requirements of the neurosurgeons and clinicians associated with the project. The refinement of the pneumatic motors by the

conclusions of this project were quite stable, delivering quadrature encoded TTL signals and reliable operation. The fixed-motor rotation stage presents a novel method for providing continuous angulation solutions over two rotation axes.

Future Work

With the completion of the 4 degree-of-freedom SpinoBot, it has achieved all targeting capabilities of the system it was designed to replace, which was in use by our collaborators. Conclusion of the development of SpinoBot enables its use in clinical trials for the treatment of amyotrophic lateral sclerosis in swine. Should the treatment prove successful, SpinoBot's inclusion in human trials will assist in overcoming the stigmas associated with open surgery on the spine, providing a less invasive option more appealing to those in the early stages of the disease. Beyond the scope of the SpinoBot's intended work, the development of the fixed-motor two degree-of-freedom rotation stage has numerous potential uses in numerous surgical robotics as well as applications in fields where multiple axes of rotation are necessary in a small volume.

The pneumatic motors used serve as a location to improve the physical design of Spinobot, as well as serve in other projects. Small pneumatic tubes and small-fiber quadplex fiber optic lines can reduce cabling volume per motor, reducing setup complexity and interference with the insertion corridor or other parts of the system. Additionally, a motor design with a small gap as in Chapter 5, combined with the form factor of the motor in Chapter 2, will enable the use of the motor in numerous commercially available systems. Refinement of the motor components with regard to the manufacturing system used will ensure proper interference or transition fits, improving the performance of all systems using the motor.

CHAPTER 8

PUBLICATIONS

Current

1) Journal Papers

[1] A. Hamed, S.C. Tang, H. Ren, **A. Squires**, C. Payne, K. Masamune, G. Tang, J. Mohammadpour, Z.T.H. Tse. “Advances in Haptics, Tactile Sensing, and Manipulation for Robot-Assisted Minimally Invasive Surgery, Noninvasive Surgery, and Diagnosis.” Journal of Robotics, 2012, Article ID 4128 16.

[2] **A. Squires**, Y. Gao, S. Taylor, M. Kent, Z.T.H. Tse. “A Simple and Inexpensive Stereotactic Guidance Frame for MRI-Guided Brain Biopsy in Canines.” Journal of Medical Engineering, 2014, Article ID 139535.

[3] L.C. Ho, I.A. Sigal, N. Jan, **A. Squires**, Z.T.H. Tse, E.X. Wu., S. Kim, J.S. Schuman, K.C. Chan. “Magic Angle-Enhanced MRI of Fibrous Microstructures in Sclera and Cornea with and without Intraocular Pressure Loading.” Invest. Ophthalmol. Vis. Sci. August 7, 2014 IOVS-14-1456 1.

[4] **A. Squires**, J. Oshinski, J. Lamanna, and Z. T. H. Tse, "SpinoTemplate: A Platform for MRI-Guided Spinal Cord Injections," *Journal of Medical Robotics Research*, vol. 01, p. 1640006, 2016.

[5] **A. Squires**, K. C. Chan, L. C. Ho, I. A. Sigal, N.-J. Jan, and Z. T. H. Tse, "MAPS – A Magic Angle Positioning System for Enhanced Imaging in High-Field Small-Bore MRI." Journal of Medical Robotics Research, vol. 01, p. 1640004, 2016.

[6] Y. Chen, **A. Squires**, R. Seifabadi, S. Xu, H. Agarwal, M. Bernardo, et al., "Robotic System for MRI-guided Focal Laser Ablation in the Prostate," IEEE/ASME Transactions on Mechatronics.

2) Conference Papers/Abstracts

[1] K.C. Chan, Z.T.H. Tse, T. Pirkle, **A. Squires**, N.J. Jan, G. Wollstein, J.S. Schuman, S. Kim, I.A. Sigal. “Magic Angle Enhanced MR Imaging of Ocular Fibrous Microstructures.” 22nd IEEE International Symposium on Industrial Electronics, Taipei, 2013.

[2] C. Mershon, **A. Squires**, Y. Gao, K.C. Chan, Z.T.H. Tse. “Magic Angle Enhanced Imaging in High-Field MRI Using an Automated MR-Conditional Positioners.” International Society of Magentic Resonance in Medicine, Salt Lake City, 2013.

[3] L.C. Ho, I.A. Sigal, N.J. Jan, H. Mehrens, **A. Squires**, Z.T.H. Tse, E.X. Wu, J.S. Schuman, S.G. Kim, T. Jin, K.C. Chan. “Magic angle enhanced MR microscopy of fibrous structures in normotensive and hypertensive eyes using T2, T2* and T1rho MRI.” International Society of Magentic Resonance in Medicine, Milan, 2014.

[4] J. Box, T.S. Gregory, **A. Squires**., Y. Gao., Z.T.H. Tse. “Development of a Magnetohydrodynamically Driven Actuator for Use in MRI.” International Society of Magentic Resonance in Medicine, Milan, 2014.

[5] Y. Gao, K.-W. Kwok, R. Chandrawanshi, **A. Squires**, A. C. Nau, Z. Tsz, et al., "Wearable Virtual White Cane: Assistive Technology for Navigating the Visually Impaired1," Journal of Medical Devices, vol. 8, pp. 020931-020931, 2014.

[6] **A. Squires**, J. Oshinski, J. Lamanna, Z.T.H. Tse. “SpinoTemplate: A System for MR-Guided Spinal Cellular Therapeutics Injections.” International Society of Magentic Resonance in Medicine, Toronto, 2015.

[7] R. Seifabadi, Y. Chen, **A. Squires**, S. Xu, H. Agrawal, M. Bernardo, A. Negussie, P. Pinto, P. Choyke, Z.T.H. Tse, B. Wood. “Toward A Robotic System for MRI-guided Focal Laser Ablation of Prostate.” World Conference on Interventional Oncology, New York, 2015.

[8] **A. Squires**, S. Xu, R. Seifabadi, Y. Chen, H. Agrawal, M. Bernardo, A. Negussie, P. Pinto, P. Choyke, B. Wood, Z.T.H. Tse. “Prostate Focal Prostate Laser Ablation under MRI Guidance.” International Society of Magentic Resonance in Medicine, Singapore, 2016.

[9] **A. Squires**, S. Xu, R. Seifabadi, Y. Chen, H. Agrawal, M. Bernardo, A. Negussie, P. Pinto, P. Choyke, B. Wood, Z.T.H. Tse. “Robot for MRI-Guided Focal Prostate Laser Ablation.” Design of Medical Devices, Minneapolis, 2016.

[10] **A. Squires**, J. Oshinski, J. Lamanna, Z.T.H. Tse. “Development of a Platform for Injection of Cellular Therapeutics to the Spine under MRI Guidance.” 8th NCIGT Image Guided Therapy Workshop, 2016.

[11] **A. Squires**, Y. Chen, R. Seifabadi, S. Xu, H. Agrawal, M. Bernardo, P. Pinto, P. Choyke, B. Wood, Z.T.H. Tse. “Evaluation of Robot-Assisted Prostate Focal Laser Ablation with MRI Guidance.” 8th NCIGT Image Guided Therapy Workshop, 2016.

[12] Y. Chen, **A. Squires**, S. Xu, R. Seifabadi, H. Agrawal, M. Bernardo, P. Pinto, P. Choyke, B. Wood, Z.T.H. Tse. “NIH OncoNav Surgical Planning Software:

Optimized Workflow for MRI-guided Prostate Focal Laser Ablation." 8th NCIGT Image Guided Therapy Workshop, 2016.

[13] Y. Chen, **A. Squires**, R. Seifabadi, S. Xu, H. Agrawal, M. Bernardo, P. Pinto, P. Choyke, B. Wood, Z.T.H. Tse. "MR-conditional Robot for Transperineal Prostate Focal Laser Ablation." 8th NCIGT Image Guided Therapy Workshop, 2016.

[14] **A. Squires**, S. Xu, R. Seifabadi, Y. Chen, H. Agarwal, M. Bernardo, et al., "Robot for Magnetic Resonance Imaging Guided Focal Prostate Laser Ablation." Journal of Medical Devices, vol. 10, pp. 030942-030942, 2016.

Under Review

1) Journal Papers

[1] **A. Squires**, J. Oshinski, Z.T.H. Tse. "Robotic System for MRI-guided Cellular Therapeutics Treatment in the Spine." IEEE Transactions/Mechatronics.

2) Conference Papers/Abstracts

[1] **A. Squires**, J. Oshinski, Z.T.H. Tse. "Instrument Guidance System for MRI-Guided Percutaneous Spinal Interventions." Design of Medical Devices, Minneapolis, 2017.

[2] Z.T.H. Tse, S. Xu, **A. Squires**, Y. Chen, R. Seifabadi, H. Agrawal, M. Bernardo, P. Pinto, P. Choyke, B. Wood. "Robot for MRI-guided Prostate Cancer Focal Laser Ablation." Design of Medical Devices, Minneapolis, 2017.

[3] Z.T.H. Tse, **A. Squires**, J. Oshinski. "Robot for MRI-guided ALS Spinal Therapy." Design of Medical Devices, Minneapolis, 2017.

[4] Z.T.H. Tse, S. Xu, A. Squires, Y. Chen, R. Seifabadi, H. Agrawal, M. Bernardo, P. Pinto, P. Choyke, B. Wood. “Treatment Planning for MRI-guided Prostate Focal Laser Ablation” Design of Medical Devices, Minneapolis, 2017.

In Preparation

1) Journal Papers

[1] **A. Squires**, S. Xu, R. Seifabadi, Y. Chen, H. Agrawal, M. Bernardo, A. Negussie, P. Pinto, P. Choyke, B. Wood, Z.T.H. Tse. “Preclinical Study of Robot-assisted Focal Laser Ablation in Canine Prostate under MRI Guidance.” Magnetic Resonance in Medicine.

[2] **A. Squires**, J. Oshinski, Z.T.H. Tse. “Development of a Low-Profile System for MR-Guided Injections along the Spine.” IEEE Transactions.Mechatronics.

[3] **A. Squires**, S. Xu, R. Seifabadi, Y. Chen, H. Agrawal, M. Bernardo, A. Negussie, P. Pinto, P. Choyke, B. Wood, Z.T.H. Tse. “Robot-Assisted Prostate Focal Laser Ablation under MRI Guidance.” Journal of Medical Robotics Research.